

UNIVERSITÀ DELLA CALABRIA



UNIVERSITÀ DELLA CALABRIA

Dipartimento di Ingegneria Civile

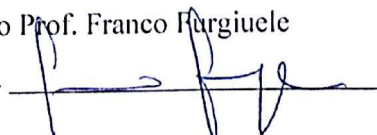
Dottorato di Ricerca in
Ingegneria Civile ed Industriale

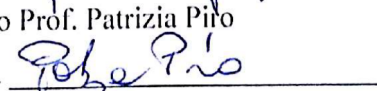
CICLO


XXIX

**ON THE USE OF MECHANISTIC MODELING FOR THE NUMERICAL
ANALYSIS OF LOW IMPACT DEVELOPMENT TECHNIQUES**

Settore Scientifico Disciplinare ICAR/02

Coordinatore: Ch.mo Prof. Franco Furgiuele
Firma 

Supervisore/Tutor: Ch.mo Prof. Patrizia Piro
Firma 

Dottorando: Dott. Giuseppe Brunetti
Firma 

I would like to dedicate this thesis to my loving parents and wonderful brothers...

Declaration

I hereby declare that except where specific reference is made to the work of others, the contents of this dissertation are original and have not been submitted in whole or in part for consideration for any other degree or qualification in this, or any other University. This dissertation is the result of my own work and includes nothing which is the outcome of work done in collaboration, except where specifically indicated in the text.

Dott. Giuseppe Brunetti

2017

Acknowledgements

And I would like to acknowledge all the people that shared with me this path. Everyone gave me something unique.

Abstract

The increasing frequency of flooding events in urban catchments related to an increase in impervious surfaces highlights the inadequacy of traditional urban drainage systems. Low-impact developments (LIDs) techniques have proven to be valuable alternatives for stormwater management and hydrological restoration, by reducing stormwater runoff and increasing the infiltration and evapotranspiration capacity of urban areas. However, the lack of diffusion of adequate modelling tools represents a barrier in designing and constructing such systems. Mechanistic models are reliable and accurate tools for analysis of the hydrologic behaviour of LIDs, yet only a few studies provide a comprehensive numerical analysis of the hydrological processes involved and test their model predictions against field-scale data. Moreover, their widespread use among urban hydrologists suffers from some limitations, namely: *complexity*, *model calibration* and *computational cost*. This suggests that more research is needed to address these issues and examine the applicability of this kind of models. Thus, the main aim of this thesis was to investigate the benefits and the limitations in the use of mechanistic modelling for LIDs analysis. In this view, the mechanistic modelling approach has been used to simulate the hydraulic/hydrologic behaviour of three different LIDs installed at the University of Calabria: an extensive green roof, a permeable pavement and a stormwater filter. Each case study was used to examine a particular modelling aspect. The morphological and hydrological complexity of the green roof required the use of a three-dimensional mechanistic model, which was validated against experimental data with satisfactory results. The measured soil hydraulic properties of the soil substrate highlighted important characteristics, accounted in the simulation. The validated model was used to carry out a hydrological analysis of the green roof and its hydrological performance during the entire simulated period as well as during single precipitation events. Conversely, a one-dimensional mechanistic model was used to simulate the hydraulic behaviour of a permeable pavement, whose parameters were calibrated against experimental data. A Global Sensitivity Analysis (GSA) followed by a Monte Carlo filtering highlighted the influence of the wear layer on the hydraulic behaviour of the pavement and identified the ranges of parameters generating *behavioural* solutions in the optimization

framework. Reduced ranges were then used in the calibration procedure conducted with the metaheuristic Particle swarm optimization (PSO) algorithm for the estimation of hydraulic parameters. The calibrated model was then validated against an independent set of data with good results. Finally, to address the issue of computational cost, the surrogate-based modelling technique has been applied to calibrate a two-dimensional mechanistic model used to simulate the hydraulic behaviour of a stormwater filter. The kriging technique was utilized to approximate the deterministic response of the mechanistic model. The validated kriging model was first used to carry out a Global Sensitivity Analysis of the unknown soil hydraulic parameters of the filter layer. Next, the Particle Swarm Optimization algorithm was used to estimate their values. Finally, the calibrated model was validated against an independent set of measured outflows with optimal results. Results of the present thesis confirmed the reliability of mechanistic models for LIDs analysis, and gave a new contribution towards a much broader diffusion of such modelling tools.

Contents

| | |
|---|------|
| Contents | xi |
| List of Figures | xiii |
| List of Tables | xvii |
| Chapter 1 Introduction..... | 19 |
| 1.1 Urban Drainage Systems: issues and new challenges..... | 19 |
| 1.2 Sustainable Stormwater Management..... | 21 |
| 1.2.1 Modelling tools for LIDs analysis | 23 |
| 1.3 Objectives and aim | 25 |
| Chapter 2 A comprehensive analysis of the variably-saturated hydraulic behaviour of a green roof in a Mediterranean climate | 29 |
| 2.1 Introduction | 29 |
| 2.2 Materials and Methods | 33 |
| 2.2.1 Green Roof and Site Description | 33 |
| 2.2.2 Soil Hydraulic Properties | 38 |
| 2.2.3 Modeling Theory | 42 |
| 2.2.4 Statistical Evaluation | 49 |
| 2.3 Results and Discussion..... | 50 |
| 2.3.1 Soil Hydraulic Properties..... | 50 |
| 2.3.2 Model Validation | 54 |
| 2.3.3 Hydrological Analysis of the Green Roof | 58 |
| 2.3.4 Hydrological Performance during Precipitation Events | 62 |
| 2.4 Conclusions | 65 |
| Chapter 3 A comprehensive numerical analysis of the hydraulic behavior of a permeable pavement 69 | |
| 3.1 Introduction | 69 |
| 3.2 Materials and Methods | 74 |
| 3.2.1 Site Description..... | 74 |
| 3.2.2 Theory..... | 78 |
| 3.3 Results and Discussion..... | 92 |
| 3.3.1 Sensitivity Analysis – Scenario I | 92 |

| | | |
|---|---|-----|
| 3.3.2 | Monte Carlo Filtering – Scenario I | 95 |
| 3.3.3 | Sensitivity Analysis – Scenario II..... | 97 |
| 3.3.4 | Monte Carlo Filtering – Scenario II..... | 100 |
| 3.3.5 | Particle Swarm Optimization | 102 |
| 3.3.6 | Confidence Regions | 107 |
| 3.3.7 | Model Validation | 108 |
| 3.4 | Conclusions | 112 |
| Chapter 4 On the use of surrogate-based modeling for the numerical analysis of Low Impact Development techniques..... | | 115 |
| 4.1 | Introduction | 115 |
| 4.2 | Materials and Methods | 119 |
| 4.2.1 | Stormwater Filter and Site Description..... | 119 |
| 4.2.2 | Evaporation Method and Parameter Estimation | 124 |
| 4.2.3 | Modeling Theory | 125 |
| 4.2.4 | Surrogate Based Model..... | 130 |
| 4.2.5 | Global Sensitivity Analysis (GSA)..... | 135 |
| 4.2.6 | Particle Swarm Optimization..... | 137 |
| 4.2.7 | Objective Function..... | 139 |
| 4.3 | Results and Discussion..... | 139 |
| 4.3.1 | Evaporation Method..... | 139 |
| 4.3.2 | Kriging Approximation of the Response Surface | 141 |
| 4.3.3 | Global Sensitivity Analysis..... | 143 |
| 4.3.4 | Kriging-Based Optimization | 145 |
| 4.3.5 | Model Validation | 152 |
| 4.4 | Conclusions and Summary..... | 154 |
| Chapter 5 Conclusions and future directions..... | | 157 |
| 5.1 | Future directions..... | 160 |
| References..... | | 163 |

List of Figures

Figure 1.1 A schematic of the current stormwater management20

Figure 1.2 A schematic of a sustainable stormwater management22

Figure 2.1 A typical cross-section of the GR.....34

Figure 2.2 A schematic of the green roof, showing both vegetated (grey) and non-vegetated (white) areas. Irrigation drippers are indicated by a letter D.35

Figure 2.3 Measured precipitation (black), irrigation (top graph), and subsurface (gray) fluxes for a selected time period.....37

Figure 2.4 Details of the drainage layer, where d is the thickness of the open space between drainage holes, and the geotextile supporting the GR substrate.45

Figure 2.5 Spatial distribution of considered boundary conditions.46

Figure 2.6 Measured and modeled values of the retention curve $\theta(\log_{10}(h))$ (left) and the hydraulic conductivity functions $K(\log_{10}(h))$ (center) and $K(\theta)$ (right). The measured values are scatter points, the full and dashed lines are the fitted bimodal and unimodal functions, respectively.51

Figure 2.7 A comparison between measured and simulated outflows versus time and against each other (in the insert). The full and dashed lines in the insert are bisector and linear regression lines, respectively.55

Figure 2.8 A lag plot of the residuals between measure and simulated outflows. Results are for the HYDRUS model with the unimodal (left) and bimodal (right) functions of soil hydraulic properties.57

Figure 2.9 A comparison between cumulative inflow and outflow from the GR, simulated by HYDRUS-3D.....59

Figure 2.10 Simulated actual root water uptake (top) and evaporation (bottom) from vegetated areas of the green roof.60

Figure 2.11 Pressure heads at the bottom of the vegetated (black) and non-vegetated (red) sections of the GR simulated by HYDRUS-3D. The yellow rectangular area in the top figure is expanded in the bottom figure. The dashed line represents a seepage condition.....61

Figure 2.12 Precipitation (dark area), modeled (grey area) and measured (red line) outflow for four selected rainfall events in the analysis of the hydrological performance of the GR during single precipitation events.63

| | |
|--|-----|
| Figure 2.13 Simulated water contents in the vegetated section of the GR at a depth of 4 cm. | 64 |
| Figure 3.1 A schematic of the permeable pavement. | 74 |
| Figure 3.2 Precipitation and subsurface flow during the optimization (top) and validation (bottom) time periods. | 77 |
| Figure 3.3 Scatter plots for pair relations a_1 - NSE (left) and n_1 - NSE (right) for Scenario I. The red line is a regression line. | 94 |
| Figure 3.4 Bivariate KDE plots (below diagonal), univariate KDE plots (diagonal), and correlation plots (above diagonal) for Scenario I. | 96 |
| Figure 3.5 The average total index, S_T , for different layers for both scenarios. | 99 |
| Figure 3.6 Scatter plots for pair relations a_1 - NSE (left) and n_1 - NSE (right) for Scenario II. The red line is a regression line. | 100 |
| Figure 3.7 Bivariate KDE plots (below diagonal), univariate KDE plots (diagonal), and correlation plots (above diagonal) for Scenario II. | 101 |
| Figure 3.8 Comparison between the modeled and measured hydrographs for Scenarios I (top) and II (bottom) for the optimization process. | 104 |
| Figure 3.9 Comparison between the modeled and measured hydrograph for the two scenarios for the validation period. | 109 |
| Figure 3.10 Comparison between the modeled and measured outflows for the two scenarios for the validation period. | 111 |
| Figure 4.1 A schematic of the experimental site (top) and a typical cross-section (bottom) of the stormwater filter. | 120 |
| Figure 4.2 Precipitation (black line) and subsurface flow (grey line) for the optimization (top) and validation (bottom) periods, respectively. | 123 |
| Figure 4.3 The spatial distribution of applied boundary conditions. | 129 |
| Figure 4.4 Measured values and modeled functions of soil water retention, $\theta(\log_{10}(h))$ (left) and the unsaturated hydraulic conductivity, $K(\log_{10}(h))$ (center) and $K(\theta)$ (right). Symbols represent the measured values, and full lines the fitted VGM functions. | 140 |
| Figure 4.5 Comparison between the HYDRUS-2D and kriging-predicted values of the NSE for the validation sample. The initial (grey diamonds) and infilled (red circles) kriging models are compared. A bisector (a black line) and regression lines for the initial (a dashed grey line) and infilled (a dashed red line) kriging models are reported. | 142 |
| Figure 4.6 A comparison between measured and simulated outflows versus time and against each other (in the insert) for the calibration period. The full and dashed lines in the insert are a bisector and linear regression line, respectively. | 147 |
| Figure 4.7 The $\alpha - K_s$ response surface obtained using a regular grid of 40,000 points. The red lines indicate the cross sections reported in Figure 4.8. | 149 |
| Figure 4.8 Horizontal [$K_s = 90$ cm/min] (top), and vertical [$\alpha = 0.001$ 1/cm] (bottom) response surface cross-sections. The yellow rectangular areas for both plots are expanded on the right. | 151 |

Figure 4.9 A comparison between measured and simulated outflows versus time and against each other (in the insert) during the validation period. The full and dashed lines in the insert are a bisector and linear regression line, respectively..... 153

List of Tables

| | |
|---|-----|
| Table 2.1 Feddes' parameters for the water stress response function used in numerical simulations. | 43 |
| Table 2.2 Fluxes considered in different types of boundary conditions. | 47 |
| Table 2.3 Estimated soil hydraulic parameters and their confidence intervals (CIs) for the unimodal and bimodal hydraulic functions. | 52 |
| Table 3.1 Conceptual models representing water flow in the permeable pavement. | 78 |
| Table 3.2 Number of parameters and HYDRUS-1D runs for both scenarios. | 86 |
| Table 3.3 Ranges of parameters used in the GSA for both scenarios. | 87 |
| Table 3.4 Parameters used in the PSO optimization. | 91 |
| Table 3.5 First-order (S_1) and total (S_T) effect indices (in decreasing order) with their bootstrap confidence intervals (BCI) for parameters of Scenario I. | 92 |
| Table 3.6 First-order (S_1) and total (S_T) effect indices (in decreasing order) with their bootstrap confidence intervals (BCI) for parameter of Scenario II. | 98 |
| Table 3.7 Reduced ranges of optimized parameters for the optimization process. | 103 |
| Table 3.8 Optimized soil hydraulic parameters for both scenarios. | 105 |
| Table 3.9 Confidence intervals (CI) for optimized parameters for both scenarios. | 107 |
| Table 4.1 Ranges of investigated parameters for the surrogate-based analysis. | 127 |
| Table 4.2 Parameters used in the PSO optimization. | 138 |
| Table 4.3 Estimated soil hydraulic parameters and their confidence intervals for the soil substrate. | 141 |
| Table 4.4 The first-order (S_1) and total (S_T) effect indices (in a decreasing order) with their bootstrap confidence intervals (BCI) for the soil hydraulic parameters. | 144 |
| Table 4.5 VGM parameters for the filter layer. The shape parameter α and the saturated hydraulic conductivity K_s were estimated using the PSO algorithm. | 146 |
| Table 4.6 VGM parameters for the filter layer. The saturated water content θ_s , the shape parameters α and n , and the saturated hydraulic conductivity K_s were estimated using the PSO algorithm. | 152 |

Chapter 1 Introduction

“*Sustainability*” is not only a word, but a concept that is permeating our life in the last few decades. A concept that represents an abrupt and necessary change in our way of living; a change that is needed in order to not compromise the lives of the new generations:

« *Development that meets the needs of the present without compromising the ability of the future generations to meet their own needs*».

This is the basic definition of *sustainable development* proposed at the World’s first Earth Summit in Rio de Janeiro in 1992. Before that date, the concept of sustainability was something rather marginal in the society, focused on the economic growth and industrial development after the tragedies of the second World War. The exponential demographic growth, the technological progress and the wild globalization pushed the society towards a new model, where individual needs are multiplied. To deal with this change, Earth’s resources were exploited at an unsustainable rate, disregarding the negative impacts on the environment. Air, soil and water pollution became the most important threats to the global health, with the appearance of new contaminants. The *sustainability* concept emerged as the unique viable approach to counterbalance and mitigate the negative impacts of the current development model.

1.1 Urban Drainage Systems: issues and new challenges

Progressing urbanization of undeveloped land leads to an increasing amount of impervious surfaces at the expense of natural areas. Leopold (1968), while describing the effects of urbanization on the hydrological cycle, identified such major effects as reduced

infiltration and evapotranspiration, resulting in increased runoff and reduced groundwater recharge. Traditional stormwater management design focused on collecting stormwater in piped networks and transporting it off-site as quickly as possible. Increases in the incidence of flooding and combined sewer overflows (CSOs) in urban areas demonstrate that the traditional approach is inadequate for managing stormwater. Traditional urban drainage systems are unable to cope with a constant increase of surface runoff due to structural limitations. Drainage systems, especially in European cities, consist of facilities built in different epochs, and designed to manage considerably lower runoff volumes. In such circumstances, it is quite usual to have in the same cities flooded and non-flooded districts, depending on the structure of the drainage system.

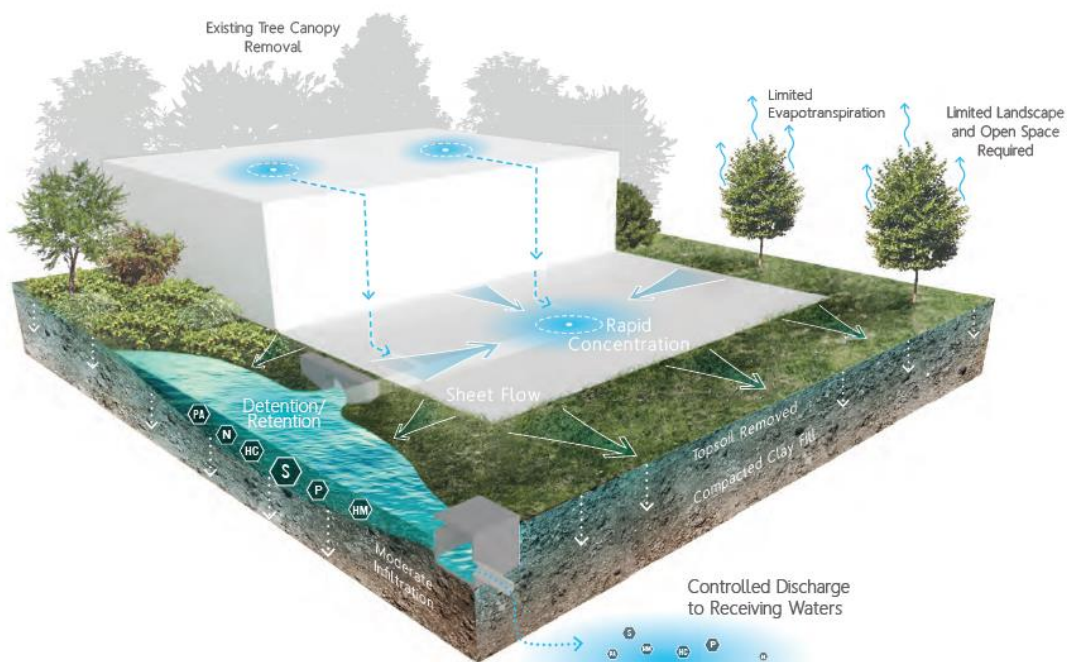


Figure 1.1 A schematic of the current stormwater management

In a context where the resiliency of urban areas under climate change becomes crucial, the inadequacy of traditional urban drainage systems can pose serious problems. Urbanized landscapes are one of the most sensitive systems to hydrological extremes, fluctuations and changes. The change of precipitation regime, which is likely to occur in the immediate future, will increase the frequency of extreme precipitation events (Lenderink and van Meijgaard, 2008), known to be correlated with flash floods in urban areas. In such circumstances, it is necessary to treat the stormwater management as an urgent problem and find *sustainable* solutions able to cope with today's and upcoming problems.

1.2 Sustainable Stormwater Management

As mentioned above, the combined effects of increased imperviousness and climate change is highlighting the inadequacy of traditional drainage systems in stormwater management. A theoretical alternative would be to replace existing piped networks with larger ones able to manage an increased surface runoff, but this poses economic and practical problems. Thus, it is necessary to shift the target to the reasons of runoff increase, namely the surface's imperviousness, main cause of the alteration of the urban hydrological cycle. In this view, the sustainable stormwater management aims to preserve and restore natural features, minimize the imperviousness of urban catchments, and increase their infiltration and evapotranspiration capacities.

The so-called "Sponge cities" focus on mimicking the hydrology that existed prior to the development through the use of micro-controls distributed throughout a developed site. These micro-controls are located near the source where runoff is generated and help deliver it back to its natural pathway (through permeable materials into the ground, or through evaporation into the air). Micro-controls can include stormwater filters, green roofs, wetlands, permeable pavements and other measures that reduce both runoff volume and speed. Rain can also be harvested in cisterns for landscape irrigation and other beneficial uses. Such practices are

commonly known as *Low Impact Development (LID)* techniques, or *Green Infrastructures (GI)*.

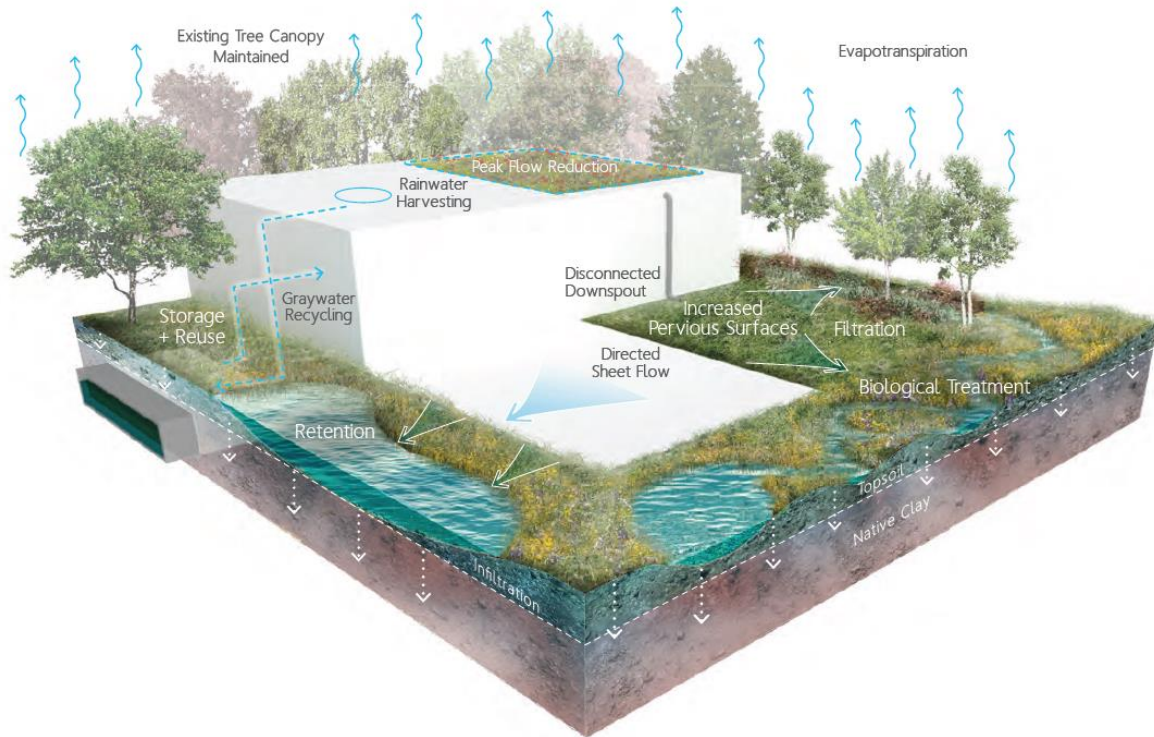


Figure 1.2 A schematic of a sustainable stormwater management

Low-impact developments are able to reduce runoff volumes and pollutant loads and increase evapotranspiration. Green roofs were able to significantly reduce peak rates of stormwater runoff (Getter et al., 2007) and retain rainfall volumes with retention efficiencies ranging from 40 to 80% (Bengtsson et al., 2004). Bioretention cells were shown to reduce average peak flows by at least 45% during a series of rainfall events in Maryland and North Carolina (Davis, 2008). Permeable pavements offered great advantages in terms of runoff reduction (Carbone et al., 2014; Collins et al., 2008), water retention, and water quality improvement (Brattebo and Booth, 2003).

1.2.1 Modelling tools for LIDs analysis

In spite of the large and well-known benefits of green roofs and other LID techniques, the transition to sustainable urban drainage systems is very slow. One of the key limiting factors in the widespread adoption of such systems is the lack of adequate analytical and modelling tools (Elliot and Trowsdale, 2007) able to simulate all the physical processes involved. Several models have been proposed in the literature; most of them focused on simulating the hydraulic/hydrologic behaviour of the system.

Empirical models are models where the structure is determined by the observed relationship among experimental data. These models can be used to develop relationship for forecasting and describing trends, which are not necessarily mechanistically relevant. Typical examples of empirical models for LIDs analysis include relationships between the rain depth and the subsurface runoff coefficient, or between the antecedent dry periods and the surface runoff coefficient. The main drawback of this kind of models is the lack of generality. The accuracy of the empirical relation is strongly dependent on the size and characteristics of the sample used for the statistical analysis. For example, a relationship between the retention efficiency of a green roof in a continental climate, and the antecedent dry period will lead to inaccurate results if applied to a green roof in a mediterranean climate. Only by increasing the size and the variance of the sample, it would be possible to increase the robustness of the empirical model. However, even if the sample is statistically representative and significant, the uncertainty associated with the developed relationship could lead to biased conclusions.

An alternative is represented by conceptual models. A conceptual model is a descriptive representation of a system that incorporates the modeler's understanding of the relevant physical processes involved. In this type of modelling, the different components of the system are described using conceptual entities. For example, the hydraulic behaviour of a porous media is described using a reservoir with a sharp-crested weir, whose height represents the field capacity, and whose discharge rate represents its hydraulic conductivity. Conceptual models have been used extensively in the literature for the numerical analysis of LIDs, in particular for green roofs. Kasmin et al. (2010) developed a simple conceptual model of the hydrological

behaviour of green roofs during a storm event. The model input was the time series of precipitation events and the output was runoff. The water content in the green roof at any given time was between field capacity and the residual water content. Evapotranspiration was estimated using an empirical relationship accounting for the actual water contents, the storm event's characteristics, and the antecedent dry weather period. During a precipitation event, the porous medium absorbed moisture until field capacity was reached. The addition of further moisture produced subsurface flow. Stovin et al. (2013) used a conceptual model to simulate the hydraulic behaviour of a green roof. In that model, the actual evapotranspiration is function of the potential evapotranspiration and substrate moisture content, and the retention capacity is conceptualized as a reservoir. While being quite fast and intuitive, conceptual models suffer from several limitations. Conceptualization of the physical processes involved often leads to simplification of the system and a reduction in numerical parameters. While in a physical model each parameter has its own meaning, in conceptual models, lumped parameters often incorporate different components of the described process. These lumped parameters are case sensitive and need to be calibrated against experimental data, implying a lack of generality of the model itself. These drawbacks could represent a barrier to the use of modeling tools among practitioners who need reliable and generally applicable models.

Conceptual models represent a middle ground between empirical and mechanistic models. While empirical models are based on direct observation, measurement and extensive data records, mechanistic models are based on the mathematical description of physical, chemical, and biological processes involved. One of the main advantage of mechanistic approach is that each component has a clear physical meaning, and each parameter can be measured independently. In spite of being accurate and general, mechanistic models are not widely for the numerical analysis of LIDs. This is mainly due to some drawbacks, which are typical in mechanistic modeling:

- *Complexity*: in the mechanistic approach, each process is analysed separately and characterized by a particular set of equations. The modeller must be

familiar with all the processes involved (i.e, infiltration, evaporation, transpiration, preferential flows, solute transport, heat transport, etc);

- *Model calibration*: The calibration of mechanistic models can be quite challenging, and usually involves the optimization of several parameters. This requires the use of complex optimization algorithm and a careful quantification of the uncertainty associated with each estimated parameter;
- *Computational cost*: Mechanistic models usually require the numerical resolution of nonlinear partial differential equations. Depending on the type of problem, the computational cost associated with a single model execution can be significantly high, especially if several physical processes are modelled simultaneously. This cost increases exponentially if the modelling framework includes the calibration of several parameters, making impractical the use of the model itself.

1.3 Objectives and aim

The main aim of the present thesis is to investigate the use of mechanistic modelling for the numerical analysis of LIDs. In particular, the present study focuses on the three main drawbacks of mechanistic modeling, namely: *complexity*, *model calibration* and *computational cost*.

A mechanistic model is used to describe the hydraulic/hydrologic behaviour of three different LIDs installed at the University of Calabria: an extensive green roof, a permeable pavement and a stormwater filter. Each experimental site served as a case study to investigate the different aspects of mechanistic modelling. Specific laboratory measurements were used to support the modelling framework. Thus, the thesis is conceived and structured as a “cumulative thesis” composed of three different scientific papers, already published in international peer-reviewed journals.

In Chapter 2, the software HYDRUS-3D is used to simulate the hydraulic behaviour of an extensive green roof. The soil hydraulic properties of the soil substrate are measured and analysed by using the simplified evaporative method. Both unimodal and bimodal soil hydraulic functions are used in the analysis. The estimated parameters are then used in the HYDRUS-3D model to simulate a 2-month period. Precipitation, irrigation, evaporation, and root water uptake processes were included in the numerical analysis. The model is validated against experimental data, and then used to carry out a hydrological analysis of the green roof and its hydrological performance during the entire simulated period as well as during single precipitation events.

In Chapter 3, a mechanistic model is calibrated to simulate the hydraulic functioning of a permeable pavement. Two different scenarios of describing the hydraulic behavior of the permeable pavement system are analyzed: the first one uses a single porosity model for all layers of the permeable pavement; the second one uses a dual-porosity model for the base and sub-base layers. Measured and modeled month-long hydrographs are compared using the Nash-Sutcliffe efficiency (NSE) index. A Global Sensitivity Analysis (GSA) followed by a Monte Carlo filtering is used to investigate the sensitivity of different parameters and to identify the ranges of parameters generating behavioral solutions. Reduced ranges are then used in the calibration procedure conducted with the metaheuristic Particle swarm optimization (PSO) algorithm for the estimation of hydraulic parameters. The calibrated parameters are then validated against an independent set of experimental data.

In Chapter 4, the benefit of surrogate-based modelling in the numerical analysis of LIDs is investigated. The kriging technique is used to approximate the deterministic response of the widely used mechanistic model HYDRUS-2D, which was employed to simulate the variably-saturated hydraulic behaviour of a contained stormwater filter. The Nash-Sutcliffe efficiency (NSE) index is used to compare the simulated and measured outflows and as the variable of interest for the construction of the response surface. The validated kriging model is first used to carry out a Global Sensitivity Analysis of the unknown soil hydraulic parameters of the filter layer. Next, the Particle Swarm Optimization algorithm is used to estimate their values. The

surrogate-based optimized parameters are then validated against an independent set of experimental data.

It must be emphasized that a common issue of all modeling scenarios analyzed in the present thesis has been the limited information about the transient flow data. In particular, only measured inflows and outflows were available. In such circumstances, the optimization problem can become ill-posed thus increasing the uncertainty in the estimated parameters. For this reason, advanced numerical techniques such as the Global Sensitivity Analysis and Particle Swarm Optimization have been used. Moreover, further laboratory analysis were carried out in order to obtain specific measurements in order to reduce the dimensionality of the problem and facilitate the modeling framework.

Chapter 2 A comprehensive analysis of the variably-saturated hydraulic behaviour of a green roof in a Mediterranean climate

2.1 Introduction

During the last few decades, the area of impervious surfaces in urban areas has exponentially increased as a consequence of the demographic growth. This long-term process has altered the natural hydrological cycle by reducing the infiltration and evaporation capacity of urban catchments, while increasing surface runoff and reducing groundwater recharge. Moreover, the frequency of extreme rainfall events, characterized by high intensity and short duration, is expected to increase in the near future as a consequence of global warming (Kundzewicz et al., 2006; Min et al., 2011).

The combined effects of urbanization and climate change expose urban areas to an increasing risk of flooding. In this context, urban drainage systems play a fundamental role in improving the resilience of cities. In recent years, an innovative approach to land development known as a Low Impact Development (LID) has gained increasing popularity. LID is a 'green' approach to storm water management that seeks to mimic the natural hydrology of a site using decentralized micro-scale control measures (Coffman, 2002). LID practices consist of bioretention cells, infiltration wells/trenches, storm water wetlands, wet ponds, level spreaders, permeable pavements, swales, green roofs, vegetated filter/buffer strips, sand filters, smaller culverts, and water harvesting systems. LIDs are able to reduce runoff volumes and pollutant

loads and increase evapotranspiration. Green Roofs (GR) were able to significantly reduce peak rates of storm water runoff (Getter et al., 2007) and retain rainwater volumes with retention efficiencies ranging from 40% to 80% (Bengtsson et al., 2004). Bioretention cells were shown to reduce average peak flows by at least 45% during a series of rainfall events in Maryland and North Carolina (Davis, 2008). Permeable pavements offered great advantages in terms of runoff reduction (Carbone et al., 2014; Collins et al., 2008), water retention, and water quality (Brattebo and Booth, 2003). Considering that rooftops may represent as much as 40%–50% of the total impervious surfaces in urban areas, green roofs are among the key choices for hydrologic restoration and storm water management.

One of the key limiting factors in the wide use of LIDs is the lack of adequate modeling tools (Elliot and Trowsdale, 2007) that could be used to design LIDs that function properly for particular climate conditions. LIDs modeling requires an accurate description of the involved hydrological processes, which are multiple and interacting. In recent years, researchers have focused their attention on applying and developing empirical, conceptual, and physically-based models for the LIDs analysis. In their review article, Li and Babcock (2014) reported that there were more than 600 papers published worldwide involving green roofs, with a significant portion of them related to modeling.

Zhang and Guo (2013) developed an analytical model to evaluate the long-term average hydrologic performance of green roofs. Local precipitation characteristics were described using probabilistic methods, and the hydrological behavior of the system was described using the mass balance equations. Kasmin et al. (2010) developed a simple conceptual model of the hydrological behavior of green roofs during a storm event. The model input was the time series of precipitation events and the output was runoff. The water content in the green roof at any given time was between field capacity and the residual water content. Evapotranspiration was estimated using an empirical relationship accounting for the actual water contents, the storm event's characteristics, and the antecedent dry weather period. During a precipitation event, the

porous media absorbed moisture until field capacity was reached. Addition of further moisture produced subsurface flow.

She and Pang (2010) developed a physical model that combined an infiltration module (based on the Green-Ampt equation) and a saturation module (SWMM). The model calculates the water content in the GR in a stepwise manner from the initiation of precipitation until saturation. In simulating the hydraulic response of green roofs to precipitations, an infiltration module is used before the field capacity is reached and when no drainage is produced, while the saturation module is used after field capacity is reached and when drainage is produced. However, since runoff and infiltration can occur simultaneously during heavy precipitation, this stepwise approach may not be appropriate for a wide range of precipitation events.

Although analytical and conceptual models represent a viable alternative to the numerical analysis of green roofs, their use suffers from several limitations. Conceptualization of involved physical processes often leads to simplification of the system and a reduction of numerical parameters. While in a physical model each parameter has its own meaning, in conceptual models, lumped parameters often incorporate different components of the described process. These lumped parameters are case sensitive and need to be calibrated against experimental data, implying a lack of generality of the model itself. These drawbacks could represent a barrier to the use of modeling tools among practitioners who need reliable and generally applicable models.

Mechanistic models have proven to be a valid and reliable alternative to conceptual and analytical models for the analysis of green roofs and LIDs in general. Carbone et al. (2015) developed a one-dimensional finite volume model for the description of the infiltration process during rainfall events in green roof substrates. The model was based on the reduced advective form of the Richards equation, in which the soil water diffusivity was neglected. Metselaar (2012) used the SWAP software (van Dam et al., 2008) to simulate the one-dimensional water balance of a substrate layer on a flat roof with plants. Hilten et al. (2008) simulated peak flow and a runoff volume reduction of a 10-cm modular green roof (60×60 cm) using HYDRUS-1D (Šimůnek et al., 2008). In this study, only the values of field capacity and wilting point were

measured. These parameters, in conjunction with the soil bulk density and particle size distribution, were used to estimate the soil water retention curve using a pedotransfer function. Multiple 24 h storms were used to generate precipitation data and simulate runoff to describe the green roof's hydrologic response. Li and Babcock (2015) used HYDRUS-2D to model the hydrologic response of a pilot 61 x 61 cm green roof system. Physical properties of the substrate were obtained using laboratory measurements on soil cores extracted from a green roof. The saturated hydraulic conductivity was measured using the falling head method, while the residual and saturated water contents were measured using the gravimetric method. The hanging water column method was used to estimate the shape parameters of the unimodal van Genuchten function (van Genuchten, 1980). The model was calibrated using water content measurements obtained with TDR (Time Domain Reflectometer) sensors. The calibrated model was then used to simulate the potential beneficial effects of irrigation management on the reduction of runoff volumes.

Although physically based models have been widely and often successfully used, very few studies provided a comprehensive analysis of the hydrological behavior of a green roof and validated it against field-scale data. Moreover, studies that investigated the unsaturated hydraulic properties of green roof substrates were limited to the determination of some specific soil characteristics (e.g., field capacity, wilting point, or particle size distribution) and generally focused only on the soil water retention curves.

For these reasons, the aim of this paper is to give an accurate and comprehensive analysis of the hydrological behavior of green roofs using the mechanistic model HYDRUS-3D to analyze an extensive green roof installed at the University of Calabria. The problem was addressed in the following way. First, the soil water retention curve and the unsaturated hydraulic conductivity of the green roof substrate were measured using a simplified evaporation method. Obtained soil hydraulic parameters were then used in HYDRUS-3D numerical simulations of the green roof function using precipitation, climate, and subsurface experimental data for a two-month long period. The model was validated by comparing the

modeled and measured subsurface flows using the Nash-Sutcliffe efficiency index (J. E. Nash and Sutcliffe, 1970). Finally, the validated model was used to evaluate the hydrologic behavior of the green roof and its hydraulic response to single precipitation events.

2.2 Materials and Methods

2.2.1 Green Roof and Site Description

The University of Calabria is located in the south of Italy, in the vicinity of Cosenza (39°18' N 16°15' E). The climate is Mediterranean with a mean annual temperature of 15.5 °C and an average annual precipitation of 881.2 mm. The green roof is part of the “Urban Hydraulic Park,” which also includes a permeable pavement, a bioretention system, and a sedimentation tank connected to a treatment unit. An extensive green roof was installed on the existing rooftop of the Department of Mechanical Engineering. The original impervious roof was divided into four sectors. Two sectors are vegetated with native plants and differ from each other by the drainage layer. Another sector is characterized by bare soil with only few spontaneous plants. The last sector is the original impervious roof. The maximum depth of the soil substrate is 8 cm. This depth was selected to investigate both the energetic (heat fluxes) and hydrologic (water fluxes) behavior of a very thin extensive green roof under the Mediterranean climate. The soil substrate is composed of mineral soil with 74% of gravel, 22% of sand, and 4% of silt and clay. The soil has a measured bulk density of 0.86 g/cm³ and 8% of organic matter, which was determined in the laboratory using the Walkley-Black method. Three different plant species were selected and planted. *Cerastium tomentosum* and *Dianthus gratianopolitanus* are herbaceous plants suited for well drained soils; *Carpobrotus Edulis* is a succulent plant characterized by a high drought tolerance, largely due to the high leaf succulence and physiological adaptations such as CAM (Crassulacean Acid Metabolism) photosynthesis (Durhman et al., 2006). CAM plants have greater water use efficiency than C3

plants since transpiration per unit of CO_2 is reduced due to stomata openings at night for CO_2 uptake (Sayed, 2001).

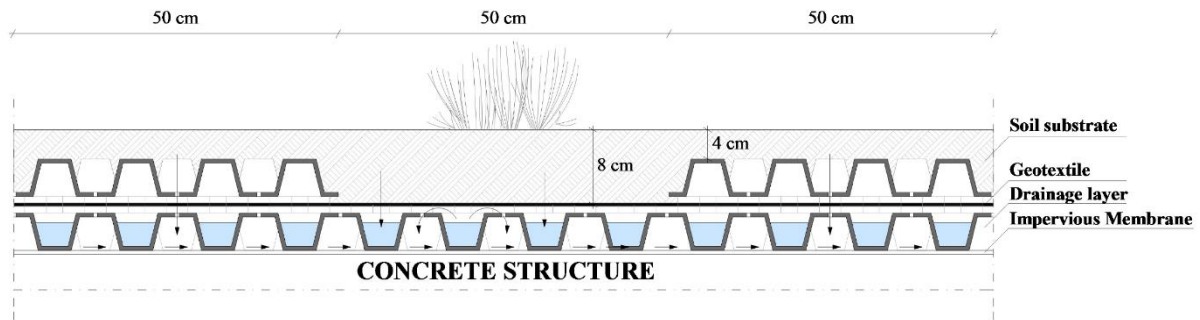


Figure 2.1 A typical cross-section of the GR.

In this study, only one vegetated sector of GR is considered. Figure 2.1 displays a cross-section of the GR; the considered sector has an area of 50 m^2 and an average slope of 1%. The GR is divided into square elements of $50 \times 50 \text{ cm}$ (Fig. 2.2), with alternating vegetated and non-vegetated areas. The substrate has a maximum depth of 8 cm where plants are grown and a minimum depth of 4 cm where no vegetation is present (Fig. 2.1, Fig. 2.2). This design was meant to minimize the weight on the GR support structure. A highly permeable geotextile is placed at the bottom of the substrate to prevent soil from migrating into the underlying layers. The drainage layer is composed of a polystyrene foam and is characterized by a water storage capacity of 11 l/m^2 and a drainage capacity of $0.46 \text{ l/s}\cdot\text{m}^2$. Water accumulated in the drainage layer can be transferred back up to the substrate only by condensation on the geotextile. An anti-root layer and an impervious membrane complete the GR.

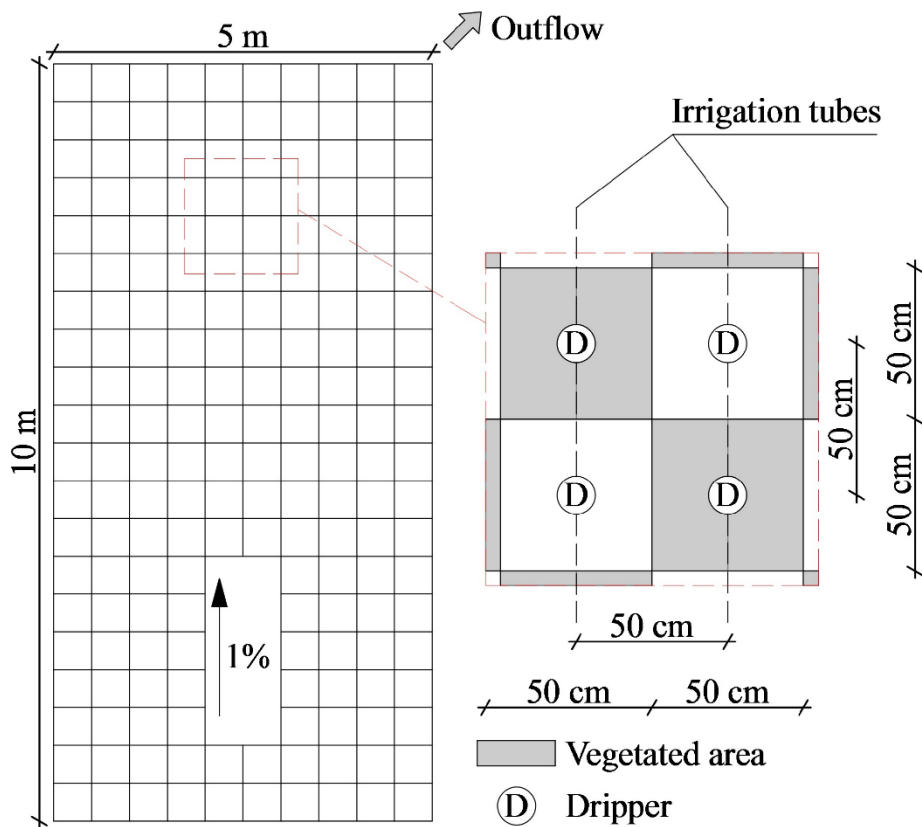


Figure 2.2 A schematic of the green roof, showing both vegetated (grey) and non-vegetated (white) areas. Irrigation drippers are indicated by a letter D.

A drip irrigation system was installed to provide water to plants during drought periods. The irrigation system is connected with a reuse system, which collects outflow from the GR. Only reused water was used for irrigating the GR. The reuse system is composed of a storage tank and a pump. When the storage capacity of the tank (1.5 m^3) is exceeded, water is directly discharged into the drainage system. Drippers are located at the center of each square and their distance from each other is approximately 50 cm. Drippers were also installed in non-vegetated areas in order to utilize water from the storage tank by using the evapotranspiration capacity of the GR. In this way, the volume of water discharged into the drainage system is reduced, and

the evaporative cooling effect of the GR on the building is expected to increase. The irrigation system is activated at predefined times by an electric valve, and the irrigation rate is measured by a water counter with an acquisition frequency of one minute. The total volume of irrigation for the selected time period was 142 mm.

A weather station located directly at the site measured precipitation, velocity and direction of wind, air humidity, air temperature, atmospheric pressure, and global solar radiation. Precipitation was measured using a tipping bucket rain gauge with a resolution of 0.254 mm and an acquisition frequency of one minute. Climate data were acquired with a frequency of five minutes. Data are processed and stored in a SQL database.

A flow meter located at the base of the building, composed of a PVC pipe with a sharp-crested weir and a pressure transducer, measured outflow from the GR. The pressure transducer (Ge Druck PTX1830) measured the water level inside the PVC pipe and had a measurement range of 75 cm, with an accuracy of 0.1 % of the full scale. The pressure transducer was calibrated in the laboratory using a hydrostatic water column, linking the electric current intensity with the water level inside the column. The exponential head-discharge equation for the flow meters was obtained by fitting the experimental data. The subsurface flow data were acquired with a time resolution of one minute and stored in a SQLITE database.

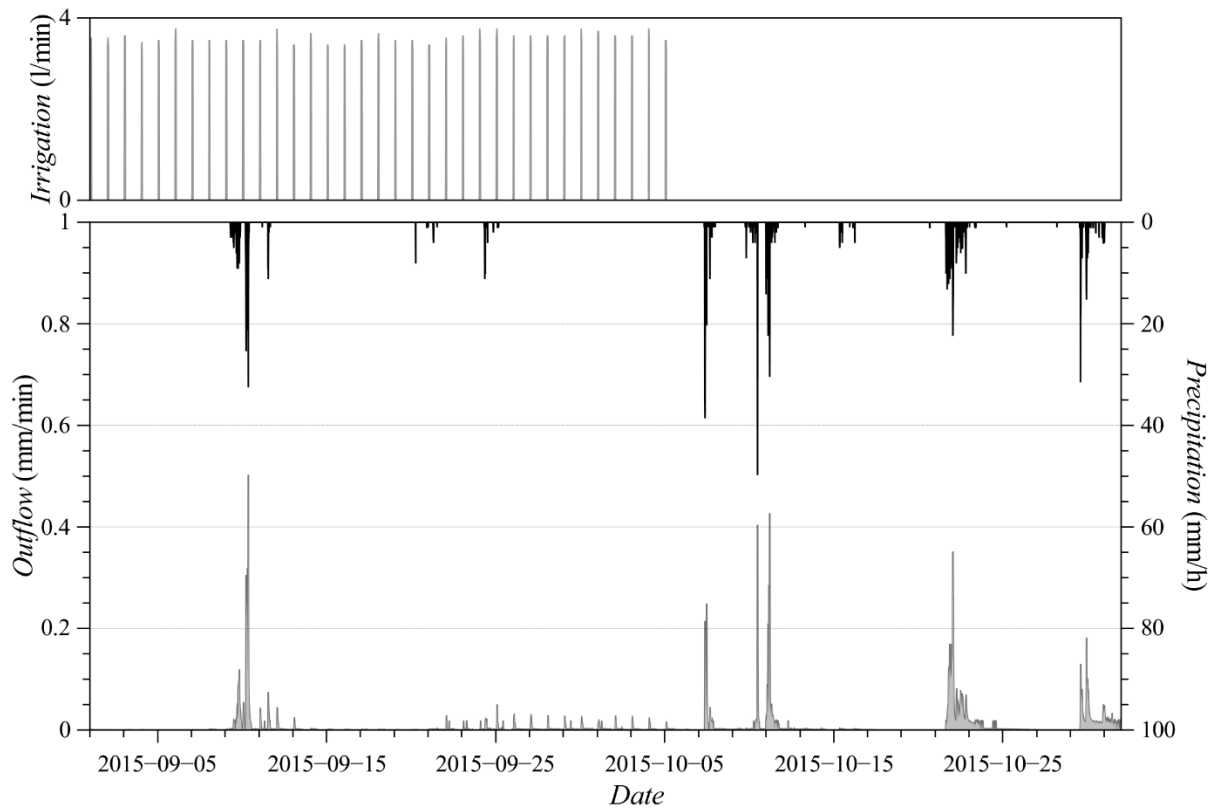


Figure 2.3 Measured precipitation (black), irrigation (top graph), and subsurface (gray) fluxes for a selected time period.

A two-month data set was selected for analysis (Fig. 2.3). This particular time period, which started on 2015-09-01 and ended on 2014-10-30, was selected because it involved highly variable climatic conditions. Isolated precipitations occurred in September, which had a relatively high average temperature. These climatic conditions required the irrigation of the GR for one hour during the night. October was characterized by intense and frequent precipitations. The total recorded precipitation for the whole period was 431 mm with an average air temperature of 20.2 °C.

Hourly reference evapotranspiration was calculated using the Penman-Monteith equation (Allen et al., 1998). An average value of albedo of 0.2 was used in calculations of net short-

wave radiation, assuming that the albedo for vegetated areas was 0.23 (Lazzarin et al., 2005) and 0.17 for bare soil (Rosenberg et al., 1983).

2.2.2 Soil Hydraulic Properties

2.2.2.1 Evaporation Method

Modeling of water flow in unsaturated soils by means of the Richards equation requires knowledge of the water retention function, $\theta(h)$, and the hydraulic conductivity function, $K(h)$, for each soil layer of the GR, where θ is the volumetric water content [L^3L^{-3}], h is the pressure head [L], and K is the hydraulic conductivity [LT^{-1}]. A broad range of methods exists for the determination of soil hydraulic properties in the field or in the laboratory (Arya, 2002; Dane and Hopmans, 2002; Klute and Dirksen, 1986). The numerical inversion of transient flow experiments represents one of the most accurate ways to determine soil hydraulic properties (Šimůnek et al., 1998). Among these, the simplified evaporation method (Schindler, 1980) is one of the most popular methods. Peters and Durner (2008) conducted a comprehensive error analysis of the simplified evaporation method and concluded that it is a fast, accurate, and reliable method to determine soil hydraulic properties in the measured pressure head range, and that the linearization hypothesis introduced by Schindler (1980) causes only small errors. The evaporation method was further modified by Schindler et al. (2010a, 2010b) to significantly extend the measurement range to higher pressures. For a detailed description of the modified evaporation method, please refer to Schindler et al. (2010a, 2010b).

A drawback of the evaporation method is that it is poorly suited for direct determinations of conductivities near saturation (Wendroth et al., 1993). The determination of hydraulic conductivities remains reliable only in the dry range, in which hydraulic gradients are more pronounced. To improve the characterization of the hydraulic conductivity function near

saturation, alternative methods are required such as the multi-step outflow method (Peters and Durner, 2008).

In this study, the simplified evaporation method with the extended measurement range (down to -9,000 cm) was used for the determination of the unsaturated hydraulic properties of the green roof substrate. For a complete description of the system, please refer to UMS GmbH (2015). The soil for the laboratory analysis was sampled directly from the GR using a stainless-steel sampling ring with a volume of 250 ml. The soil sample was saturated from the bottom before starting the evaporation test. The measurement unit and tensiometers were degassed using a vacuum pump, in order to reduce the potential nucleation sites in the demineralized water. Since Peters and Durner (2008) suggested a reading interval for structured soils of less than 0.1 day, the reading interval was set to 20 minutes in order to have high resolution measurements. At the end of the experiment, the sample was placed in an oven at 105°C for 24 hours and then the dry weight was measured.

2.2.2.2 Parameter Estimation

The numerical optimization procedure, HYPROP-FIT (Pertassek et al., 2015), was used to simultaneously fit retention and hydraulic conductivity functions to experimental data obtained using the evaporation method. HYPROP-FIT is a computer program designed to fit unimodal and multimodal retention functions to measured water retention data and to compute the corresponding relative hydraulic conductivity function. The fitting is accomplished by a non-linear optimization algorithm that minimizes the sum of weighted squared residuals between model predictions and measurements. The software uses the Shuffled Complex Evolution (SCE) algorithm proposed by Duan et al. (1992), which is a global parameter estimation algorithm. The software includes a corrected fit of the hydraulic functions by the “integral method” to avoid bias in hydraulic properties near saturation (Peters and Durner, 2006), an Hermitian spline interpolation of the raw measured data to obtain smooth and continuous time series of measured data, and an automatic detection of the validity range of

conductivity data near saturation, where the hydraulic gradients become too small to yield reliable data.

Two different models were evaluated for the description of soil hydraulic properties. The unimodal van Genuchten–Mualem (VGM) model (van Genuchten, 1980) was used first:

$$\Theta = \begin{cases} \frac{1}{(1 + (\alpha|h|)^n)^m} & \text{if } h \leq 0 \\ 1 & \text{if } h > 0 \end{cases} \quad (1)$$

$$\Theta = \frac{\theta - \theta_r}{\theta_s - \theta_r}$$

$$K = \begin{cases} K_s \Theta^L \left[\left(1 - \left(1 - \Theta^{\frac{1}{m}} \right) \right)^m \right]^2 & \text{if } h < 0 \\ K_s & \text{if } h > 0 \end{cases} \quad (2)$$

$$m = 1 - \frac{1}{n}$$

where Θ is the effective saturation (-), α is a parameter related to the inverse of the air-entry pressure head (L^{-1}), θ_s and θ_r are the saturated and residual water contents, respectively (-), n and m are pore-size distribution indices (-), K_s is the saturated hydraulic conductivity (LT^{-1}), and L is the tortuosity and pore-connectivity parameter (-).

Since the unimodal VGM model cannot always describe the full complexity of measured data, the bimodal model of Durner (1994), which constructs the retention and hydraulic conductivity functions by a linear superposition of two or more van Genuchten-Mualem functions, was used next:

$$\Theta = \begin{cases} \sum_{i=1}^2 w_i \left[\frac{1}{(1 + (\alpha_i |h|)^{n_i})^{m_i}} \right] & \text{if } h < 0 \\ 1 & \text{if } h > 0 \end{cases} \quad (3)$$

$$K = \begin{cases} K_0 \left(\sum_{i=1}^2 w_i \Theta_i \right)^L \left[\frac{\sum_{i=1}^2 w_i \alpha_i [1 - (1 - \Theta_i^{1/m_i})^{m_i}]^2}{\sum_{i=1}^2 w_i \alpha_i} \right] & \text{if } h < 0 \\ K_o & \text{if } h > 0 \end{cases} \quad (4)$$

where w is a weighing factor and i refers to the i th pore system.

Although the K_s value is commonly fixed to the measured value of the saturated hydraulic conductivity, some studies showed that this can introduce bias in the unsaturated hydraulic conductivity function when using the traditional VGM model. Schaap and Leij (1999) and Schaap et al. (2001) confirmed that fixing K_s to a measured value of the saturated hydraulic conductivity led to a systematic overestimation of hydraulic conductivity at most pressure heads. Furthermore, Schaap et al. (2001) demonstrated that the hydraulic conductivity estimated by fitting K_s provided a much better description of the hydraulic conductivity at negative pressure heads than fixing it at the measured saturated hydraulic conductivity. In addition, Schaap and Leij (1999) found that the fitted value of the tortuosity L was often negative with an optimal value of -1. For these reasons all the parameters were initially included in the optimization.

The goodness-of-fit was evaluated in terms of the Root Mean Square Error (RMSE), while the Akaike information criterion (AIC) (Hu, 1987) was used to choose between different hydraulic conductivity functions with different numbers of optimized parameters. The software also provides 95% confidence intervals to assess the uncertainty in parameter estimation.

2.2.3 Modeling Theory

2.2.3.1 Water Flow and Root Water Uptake

The HYDRUS-3D software (Šimůnek et al., 2008) was used to describe the morphological complexity of the green roof, which simultaneously includes multiple soil depths, both vegetated and non-vegetated areas, and drip irrigation. The green roof consists of four square elements, which are regularly repeated (Fig. 2.2). The hydrologic response of the entire GR can be well described as a superposition of the behavior of these four elements.

HYDRUS-3D is a three-dimensional model for simulating the movement of water, heat, and multiple solutes in variably-saturated porous media. HYDRUS-3D numerically solves the Richards equation for multi-dimensional unsaturated flow:

$$\frac{\partial \theta}{\partial t} = \nabla[K \cdot \nabla(h + z)] - S \quad (5)$$

where S is a sink term [$L^3L^{-3}T^{-1}$], defined as a volume of water removed from a unit volume of soil per unit of time due to plant water uptake. Feddes et al. (1978) defined S as:

$$S(h) = a(h) \cdot S_p \quad (6)$$

where $a(h)$ is a dimensionless water stress response function that depends on the soil pressure head h and has a range of values between 0 and 1, and S_p is the potential root water uptake rate. Feddes et al. (1978) proposed a water stress response function, in which water uptake is assumed to be zero close to soil saturation (h_1) and for pressure heads higher (in absolute values) than the wilting point (h_5). Water uptake is assumed to be optimal between two specific pressure heads (h_2 , h_3 or h_4), which depend on a particular plant. At high potential transpiration rates (5 mm/day in the model simulation) stomata start to close at lower pressure heads (h_3) (in absolute value) than at low potential transpiration rates (1 mm/d) (h_4). Parameters of the stress response function for a majority of agricultural crops can be found in various databases (e.g., Taylor and Ashcroft, 1972; Wesseling et al., 1991).

As explained above, GR plants were selected to suit Mediterranean climate conditions. Hanscom and Ting (1978) conducted a comprehensive experimental campaign on the behavior of succulent plants under water stress. They observed that during time periods with water and salt stress, plants closed their stomata and, as a consequence, little or no transpiration occurred even during day hours. Thus, the plants were capable of withstanding extended periods of drought. In the same study, well-watered plants exhibited normal C3-photosynthesis mechanisms with the maximum CO₂ uptake occurring during the day. This behavior was reported also in Starry et al. (2014). Considering that the combined effects of irrigation and precipitation is limited the drought periods, it appears reasonable to assume that a normal C3-mechanism occurred. For these reasons, parameters reported in Wesseling et al. (1991) for pasture were slightly modified in this study. In particular, h_1 and h_2 were set to -1 and -10 cm, respectively, to increase actual transpiration for near-saturated conditions. Parameters used in the water stress response function are reported in Table 2.1.

Table 2.1 Feddes' parameters for the water stress response function used in numerical simulations.

| Feddes' parameters | Pressure Head (cm) |
|--------------------|--------------------|
| h_1 | -1 |
| h_2 | -10 |
| h_3 | -200 |
| h_4 | -800 |
| h_5 | -8000 |

The local potential root water uptake S_p was calculated from the potential transpiration rate T_p . The Beer's equation was first used to partition reference evapotranspiration, calculated using the Penman-Monteith equation (Allen et al., 1998), into potential transpiration and potential soil evaporation fluxes (e. g., Ritchie, 1972). The Leaf Area Index (LAI) is needed to partition evaporation and transpiration fluxes. In this study, a LAI value of 2.29 as reported by

Blanusa et al. (2013) for a *sedum* mix was used in vegetated areas. For a detailed explanation of evapotranspiration partitioning, please refer to Sutanto et al. (2012).

As described above, the vegetated and non-vegetated GR elements alternate, while plants are located in the center of vegetated areas. HYDRUS-3D allows for the consideration of a spatially variable root distribution. A cylinder with a radius of 20 cm and a depth of 8 cm, in the center of the vegetated area, was used to model the root zone. The root density was assumed to be uniform inside of the cylinder and zero in the remaining part of the numerical domain. The total potential transpiration flux from a transport domain is in HYDRUS equal to potential transpiration T_p multiplied by the surface area associated with vegetation. This total potential transpiration flux is then distributed over the entire root zone for the computation of the actual root water uptake.

2.2.3.2 Numerical Domain and Boundary Conditions

The two main elements that form a GR are the soil substrate and the drainage layer. While the role of the substrate is well-known because it governs the dynamics of infiltration and evapotranspiration, the importance of the drainage layer for the hydraulic behavior of the GR is only partially described in the literature, especially with respect to the modeling of its function. The drainage layer is frequently modeled as an open reservoir (e.g., Locatelli et al., 2014; Vesuviano et al., 2014). Once the drainage layer's storage capacity is reached, the excess water is drained through holes into outflow drains. This guarantees a high permeability of the system and avoids the formation of ponding on top of the substrate layer even for intense precipitations. An open space of 1 cm separates the soil substrate and drainage holes (Fig. 2.1, Fig. 2.4).

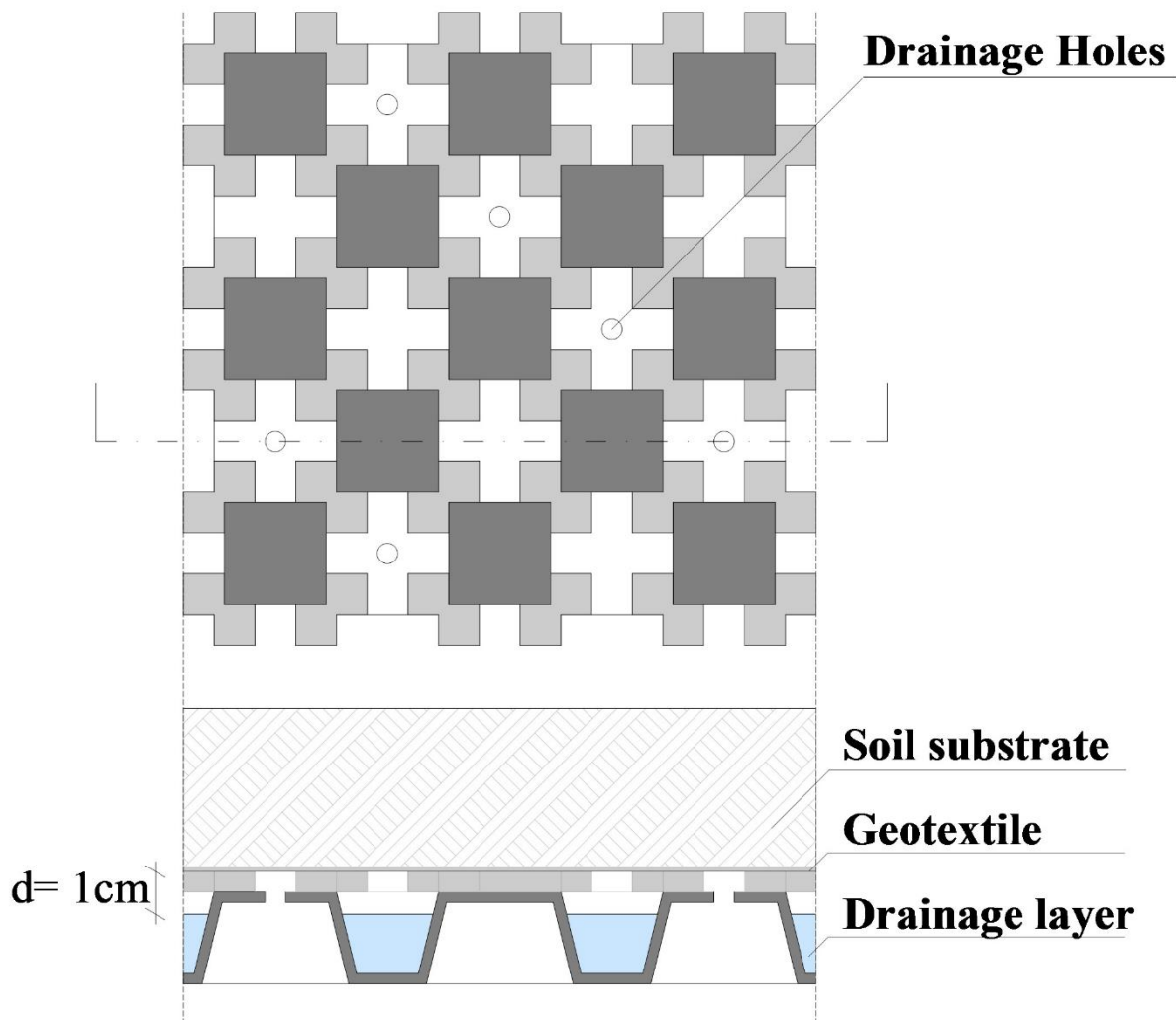


Figure 2.4 Details of the drainage layer, where d is the thickness of the open space between drainage holes, and the geotextile supporting the GR substrate.

Water accumulated in the drainage layer can return to the soil substrate only by evaporation and subsequent condensation on the geotextile at the bottom of the soil. In this small air-space, potential evaporation is expected to be limited due to microclimatic conditions, to which water in the drainage layer is exposed. The enclosed airspace is expected to be characterized by relatively high humidity, considering the combined effects of soil moisture

and the vicinity of the water table of the drainage layer. Moreover, radiation and air turbulence can be considered negligible in this enclosed airspace. The only factors that can thus produce evaporation are the air temperature and air humidity. However, the above considerations suggest that the effects of evaporation and micro-condensation can be neglected, especially at the field scale. This implies that variations of the water level in the drainage layer are limited and, consequently, the storage capacity of the drainage layer has only a limited effect on GR outflow. For these reasons, only the soil substrate is modeled in this study.

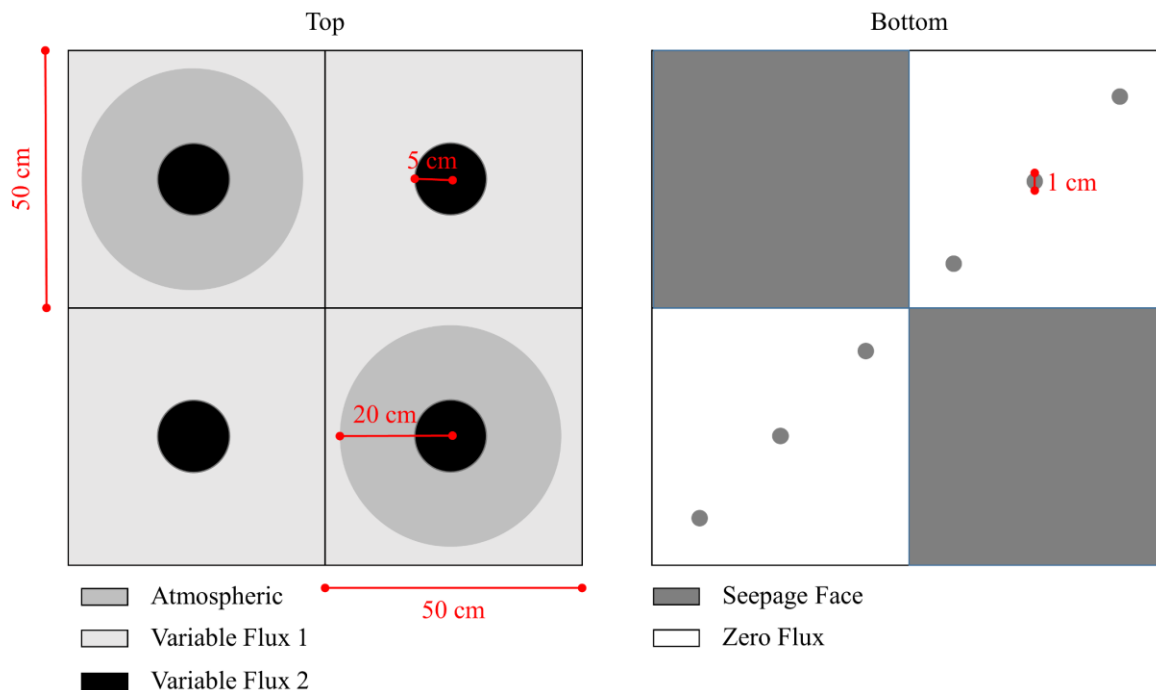


Figure 2.5 Spatial distribution of considered boundary conditions.

While precipitation and potential evaporation (different in vegetated and bare areas, see Table 2.2) were uniformly distributed on the soil surface, the drip irrigation was modeled in predefined surface points. Drippers can be idealized as point sources with a specified irrigation flux. However, if the irrigation flux is applied to a single boundary node and this flux exceeds

the infiltration capacity of this node, problems with numerical convergence can occur. To avoid such numerical problems, the irrigation flux should be distributed over a larger surface area, which should ideally represent the wetting radius. This area must be large enough to avoid surface ponding. In this study, the irrigation flux was distributed over a circular area with a radius of 5 cm, located in the center of each element. As a result, no ponding was observed during numerical simulations.

The surface of the green roof was thus exposed to precipitation, evaporation, and irrigation. As a result, three different boundary conditions were specified at the surface of the modeled domain, and two boundary conditions at its bottom (Fig. 2.5). Table 2.2 summarizes various fluxes considered in various types of used boundary conditions.

Table 2.2 Fluxes considered in different types of boundary conditions.

| BCs | Flux |
|-----------------|---|
| Atmospheric | Precipitation, potential evaporation ($=ET_0f^\dagger$), and potential transpiration ($=ET_0(1-f)$) |
| Variable flux 1 | Precipitation and potential evaporation |
| Variable flux 2 | Precipitation, irrigation, potential evaporation ($=ET_0f$), and potential transpiration ($=ET_0(1-f)$) |
| Seepage face | Seepage |
| Zero flux | No flux |

[†] ET_0 - reference evapotranspiration, f - distribution coefficient dependent on LAI (Ritchie, 1972)

The “Atmospheric” boundary condition, which was assigned to areas under vegetation, can exist in three different states: (a) precipitation and/or potential evaporation fluxes, (b) a zero pressure head (full saturation) during ponding when both infiltration and surface runoff occurs, and (c) an equilibrium between the soil surface pressure head and the atmospheric water vapor pressure head when atmospheric evaporative demand cannot be met by the substrate. The threshold pressure head, which was set to -30,000 cm, divides the evaporation process

from the soil surface into two stages: (1) a constant rate stage when actual evaporation, equal to potential evaporation, is limited only by the supply of energy to the surface, and (2) the falling rate stage when water movement to the evaporating sites near the surface is controlled by subsurface soil moisture and the soil hydraulic properties and when actual evaporation, calculated as a result of the numerical solution of the Richards equation, is smaller than potential evaporation.

A special option of HYDRUS-3D was used to treat the “Variable Flux” boundary conditions as the “Atmospheric” boundary conditions (i.e., with the limiting pressure heads described above). The “Variable Flux 1” boundary conditions included precipitation and potential evaporation and was assigned to bare soil areas. Since no vegetation was present in these areas, the reference evapotranspiration was not partitioned as for the “Atmospheric” boundary condition, but was fully assigned to potential evaporation. This approach shares some similarities with the “dual” crop coefficient introduced in FAO-56 (Allen et al., 1998):

$$ET_c = ET_0 \cdot (K_{cb} + K_e) \quad (7)$$

where ET_c is the actual crop evapotranspiration, ET_0 is the reference evapotranspiration, K_{cb} is the basal crop coefficient, and K_e is the empirical soil evaporation coefficient, which accounts for multiple factors affecting soil evaporation, such as soil texture and available soil moisture. In case of bare soil, K_{cb} becomes zero since no vegetation is present and ET_c is related only to the soil evaporation coefficient (Torres and Calera, 2010). In HYDRUS, soil evaporation is modeled using the two stage model with the threshold pressure head (described above), which directly accounts for factors affecting soil evaporation and which thus does not require the use of K_e .

The “Variable Flux 2” boundary condition, which involved precipitation, irrigation, and evaporation, was applied to the circular areas with a radius of 5 cm where drippers were located. A seepage face boundary condition was specified at the bottom of the soil substrate under vegetated areas since the geotextile is exposed to the atmospheric pressure. A seepage face boundary acts as a zero pressure head boundary when the boundary node is saturated and as a

no-flux boundary when it is unsaturated. In non-vegetated elements, a zero flux boundary condition was applied, except in small circular areas, which represented drainage holes (Fig. 2.1, Fig. 2.4). Three circular areas, each with a radius of 0.5 cm at the bottom of the non-vegetated elements, were modeled as seepage faces. Considering the occurrence of high nonlinearities and fluxes around these drainage holes, finite element mesh was refined here (to 0.5 cm) to guarantee a good accuracy of the numerical solution. “No flux” boundary conditions were used at the remaining boundaries.

The initial pressure head was assumed to be constant in the entire domain and was set equal to -330 cm, which is usually assumed to be the field capacity. The numerical model is expected to only be sensitive to the initial condition during the first few simulated days.

The three-dimensional simulated domain had a surface area of 1 m², a maximum height of 8 cm, and a total volume of 0.06 m³. The domain was discretized into three-dimensional prismatic elements using the MESHGEN Plus tool of HYDRUS-3D. No mesh stretching was used and the finite element (FE) mesh was isotropic. The generated FE mesh had 10,709 nodes and 49,027 three-dimensional elements. The quality of the FE mesh was assessed by checking the mass balance error reported by HYDRUS-3D at the end of the simulation. Mass balance errors, which in this simulation were always below 1%, are generally considered acceptable at these low levels.

2.2.4 Statistical Evaluation

The Nash-Sutcliffe Efficiency (NSE) index (J. E. Nash and Sutcliffe, 1970) was used to evaluate the agreement between measured and modeled hydrographs:

$$NSE = 1 - \left[\frac{\sum_{i=1}^T (Q_i^{obs} - Q_i^{mod})^2}{\sum_{i=1}^T (Q_i^{obs} - Q_{mean}^{obs})^2} \right] \quad (8)$$

where T is the total number of observations, Q_i^{obs} is the i th measured value, Q_i^{mod} is the i th simulated value, and Q_{mean}^{obs} is the mean value of observed data. The NSE index ranges between $-\infty$ and 1.0, is equal to 1 in case of a perfect agreement, and generally, values between 0.0 and 1.0 are considered acceptable (Moriassi et al., 2007). The NSE index was used because it is often reported to be a valid indicator for evaluating the overall fit of a hydrograph (Sevat et al., 1991).

2.3 Results and Discussion

2.3.1 Soil Hydraulic Properties

Soil hydraulic properties measured using the evaporation method are displayed in Figure 2.6. The soil water retention curve is well described across the entire water content range (Fig. 2.6). The retention data point close to $\log(h)=4$ (h in cm) was obtained by using the air-entry pressure head of the ceramic. At the first inspection, the behavior of the retention curve appears not to be perfectly sigmoidal, which may indicate the presence of a secondary pore system (Durner, 1994). Measured points of the hydraulic conductivity function are concentrated in the dry range between 10 and 30% of the volumetric water content. This is common when the evaporation method is used to measure soil hydraulic properties of coarse textured soils such as the substrate of the green roof.

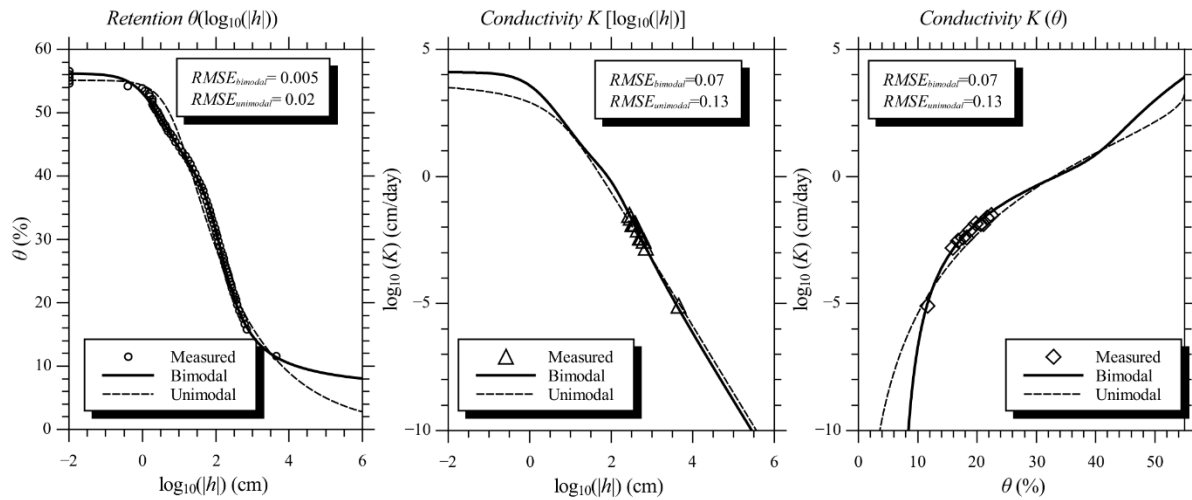


Figure 2.6 Measured and modeled values of the retention curve $\theta(\log_{10}(h))$ (left) and the hydraulic conductivity functions $K(\log_{10}(h))$ (center) and $K(\theta)$ (right). The measured values are scatter points, the full and dashed lines are the fitted bimodal and unimodal functions, respectively.

The measured data were imported into the HYPROP-FIT software to fit the analytical hydraulic property functions. The unimodal van Genuchten-Mualem model (van Genuchten, 1980) was fitted first. The $RMSE$ values for retention and conductivity functions were 0.02 ($\text{cm}^3\text{cm}^{-3}$) and 0.13 (in $\log K$, cm/day), respectively. An AIC of -874 was obtained when L was included in the optimization. The unimodal function introduced a high bias, especially in the hydraulic conductivity function. The bimodal Durner (1994) model (eqs. 3-4) was fitted next. The $RMSE$ values for retention and conductivity functions were 0.005 ($\text{cm}^3\text{cm}^{-3}$) and 0.07 (in $\log K$, cm/day), respectively. An AIC of -1298 was obtained when the value of L was fixed to 0.5, as this is the value usually assumed in the literature for many soils. Figure 2.6 displays a comparison between measured data and their fit using the unimodal and bimodal retention functions. The estimated soil hydraulic parameters with their confidence intervals are reported in Table 2.3.

Table 2.3 Estimated soil hydraulic parameters and their confidence intervals (CIs) for the unimodal and bimodal hydraulic functions.

| Parameter | Unimodal | CIs | Bimodal | CIs |
|--|----------|------|---------|-------|
| Residual water content, θ_r (-) | 0 | 0.05 | 0.070 | 0.007 |
| Saturated water content, θ_s (-) | 0.551 | 0.01 | 0.562 | 0.003 |
| Air-entry pressure head index for the first pore system, α_1 (1/cm) | 0.13 | 0.03 | 0.843 | 0.07 |
| Pore-size distribution index for the first pore system, n_1 (-) | 1.25 | 0.06 | 1.24 | 0.04 |
| Saturated hydraulic conductivity, K_S (cm/day) | 4700 | 3500 | 12600 | 3700 |
| Air-entry pressure index for the secondary pore system α_2 (1/cm) | - | - | 0.01 | 0.001 |
| Pore-size distribution index for the secondary pore system n_2 (-) | - | - | 1.97 | 0.08 |
| Weight coefficient w_2 (-) | - | - | 0.422 | 0.01 |
| Tortuosity and pore connectivity parameter, L (-) | 0.53 | 0.02 | 0.5 | - |

It is evident that the bimodal function provides a more accurate description of the retention curve. A significant difference between unimodal and bimodal functions emerges in the dry range between $\log(h) = 4$ and 6, where the unimodal function estimates lower water contents. The unimodal function overestimates the water contents in the range between $\log(h) = 0$ and 2 (h in cm). This is confirmed by the RMSE values, which are higher for the unimodal function, especially for the hydraulic conductivity function, for which the RMSE value is twice as large as for the bimodal function. The AIC value is higher (in absolute values) for the bimodal function, indicating that the model is better suited to describe the soil hydraulic properties of the evaluated soil than the unimodal model. Figure 2.6 displays measured data and the fitted multimodal retention and conductivity curves.

The change in the slope of the retention curve near saturation is reflected in the hydraulic conductivity function. However, this decrease in the hydraulic conductivity is not highly pronounced. Significant differences between the two hydraulic conductivity models occur only near saturation and in the dry range. The unimodal model estimates significantly lower hydraulic conductivity values close to saturation than the bimodal model. While the fitted

saturated water contents θ_s are almost the same for both models, significant differences exist in the residual water contents θ_r . Fitted values of θ_r are 0.0 and 0.062 for the unimodal and bimodal models, respectively. The value estimated by the unimodal model seems unrealistically low and it could indicate inaccuracy in the description of soil hydraulic properties in the dry range.

Both models indicate a soil characterized by a very high permeability, which corresponds well with the textural composition of the GR substrate. This characteristic is well suited for GR substrates, which must guarantee fast drainage and avoid water ponding on the surface even during intense precipitations. The volumetric water contents corresponding to the field capacity and the wilting point were 21 and 10 % for the bimodal model and 21 and 8% for the unimodal model, respectively.

The maximum correlation between optimized parameters for the bimodal model was 0.88 for θ_r and n_1 , a result that is quite common when only few points are measured in the dry range. However, only five correlation coefficients were higher than 0.8, indicating a generally well-posed problem. On the other hand, the maximum correlation coefficient for the unimodal model was 0.97 for θ_r and n , which indicates ill-posedness of the optimization problem. Narrow confidence intervals for parameters θ_r , θ_s , n_1 , α_2 , n_2 , and w_2 indicate high confidence in their estimation. The fitted saturated hydraulic conductivity K_s and the parameter α_1 for the first pore system exhibited the largest uncertainties. As explained above, the evaporation method is not accurate for the determination of the hydraulic conductivity near saturation, and this fact is reflected in the estimation of K_s . To improve the accuracy in the estimation of the hydraulic conductivity near saturation, other methods should be used.

The above discussed analysis suggests that the bimodal model could provide a slightly better description of the soil hydraulic properties than the unimodal model.

2.3.2 Model Validation

Parameters obtained with the evaporation method were used in HYDRUS-3D to describe the soil hydraulic properties of the GR substrate. Figure 2.7 shows a comparison between measured and simulated outflows from the GR when using both unimodal and bimodal functions of soil hydraulic properties.

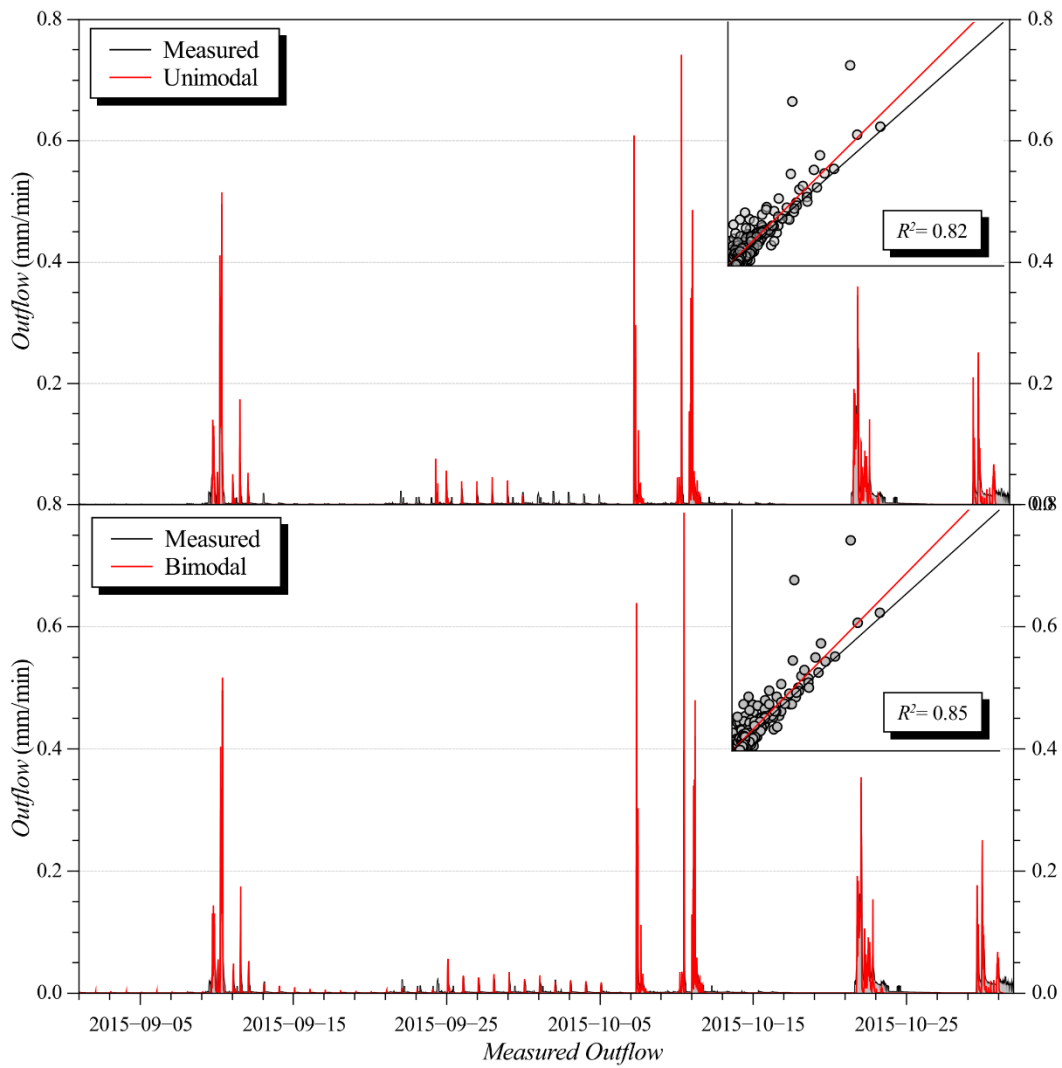


Figure 2.7 A comparison between measured and simulated outflows versus time and against each other (in the insert). The full and dashed lines in the insert are bisector and linear regression lines, respectively.

The NSE indices for measured and simulated GR outflows were 0.74 and 0.8 when the unimodal and bimodal functions were used, respectively. These values indicate that both models were able to accurately describe the hydraulic behavior of the GR, while a higher

accuracy was achieved by the bimodal model. It is evident from Figure 2.7 that the unimodal model failed in reproducing small outflows after irrigations, which were observed at the beginning and at the end of September. The inserts of Figure 2.7 show simulated against measured GR outflows. The same plot also shows a bisector line, which indicates a perfect agreement between simulated and measured outflows, and a linear regression line. The good performance of the models are confirmed by the determination coefficient $R^2= 0.85$ and 0.82 of the linear regressions for the bimodal and unimodal models, respectively. The comparison between bisector and regression lines indicates that both models slightly overestimated the outflow.

A further analysis of the fit between measured and simulated GR outflows was carried out by the analysis of the residuals, which is displayed in Figure 2.8 using a lag plot. The lag plot is constructed by comparing neighboring residuals with respect to time (i and $i-1$), where i is time with a measured value. A lag plot is useful for examining the dependency of the error terms. Any non-random pattern in a lag plot suggests that the variance is not random. No particular pattern emerges from the analysis of the lag plot, suggesting that the errors are random for both the unimodal and bimodal functions (Fig. 2.8).

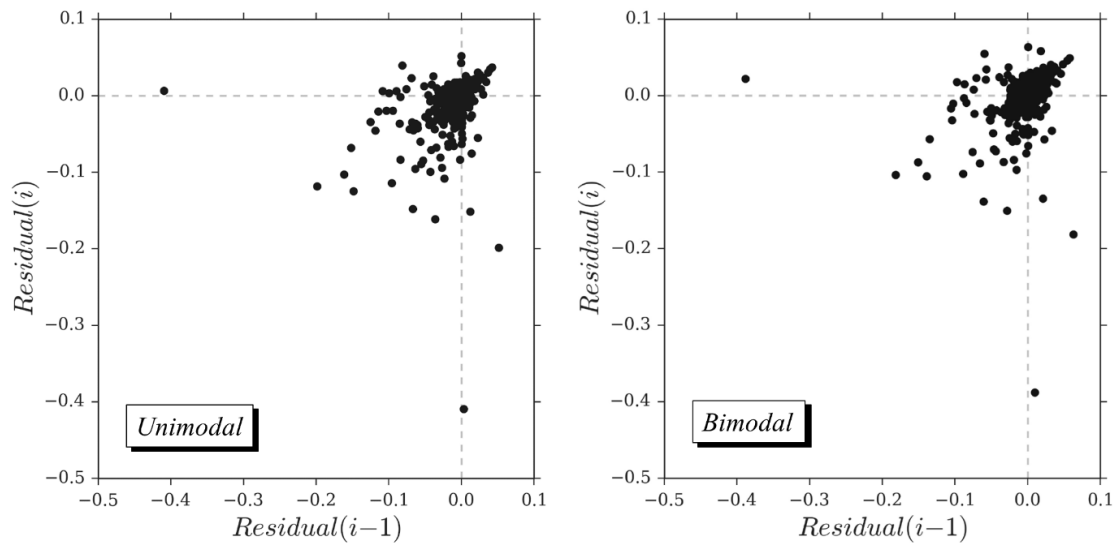


Figure 2.8 A lag plot of the residuals between measure and simulated outflows. Results are for the HYDRUS model with the unimodal (left) and bimodal (right) functions of soil hydraulic properties.

The bimodal model performs well during both dry and wet periods. In September, which is characterized by sparse precipitations, significant evapotranspiration, and daily irrigation, the model is able to reproduce both the fast response of the GR to precipitations and the small response to drip irrigation. This also indicates good accuracy in the estimation of daily fluctuations of soil water contents due to the combined effects of both evaporation and root water uptake.

The overestimation of the peak flux values (Fig. 2.7) can be related to the combined effects of uncertainties in measured precipitations and estimated unsaturated hydraulic conductivity. During large precipitation events, a significant part of the domain near the geotextile (a seepage face) becomes saturated or near-saturated, and in such conditions the hydraulic conductivity plays a fundamental role in the infiltration process. Considering the uncertainty and a possible bias introduced by the evaporation method for values of the hydraulic conductivity near saturation, it is reasonable to assume that the errors in predicted peak fluxes are related to this uncertainty. A more accurate description of the hydraulic

conductivity close to saturation should help in improving the accuracy of the model. Moreover, some uncertainty also arises from the evaluation of the soil depth in non-vegetated areas. Although an average depth of 4 cm was assumed, a slightly higher value may also be realistic considering the structure of the GR (Fig. 2.1, Fig. 2.4), and this would slightly modify the hydraulic response of the simulated GR.

It can be concluded that HYDRUS with both unimodal and bimodal functions of soil hydraulic properties can accurately describe the hydraulic behavior of the considered GR. The NSE indices are high and residuals are randomly distributed for both models, with a slightly better performance with the bimodal functions. Since the bimodal model has proven to be more accurate in reproducing the real behavior of the GR under small inflows, such as irrigation (Fig 2.7), it was selected for further analysis.

2.3.3 Hydrological Analysis of the Green Roof

Cumulative inflow and outflow fluxes of the GR are reported in Figure 2.9. The GR, coupled with the reuse system, was able to reduce the runoff volume by 25% during the considered period. Considering that the volume of water stored in the GR substrate was only 16 mm (3% of the total inflow), evapotranspiration was the main factor in reducing the runoff volume. The steep gradients in cumulative outflow (Fig. 2.9) indicate that the GR had a fast response to precipitations with a negligible delay in the hydrograph. This aspect is directly related to the limited thickness of the GR, which reduces the possible delay effect. On the other hand, cumulative outflow appeared flat when the irrigation was applied. This behavior is particularly evident in September when only negligible outflow fluxes were observed. At the beginning of October, cumulative outflow started to exhibit an increasing trend, caused by variations in actual evapotranspiration, as confirmed by the model. Figure 2.10 shows simulated actual root water uptake and evaporation from vegetated areas.

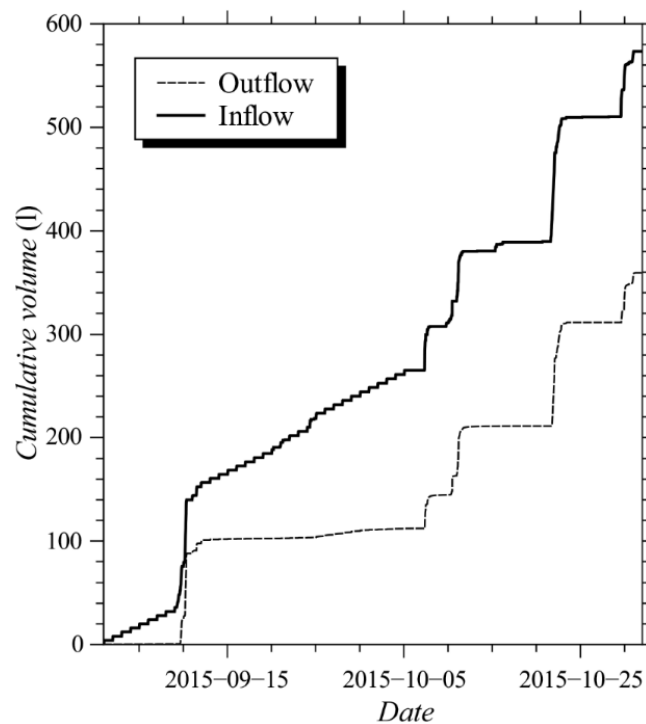


Figure 2.9 A comparison between cumulative inflow and outflow from the GR, simulated by HYDRUS-3D.

The first part of September (Fig. 2.10) was characterized by relatively high evapotranspiration, which lowered water contents in the soil substrate. As a consequence, only negligible outflow was produced by irrigation. The evapotranspiration rate dropped during the rain events between 2015-09-09 and 2015-09-11 due to the combined effects of high air humidity and low solar radiation. At the end of September, due to the irrigation and lower evapotranspiration rates, the soil water contents were higher and actual transpiration lower. This behavior is shown in detail in Figure 2.13. Between 2015-09-25 and 2015-09-30 the water content in vegetated areas ranged between 0.45 and 0.50, which corresponded to a pressure head range between -10 and -3 cm. In this pressure head range, plants transpiration is limited because of anaerobic conditions induced by high soil water contents (see the Feddes parameters in Table 2.3). Under these conditions, significant outflow was measured after irrigations (Fig.

2.3). This indicates that the model reproduced the dynamics of evapotranspiration in the GR with good accuracy, and that the parameters chosen for the water stress function are reasonable.

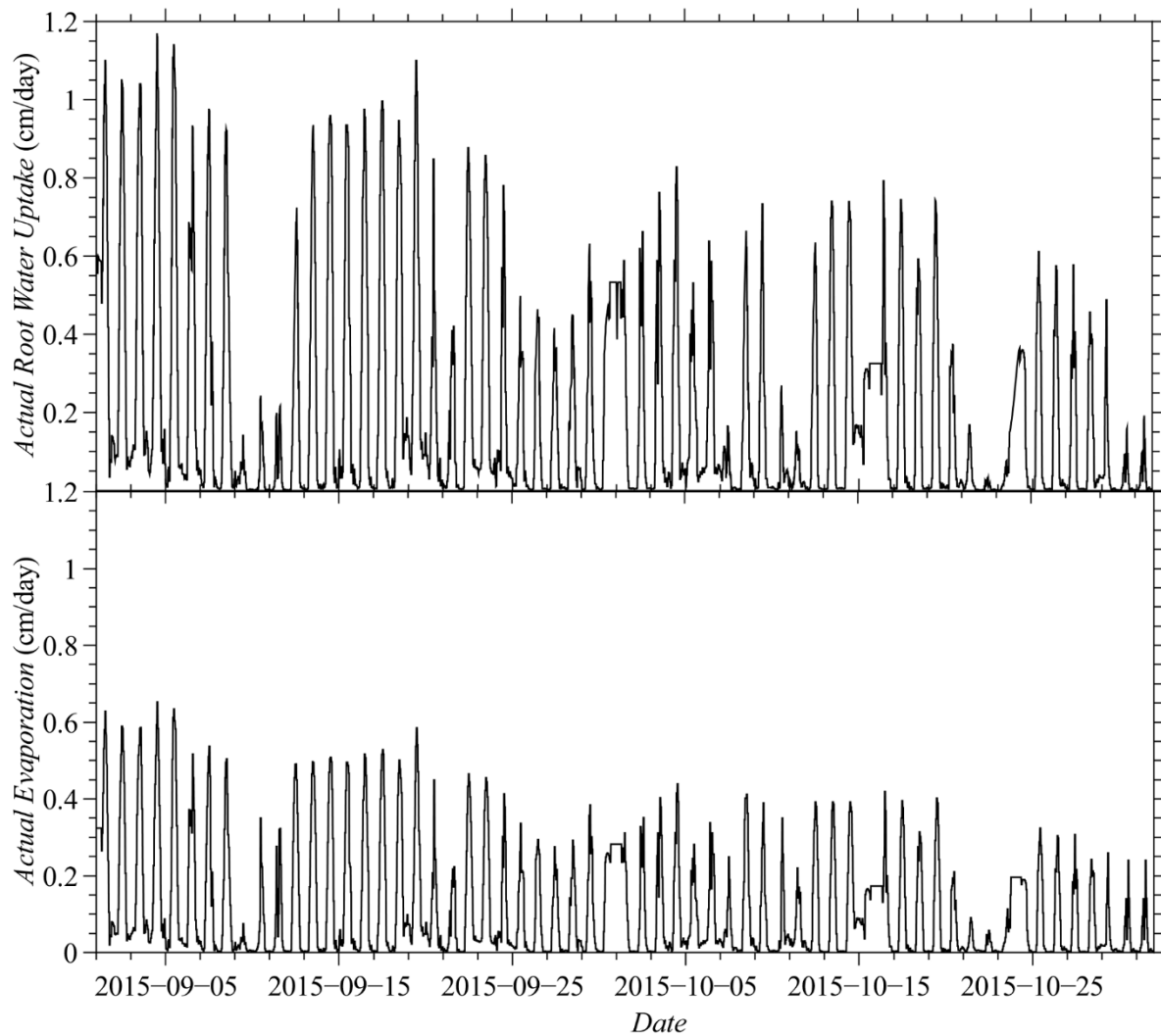


Figure 2.10 Simulated actual root water uptake (top) and evaporation (bottom) from vegetated areas of the green roof.

The comparison between pressure heads at the bottom of vegetated and non-vegetated areas of the GR helps in identifying the different hydraulic responses of these two sections (Fig.

2.11). Before irrigation started, the bottom pressure head in the non-vegetated section was higher (in absolute value) than in the vegetated section. This indicates that the non-vegetated section dried out more and faster than the vegetated section due to its very low thickness. As irrigation started, the pressure head quickly increased in the non-vegetated section, reaching the seepage condition and producing outflow. On the other hand, in the vegetated section, the pressure head only approached the seepage condition without generating outflow. This indicates that only the non-vegetated section of the GR was responsible for outflow after irrigation, and that the irrigation system could be optimized to avoid the formation of outflow after irrigations.

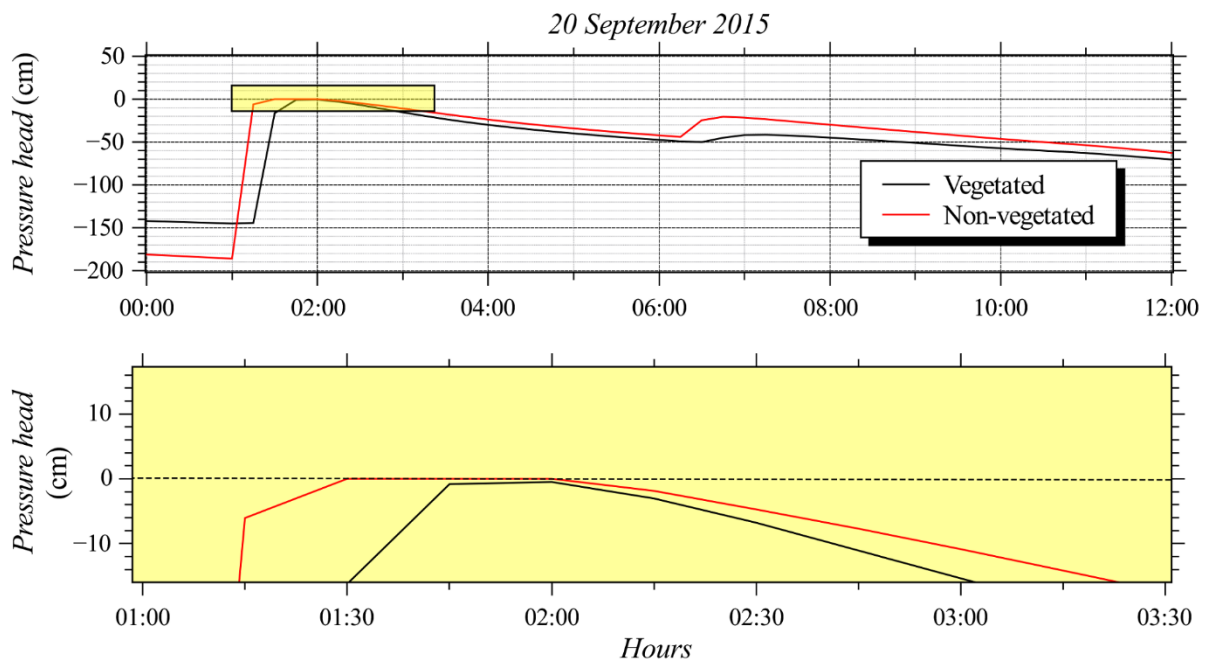


Figure 2.11 Pressure heads at the bottom of the vegetated (black) and non-vegetated (red) sections of the GR simulated by HYDRUS-3D. The yellow rectangular area in the top figure is expanded in the bottom figure. The dashed line represents a seepage condition.

2.3.4 Hydrological Performance during Precipitation Events

The hydrological response to single precipitation events is an important characteristic in the analysis of GRs and LIDs in general. The measures such as peak flow reduction P_{red} (%), the peak flow delay t_{del} (min), and the volume reduction V_{red} (%), provide information about the hydrological benefits of the LID system to the urban drainage system. Four distinct rainfall events of a significant magnitude, one in September and three in October, were identified for further analysis of the hydrological performance of the green roof for single precipitation events. Figure 2.12 shows precipitation, measured and modeled outflow fluxes for each precipitation event, as well as the total volume of the entire precipitation event V_{prec} (mm) and measures P_{red} and V_{red} .

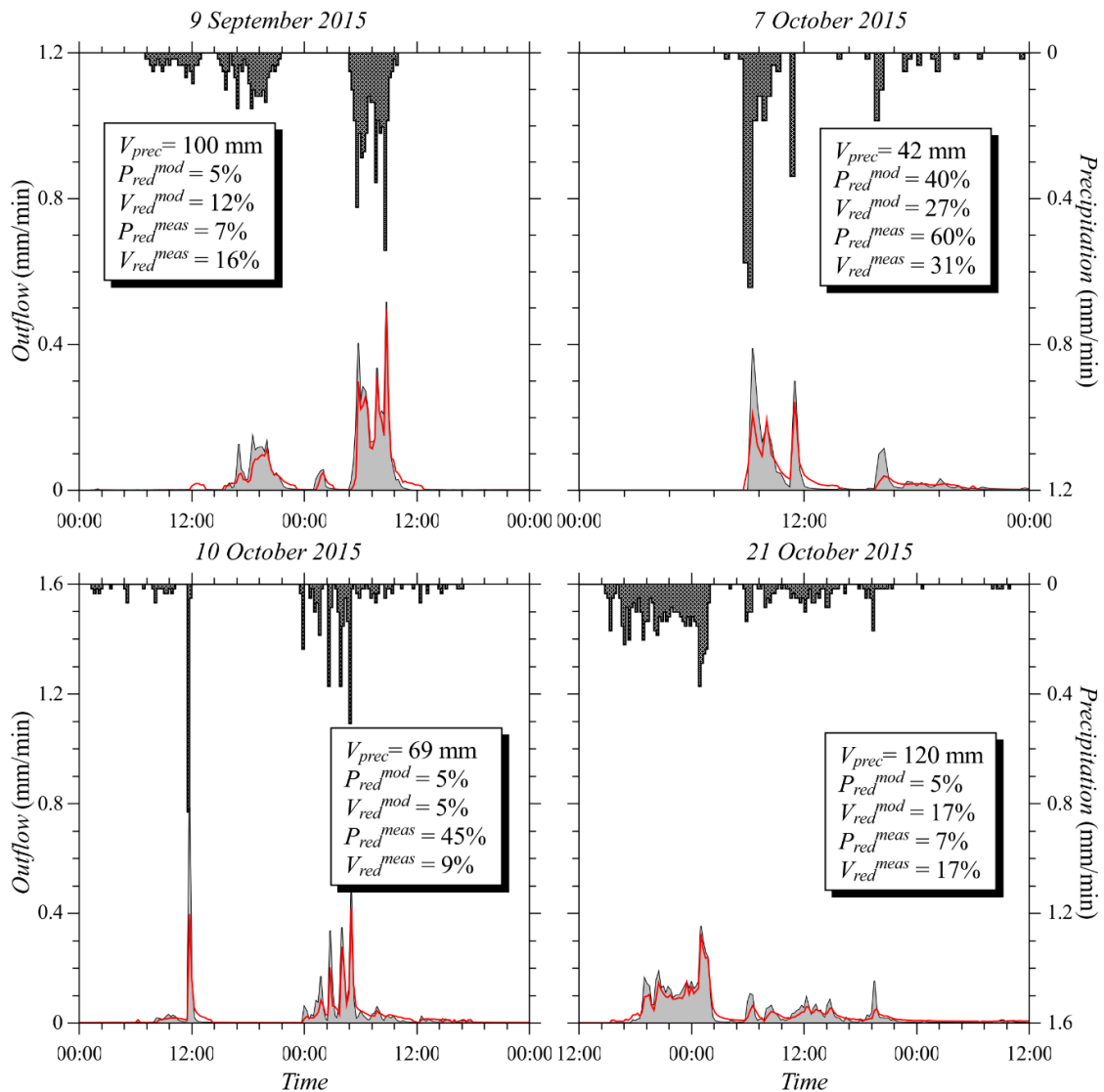


Figure 2.12 Precipitation (dark area), modeled (grey area) and measured (red line) outflow for four selected rainfall events in the analysis of the hydrological performance of the GR during single precipitation events.

It is evident from Figure 2.12 that the model exhibited good accuracy in reproducing the GR hydraulic response also for single precipitation events. Modeled V_{red} and P_{red} are in agreement with information reported in the Model Validation section. The model tended to

overestimate the peak flow especially for precipitations characterized by an early peak (7 October 2015 and 10 October 2015), while the accuracy was very high for precipitations with a delayed peak (9 September 2015 and 21 October 2015). Modeled volume reductions were sufficiently accurate. Only the analysis of the precipitation event on October 21 exhibited a significant deviation between the measured and modeled volume reductions.

The hydrological response of the GR varied considerably for different precipitation events. Delay time t_{del} was on the order of 15 minutes in all events, indicating that the delay effect was limited due to the limited thickness of the substrate. The largest P_{red} and V_{red} were observed for the event of October 7. In this event, the precipitation peak occurred at the beginning of the event, which was preceded by more than two days of a dry period since irrigation was stopped on October 5. Under these conditions, peak flow was partially attenuated by the relatively low initial water content of the soil substrate (Fig. 2.13). The effective volume reduction of the precipitation event (V_{eff}) was 13 mm.

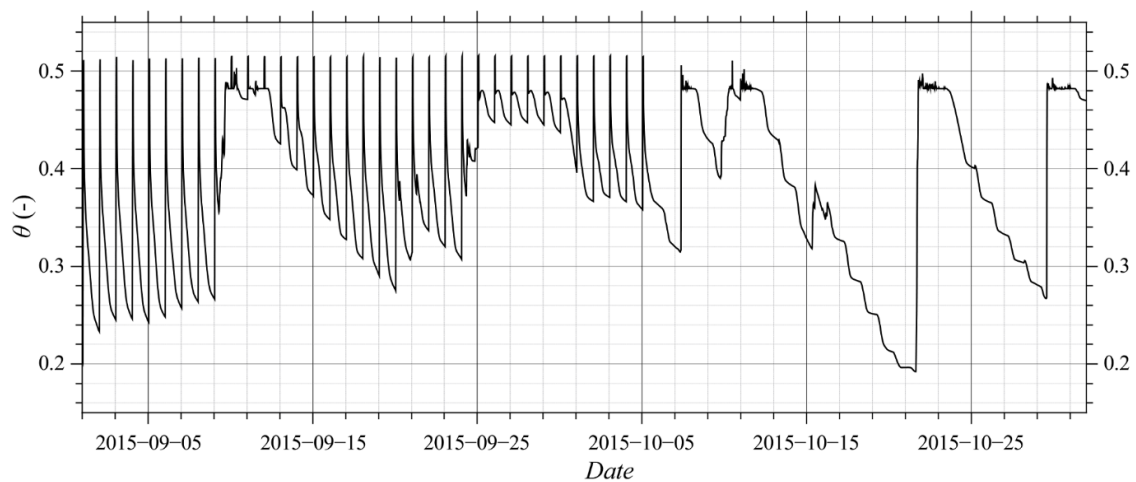


Figure 2.13 Simulated water contents in the vegetated section of the GR at a depth of 4 cm.

Although the precipitation event of October 10 was also characterized by an early peak, the measured peak reduction of 45% was lower than the one measured on October 7. This can be attributed to the higher water content at the beginning of the event. While on October 7 the initial water content was about 0.32, it was about 0.39 on October 10. The higher water content on October 10 resulted in a lower attenuation capacity of the substrate. For the events of September 9 and 21, P_{red} was only 7%. In both events, peak flow was preceded by low intensity precipitation, which increased the soil water content and as a consequence lowered the capacity of the GR to attenuate the peak of precipitation. The effective volume reduction for the event (V_{eff}) of October 21 was 20.4 mm, which was the highest among all of the other evaluated precipitation events. Before this event started, the water content of the substrate reached the lowest value of 0.2, significantly increasing the soil storage capacity.

It can be concluded that the GR response to precipitation, during the analyzed period, was influenced primarily by the antecedent substrate moisture and secondarily by the precipitation pattern. Positively-skewed and leptokurtic precipitation distributions tended to exhibit the largest peak flow reduction, while negatively-skewed and platykurtic precipitation distributions were likely to cause smaller peak reductions. The volume retained by the GR was mainly determined by the initial substrate moisture and it was independent of the precipitation pattern. It must be emphasized that these conclusions are not general, but restricted to the specific investigated GR. The validated model could be used in a sensitivity analysis, in which, together with other factors (e.g., substrate moisture, slope, substrate depth, etc.), the effect of the precipitation pattern on the GR response can be investigated using synthetically designed storms (Carbone et al., 2015b).

2.4 Conclusions

The goal of this study was to provide a comprehensive numerical analysis of the hydrological behavior of a green roof. The widely used mechanistic model HYDRUS-3D was

used to model the GR installed at the University of Calabria's hydrological responses to precipitation, evapotranspiration, and irrigation fluxes. The GR was characterized by a high degree of complexity; it included different soil depths, vegetated and non-vegetated areas, and non-uniformity in the boundary conditions.

Moreover, considering the lack of studies with regards to the unsaturated hydraulic properties of soil substrates in GRs, the simplified evaporation method was used to determine both the soil water retention curve and the unsaturated hydraulic conductivity function of the soil used in the GR. The soil exhibited a bimodal pore structure, characterized by a weakly pronounced secondary pore system and a high hydraulic conductivity. The bimodal functions proposed by Durner (1994) best represented the hydraulic properties of the substrate. The unimodal van Genuchten-Mualem relationships were also tested, but their description of unsaturated hydraulic properties was less accurate, especially for the unsaturated hydraulic conductivity.

Soil hydraulic parameters obtained from the evaporation method were then used in HYDRUS-3D to model the hydrological behavior of the green roof during a two month time period. Both the unimodal and bimodal functions of soil hydraulic properties were used in the analysis. The numerical simulation considered precipitation, evaporation, root water uptake, and irrigation. The Feddes model was used to represent the water stress response function of plants installed on the green roof. The Feddes' parameters were adjusted by taking into account the behavior of succulent plants such as *Carpobrotus Edulis* under different soil water content regimes. The Nash-Sutcliffe efficiency index was used to compare the simulated and measured outflows. The *NSE* indices were 0.74 and 0.8 for the model predictions with the unimodal and bimodal functions, respectively, indicating a good accuracy. Both models slightly overestimated some outflow fluxes. The randomness of the residuals was confirmed by the absence of evident patterns in the lag plot. The main difference between the two models was in the description of the hydraulic behavior of the GR after irrigations. While the unimodal model failed in reproducing small measured outflows, the bimodal model gave a more accurate

description. This further confirmed the accuracy of this model. The validated model with bimodal functions was used to analyze the hydrological performance of the GR during the entire simulation period and to investigate its hydrological response to single precipitation events. About 25% of the total inflow volume was returned to the atmosphere by evaporation and transpiration. The analysis of simulated pressure heads revealed that the non-vegetated section of the GR was responsible for small outflow fluxes following irrigations. This suggests that the irrigation system could be further optimized. The analysis of the hydrological response of the GR to single precipitation events highlighted the importance of the initial soil moisture for the volume and peak flow reductions. Furthermore, the analysis revealed that positively-skewed and leptokurtic precipitation distributions are likely to exhibit the largest peak flow reduction. The volume reduction is mainly influenced by the initial soil moisture and is insensitive to the precipitation pattern.

The performance of the model can be improved by a better description of the soil hydraulic properties, especially near saturation, considering that during intense precipitation events significant portions of the domain become saturated. Moreover, uncertainties in rainfall measurements and in geometric characteristics of the GR can introduce a further bias to the simulated results. A sensitivity analysis followed by an uncertainty analysis can help in identifying the most sensitive parameters and address the source of uncertainty (e.g., Brunetti et al., 2016a). Nevertheless, it can be concluded that the use of measured soil hydraulic properties with a mechanistic model can represent a valuable tool for the analysis of green roofs and other LIDs, and can boost the widespread adoption of such systems as a viable alternative to traditional urban drainage systems.

Chapter 3 A comprehensive numerical analysis of the hydraulic behavior of a permeable pavement

3.1 Introduction

Progressing urbanization, connected with the demographic growth of the last decades, has led to an increase in impervious surfaces in urban catchments at the expense of natural areas. This long-term process has resulted in the alteration of the natural hydrological cycle by reducing the infiltration and evaporation capacity of urban catchments, increasing surface runoff, and reducing groundwater recharge. While some studies highlighted a decrease of recharge as a result of an increase of impervious surfaces, other studies identified an increase in recharge due to the leakage of water from an urban infrastructure, such as sewer and water supply systems. The effect of urbanization on groundwater recharge is discussed in detail by Price (2011).

Another important factor is that the frequency of extreme rainfall events, characterized by high intensity and short duration, is expected to increase in the near future as a consequence of climate change (Kundzewicz et al., 2006; Min et al., 2011). For example, a recent study of Wasko and Sharma (2015) identified a strong correlation between intense precipitation peaks and high temperatures. They concluded that the expected global warming could lead to an increase of short-duration floods. The correlation between atmospheric temperature and extreme rainfall intensities was also confirmed in other studies (e.g., Westra et al., 2014). This will be accompanied by a more frequent occurrence of flooding events in urban areas (Carbone et al., 2015b).

The traditional approach to urban drainage systems focuses on collecting stormwater in piped networks and transporting it off-site as quickly as possible. The increasing frequency of flooding events proves that a new design paradigm for drainage systems is needed. This approach must aim to restore the natural hydrological cycle of urban catchments by increasing their evapotranspiration and infiltration capacity. In recent years, Low Impact Development (LID), an innovative approach to land development, has gained increasing popularity. LID is a 'green' approach for stormwater management that seeks to mimic the natural hydrology of a site using decentralized micro-scale control measures (Coffman, 2002). LID practices consist of bioretention cells, infiltration wells/trenches, stormwater wetlands, wet ponds, level spreaders, permeable pavements, swales, green roofs, vegetated filter/buffer strips, sand filters, smaller culverts, and water harvesting systems. Several studies have evaluated the benefits of LIDs. For example, Newcomer et al. (2014) used a numerical model to demonstrate the benefits of LIDs, in particular of an infiltration trench, on recharge and local groundwater resources for future climate scenarios. In another paper, Berardi et al. (2014) demonstrated how green roofs may contribute to the development of more sustainable buildings and cities. Environmental benefits included ecological preservation, mitigation of air and water pollution, enhancement of urban hydrology, a decrease of urban heat island effects, a reduction of energy consumption, etc. Furthermore, green roofs were able to significantly reduce storm-water runoff and retain rainfall volume with retention efficiencies ranging from 40% to 80% (Bengtsson et al., 2004); bioretention cells were shown to reduce average peak flows by at least 45% during a series of rainfall events in Maryland and North Carolina (Davis, 2008). Even though the results of available studies are encouraging, more research is needed to precisely assess the impact of LIDs on the hydrological cycle.

Most impervious surfaces in urban catchments consists of roofs, roads, parking lots and road shoulders. The development of any large impervious surface commonly leads to multiple impacts on stream systems. These impacts include higher peak stream flows, which cause channel incision, bank erosion, and increased sediment transport (Trimble, 1997; Whipple et

al., 1981). Another consequence of these impervious surfaces is the reduction of infiltration, which lowers groundwater recharge (Rose and Peters, 2001) and potentially also stream base flow (DeWalle et al., 2000; Simmons and Reynolds, 1982). Permeable pavements represent one solution to the problem of increased stormwater runoff and decreased stream water quality. They can consist of a surface concrete layer, a filter layer made of sand and other materials, a stony base, and sub-base layers. Permeable pavements offer great advantages in terms of runoff reduction (Collins et al., 2008), water retention, and water quality (Brattebo and Booth, 2003).

In spite of many well-known benefits of permeable pavements and other LID practices, the transition to sustainable urban drainage systems is very slow. One of the key limiting factors in the widespread adoption of such systems is the lack of adequate analytical and modeling tools (Elliot and Trowsdale, 2007). The availability of an effective LID modeling software could encourage a wider adoption of LID principles. Although several stormwater models can be applied to the LID analysis (Elliot and Trowsdale, 2007), most of them do not incorporate accurate descriptions of hydrological processes involved, which leads to inaccurate predictions. Moreover, existing tools do not incorporate automatic parameter optimization techniques and sensitivity analysis routines, which have proven to be fundamental when the model includes multiple parameters. In recent years, researchers have focused their attention on applying and developing physically-based models for the LID analysis (Carbone et al., 2015a), however more research is still needed in this direction.

For example, the HYDRUS software suite (Šimůnek et al., 2008) has been widely used in the literature for the description of the hydraulic behavior of green roofs (Hilten et al., 2008; Li and Babcock, 2015; Newcomer et al., 2014; Palla et al., 2009), with excellent agreement between numerical simulations and experimental data. Newcomer et al. (2014) investigated the effects of LIDs on recharge. In their study, the HYDRUS-2D software was used to simulate flow from an infiltration trench and an irrigated lawn installed at the San Francisco State University. While the model was calibrated by comparing the simulated and measured recharge, only few details were given about the calibration procedure. The calibrated model was then used to simulate the behavior of LIDs for future precipitation scenarios. Hilten et al.

(2008) used HYDRUS-1D to study the effectiveness of green roofs in mitigating stormwater. Simulations were run using HYDRUS-1D for a 24-h design storm to determine peak flow, retention, and detention time of runoff. Li and Babcock (2015) used HYDRUS-2D to model the hydrologic response of a pilot green roof system. The root-mean-square error deviation (RMSD) between the modeled water contents and field measurements ranged between 0.38 and 1.74%. This suggests that the use of mechanistic models, such as HYDRUS, represents one of the most valuable alternatives to empirical and conceptual models for the LID analysis.

Among all LID practices, permeable pavements are the practices that are most lacking modelling tools capable of describing their hydraulic behavior. The heterogeneity of materials that compose a permeable pavement, together with the high infiltration rates (Brattebo and Booth, 2003), which may lead to preferential flow and especially in the base and sub-base layers, pose complex problems in the numerical modeling of these systems. Very few modeling tools exist in the literature for permeable pavements. One of them is included in the Storm Water Management Model (SWMM) (Gironás et al., 2010). However, results obtained by SWMM have proven to be inaccurate, especially in the description of the effects of base and sub-base layers on the infiltration processes (Zhang and Guo, 2015). HYDRUS has also been used for the description of variably-saturated flow in permeable pavements. Illgen et al. (2007) used HYDRUS-2D for the numerical analysis of a permeable pavement and calibrated the model against experimental data collected at a laboratory test facility. The calibrated model was then used to simulate different scenarios not investigated during the laboratory campaign. The Illgen et al. (2007) study provided only limited details about the calibration of soil hydraulic parameters and their uncertainty and sensitivity. The occurrence of preferential flow in the permeable pavement was also not investigated. Moreover, the model was used to simulate a laboratory test facility, the behavior of which may differ from a field scale experimental facility. On the other hand, Carbone et al. (2014) used HYDRUS-1D to model a permeable pavement at the field scale. The HYDRUS-1D model was calibrated against four different rainfall events with optimal results. In this study, the permeable pavement was

modeled as a single homogeneous layer and the differences between hydraulic properties of different layers were neglected. Furthermore, the numerical simulations were event-based. In both studies, calibration of soil hydraulic properties was carried out manually without taking advantage of more recent global optimization algorithms. This indicates that research in this direction is limited, with only inconclusive results that need to be further investigated.

The lack of studies that provide a comprehensive description of the hydraulic behavior of a permeable pavement at the field scale and that propose a general methodology for the estimation of its hydraulic parameters suggests that research is particularly needed in the development and identification of accurate modeling tools for the analysis of LID practices, especially for permeable pavements. The aim of this study is to investigate the suitability of the HYDRUS mechanistic model to correctly describe unsaturated flow in typical permeable pavement, installed at the experimental site of the University of Calabria. Multiple uniform and nonequilibrium flow models included in HYDRUS-1D, such as single- and dual-porosity models, are used to describe the hydraulic behavior of the permeable pavement. The problem is addressed in the following way. First, a Global Sensitivity Analysis (GSA) is carried out to prioritize hydraulic parameters and identify those that are non-influential. Results of the GSA, combined with a Monte Carlo filtering approach, are used to investigate the parameter space and identify *behavioral* regions. These regions are then used in the calibration process conducted with the Particle Swarm Optimization (PSO) algorithm. The use of PSO for the determination of unsaturated hydraulic properties represents a new important application of this method. Finally, the calibrated model is validated on an independent set of measurements.

3.2 Materials and Methods

3.2.1 Site Description

The University of Calabria is located in the south of Italy, in the vicinity of Cosenza (39°18' N 16°15' E). The climate is Mediterranean with a mean annual temperature of 15.5 °C and an average annual precipitation of 881.2 mm. The permeable pavement is part of the “Urban Hydraulic Park,” which also includes an extensive green roof, a bioretention system, and a sedimentation tank connected with a treatment unit. The permeable pavement has an area of 154 m², an average slope of 2%, and a total depth of the profile of 0.98 m. Figure 3.1 shows a schematic of the permeable pavement, consisting of 5 layers.

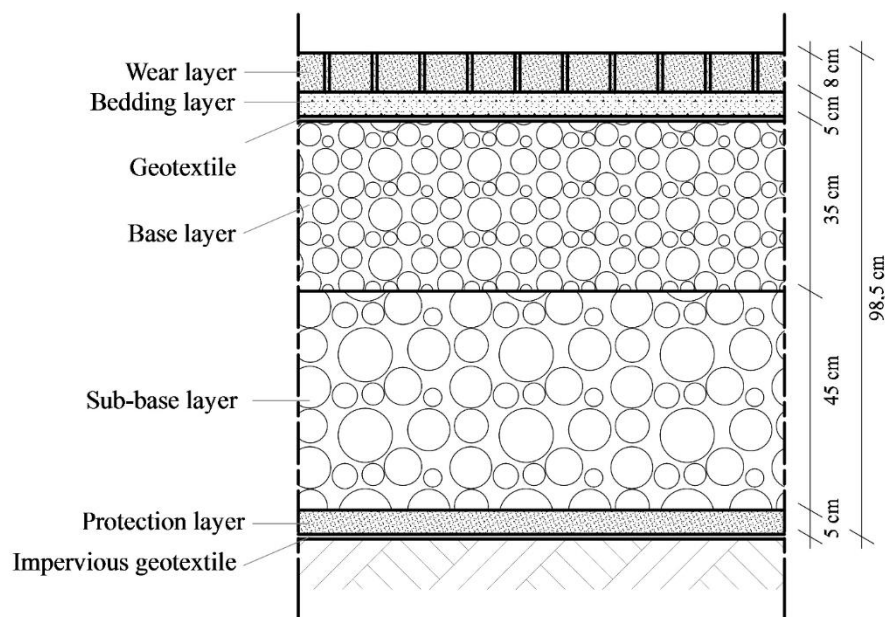


Figure 3.1 A schematic of the permeable pavement.

The surface wear layer consists of porous concrete blocks characterized by high permeability. Base, sub-base and bedding layers were constructed by following the suggestions of the Interlocking Concrete Pavement Institute (ICPI), which recommends certain ASTM

stone gradations. The ASTM numbers and corresponding gradations can be found in ASTM D 448, *Standard Classification for Sizes of Aggregate for Road and Bridge Construction*. The ASTM N°57, used for the base layer, is characterized by a porosity of about 30-35%. The ASTM N°2 is used in the sub-base layer for its stability and a high volumetric porosity of about 40%. The ASTM N°8 is used for the bedding layer and the protection layer and has a porosity of about 20% of volume. The bedding layer is composed of a mixture of sand, glass sand, and zeolite to improve the pollutant removal efficiency of the permeable pavement for typical contaminants of stormwater runoff. A high permeability geotextile with a fiber area weight of 60 g/m² is placed at the interface between the bedding layer and the base layer to prevent sand from migrating into the bottom layers. An impervious membrane is placed at the bottom of the profile to prevent water from percolating into deeper horizons. The protection layer which is composed of coarse sand is placed between the sub-base layer and the impervious membrane. The baseflow is collected in a horizontal drain, which consists of a perforated PVC pipe, and is conducted to a manhole for quantity and quality measurements.

A weather station located directly at the site measures precipitation, wind velocity and direction, air humidity, air temperature, atmospheric pressure, and global solar radiation. Rain data are measured by a tipping bucket rain gauge with a resolution of 0.254 mm and an acquisition frequency of one minute. Climatic data are acquired with a frequency of five minutes. Data are processed and stored in the SQL database.

Two flow meters, composed of a PVC pipe with a sharp-crested weir and a pressure transducer, measure baseflow and runoff from the permeable pavement. The pressure transducer (Ge Druck PTX1830) measures the water level inside the PVC pipe and has a range of measurement of 75 cm with an accuracy of 0.1 % of the full scale. The pressure transducers were calibrated in the laboratory by using a hydrostatic water column, linking the electric current intensity with the water level inside the column. The exponential head-discharge equations for the two PVC flow meters were obtained by fitting the experimental data with a coefficient of determination $R^2=0.999$ for both devices. Runoff and baseflow data were

acquired with a time resolution of 1 minute and stored in the SQL database. No measurements of pressure heads or volumetric water contents inside the pavement were taken.

Two month-long data sets were selected for further analysis (Fig. 3.2). The first data set, which started on 2014-01-15 and ended on 2014-02-15, was used for parameter optimization and sensitivity analysis. Total precipitation and total potential evapotranspiration for the first data set were 274 mm and 43 mm, respectively. The second data set, which started on 2014-03-01 and ended on 2014-03-31, was used for model validation. Total precipitation and total potential evapotranspiration for the second data set were 175 mm and 81 mm, respectively. The second data set was selected so that it had significantly different meteorological data than during the first period. The optimization set is characterized by multiple rain events with few dry periods. The validation set has fewer rain events, which are concentrated at the beginning and end of the time period and separated by a relatively long dry period between. Surface runoff was not observed during these time periods.

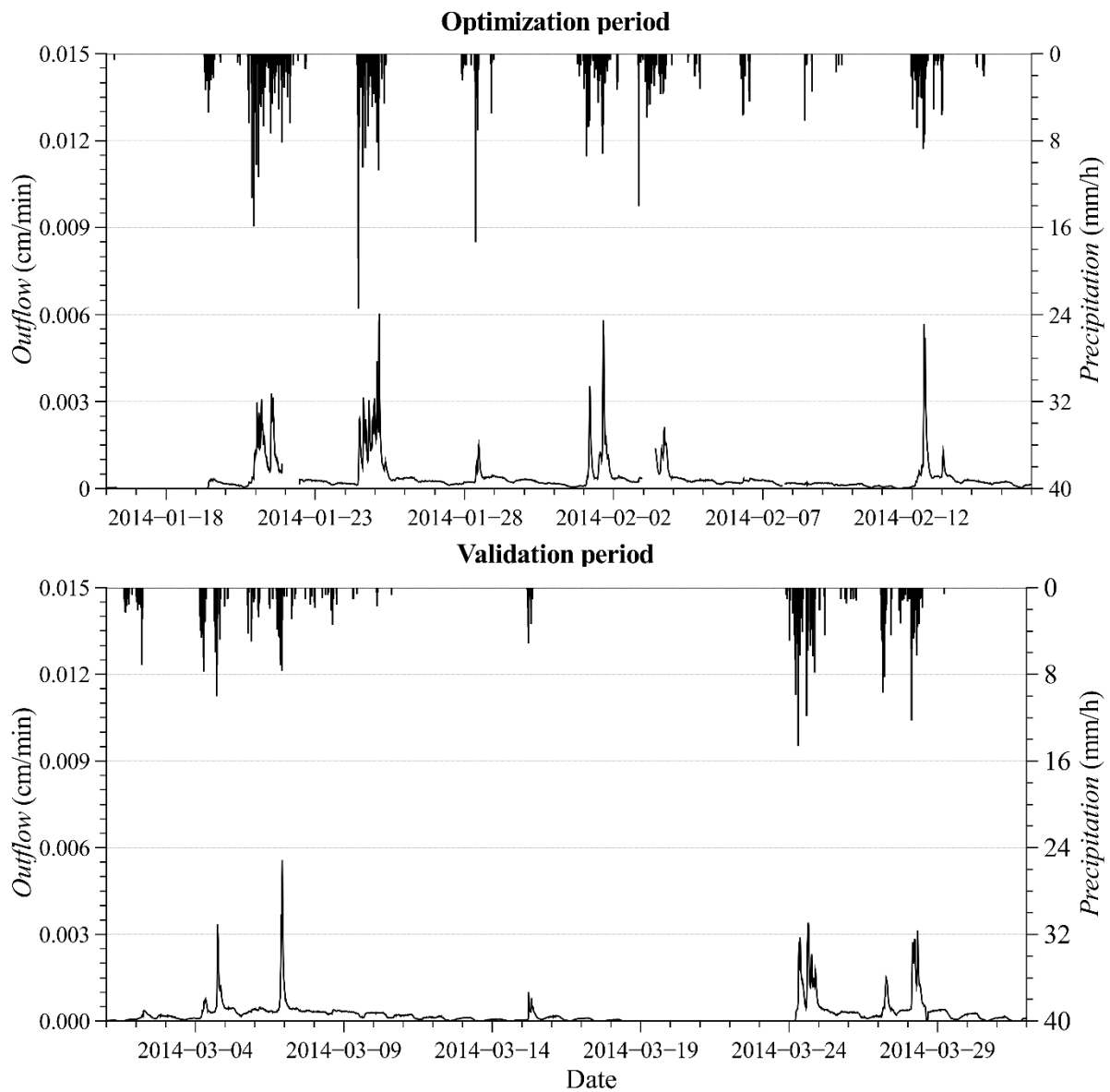


Figure 3.2 Precipitation and subsurface flow during the optimization (top) and validation (bottom) time periods.

Potential evaporation was calculated using the Penman-Monteith equation (Allen et al., 1998). The permeable pavement was installed in 2013 and has been constantly exposed to atmospheric conditions and traffic since then that has altered the surface roughness and color.

For these reasons, an albedo of 0.25 was used as suggested by Levinson and Akbari (2002) for weathered gray cement.

3.2.2 Theory

Water flow simulations were conducted using the HYDRUS-1D software (Šimůnek et al., 2008). HYDRUS-1D is a one-dimensional finite element model for simulating the movement of water, heat, and multiple solutes in variably-saturated porous media. HYDRUS-1D implements multiple uniform (single-porosity) and nonequilibrium (dual-porosity and dual-permeability) water flow models (Šimůnek and van Genuchten, 2008). In this study, two different conceptual models were used to represent flow in the permeable pavement (Table 3.1).

Table 3.1 Conceptual models representing water flow in the permeable pavement.

| Soil Layer | Scenario I | Scenario II |
|-------------------|-------------------|---------------------|
| Wear | Single Porosity | Single Porosity |
| Bedding | Single Porosity | Single Porosity |
| Base | Single Porosity | Dual Porosity – MIM |
| Sub-base | Single Porosity | Dual Porosity – MIM |
| Protection | Single Porosity | Single Porosity |

Scenario I assumed that water flow in all five soil layers of the permeable pavement can be described using the classical single-porosity approach (SPM). Unsaturated water flow is then described using the one-dimensional Richards equation:

$$\frac{\partial \theta}{\partial z} = \frac{\partial}{\partial z} \left[K(h) \left(\frac{\partial h}{\partial z} + 1 \right) \right] \quad (9)$$

where θ is the volumetric water content [-], h is the soil water pressure head [L], $K(h)$ is the unsaturated hydraulic conductivity [LT^{-1}], t is time [T], and z is the soil depth [L]. The soil

hydraulic properties are described by the van Genuchten – Mualem relation (van Genuchten, 1980):

$$\Theta = \begin{cases} \frac{1}{(1 + (\alpha|h|)^n)^m} & \text{if } h \leq 0 \\ 1 & \text{if } h > 0 \end{cases} \quad (10)$$

$$\Theta = \frac{\theta - \theta_r}{\theta_s - \theta_r}$$

$$K = \begin{cases} K_s \Theta^L \left[\left(1 - \left(1 - \Theta^{\frac{1}{m}} \right) \right)^m \right]^2 & \text{if } h < 0 \\ K_s & \text{if } h > 0 \end{cases} \quad (11)$$

$$m = 1 - \frac{1}{n}$$

where θ_r [-] is the residual water content, θ_s [-] is the saturated water content, K_s [LT⁻¹] is the saturated hydraulic conductivity, n is a pore-size distribution index [-], α is a parameter related to the inverse of the air-entry pressure [L⁻¹], L indicates the tortuosity and is usually assumed to be 0.5 for many soils, and Θ is the effective saturation [-]. In order to simplify the model (to lower the number of unknown parameters), the residual water content of all layers was fixed. In particular, the residual water content for the wear and bedding layers was assumed to be 0.045 and 0.03, respectively, while the residual water content for both the base and sub-base layers was assumed to be 0.0, considering that they were composed of crushed stones. Furthermore, considering that the bedding layer and the protection layer had the same stone gradation, ASTM N°8, the same set of parameters was used for both. Despite of all these considerations, this scenario still involves 16 parameters (θ_s , α , n , and K_s for 4 soil layers).

Scenario II assumes a single-porosity model for the wear layer, the bedding layer, and the protection layer, and a dual-porosity model for the base and sub-base layers. This configuration was selected in order to consider the occurrence of preferential flow in the coarse layers of the pavement.

The base and sub-base layers are composed of crushed stones, with particle size diameters ranging from 2.5 to 37 mm in the base layer and from 20 to 75 mm in the sub-base layer. Crushed stones were washed before installation in order to remove fine particles. This narrow gradation provides a high volume of voids and increases the water storage and infiltration capacities of these two layers. From a physical point of view, the structure of the base and sub-base materials closely resembles fractured aquifers (Barenblatt et al., 1960). Fractured aquifers are represented by a blocky matrix system intercepted by fractures. Open and well-connected fractures represent high permeability pathways that are many orders of magnitude more permeable than the porous rock matrix. At the same time, one of the characteristics of a fractured aquifer is that the fractures occupy a much smaller volume than the pores of the rock matrix. Traditionally, fractured porous media are thus represented by two separate flow domains: the high permeability (mobile) domain, the network of connected fractures characterized by advective flow, and the low permeability (immobile) domain, dominated by diffusion. The rock matrix also provides storage capacity because of its significantly larger volume than the fracture system. Typical breakthrough curves for a fractured aquifer are characterized by early breakthrough and long tailing (Geiger et al., 2010). This is due to the fact that the matrix has a delayed response to pressure head changes that occur in the surrounding fractures. The resulting pressure difference induces matrix-fracture interflow. This flow takes place after initial fracture flow and before the matrix and fracture pressures equilibrate (Bai et al., 1994). Several studies have demonstrated the long tailing from permeable pavements in discharge hydrographs (e.g., Brattebo and Booth, 2003; Fassman and Blackburn, 2010) and attributed this effect to the storage and flow through the base and sub-base layers.

The classical approach to model water flow in fractured porous media is the so-called “dual-porosity” or “mobile-immobile water” (MIM) approach (Barenblatt et al., 1960; van Genuchten and Wierenga, 1976; Warren and Root, 1963). This approach assumes that flow occurs only in the mobile fracture domain, for which an effective permeability must be known,

while water in the matrix domain is immobile. Both domains are connected by a simple first-order transfer function, which accounts for the exchange of fluid across the boundary of the two domains.

In the dual-porosity approach, the liquid phase is divided into two domains:

$$\theta = \theta_f + \theta_m \quad (12)$$

where subscript f refers to the (mobile) fracture system, and subscript m refers to the immobile matrix domain. The dual-porosity water flow formulation is based on a modified Richards equation for flow in fractures and a mass balance equation for moisture dynamics in the matrix:

$$\frac{\partial \theta_f}{\partial z} = \frac{\partial}{\partial z} \left[K(h) \left(\frac{\partial h}{\partial z} + 1 \right) \right] - \Gamma_w \quad (13)$$

$$\frac{\partial \theta_m}{\partial t} = \Gamma_w \quad (14)$$

where Γ_w is the mass transfer between two domains, which is assumed to be proportional to the difference in effective saturations of the two regions (Šimůnek and van Genuchten, 2008; Simunek et al., 2003):

$$\Gamma_w = \omega \cdot (S_e^m - S_e^{im}) \quad (15)$$

where ω is a first-order coefficient [T^{-1}]. Compared to assuming a pressure head based driving force for the mass transfer, the dual-porosity model based on (7) requires significantly less parameters since one does not need to know the retention function (and corresponding parameters) for the matrix region explicitly, but only its residual and saturated water contents (Simunek et al., 2003). The residual water content for the mobile domain of both the base and sub-base layers is assumed to be 0.0 (Simunek et al., 2003). The tortuosity factor, L , is again assumed to be 0.5 for all layers. Scenario II thus includes 20 parameters (additionally also ω and θ_s of the immobile domain for the base and subbase layers).

3.2.2.1 Numerical Domain and Boundary Conditions

The numerical domain representing the stratigraphy of the permeable pavement was divided in 5 layers. The bedding layer and the protection layer had the same properties since they were constructed using the same ASTM N°8 stone gradation. A relatively fine, finite element mesh with a constant element size of 0.5 cm was used in order to minimize mass balance errors and avoid non-convergent runs during sensitivity analysis and parameter optimization. An atmospheric boundary condition was applied at the pavement surface using (a) precipitation and potential evaporation fluxes, (b) a prescribed zero pressure head (saturation) during ponding, and (c) equilibrium between the pavement surface water content and atmospheric water vapor when atmospheric evaporative demand could not be met by the wear layer. A seepage face boundary condition was specified at the bottom of the protection layer. A seepage face boundary acts as a zero pressure head boundary when the bottom boundary node is saturated and as a no-flux boundary when it is unsaturated. The initial conditions were specified in terms of the soil water pressure head and were set to linearly increase with depth, from -90 cm at the top of the flow domain ($z = 0$) to -0.5 cm at the bottom ($z = -98$). The surface layers are assumed to be drier than the bottom layers since they are directly exposed to evaporation.

3.2.2.2 Objective Function

The Nash-Sutcliffe Efficiency (NSE) index (J E Nash and Sutcliffe, 1970) is used for evaluating the agreement between hydrographs:

$$NSE = 1 - \left[\frac{\sum_{i=1}^T (Q_i^{obs} - Q_i^{mod})^2}{\sum_{i=1}^T (Q_i^{obs} - Q_{mean}^{obs})^2} \right] \quad (16)$$

where Q_i^{obs} is the i th measured value, Q_i^{mod} is the i th simulated value, and Q_{mean}^{obs} is the mean value of observed data. The NSE coefficient ranges between $-\infty$ and 1.0, is equal to 1 in case of a perfect agreement, and, generally, values between 0.0 and 1.0 are considered acceptable (Moriassi et al., 2007). The NSE has been used because it is often reported to be the best measure for evaluating the overall fit of a hydrograph (Sevat et al., 1991).

3.2.2.3 Global Sensitivity Analysis

Most existing environmental models include a high number of parameters. This aspect creates a major problem in their application, as the parameter estimation becomes a high-dimensional and mostly nonlinear problem. To solve this problem, several optimization algorithms were developed (Beven and Binley, 1992; Duan et al., 1992; Poli et al., 2007; Vrugt et al., 2003). Moreover, environmental optimization studies are often affected by the equifinality problem (Beven, 2006) when multiple sets of parameters can produce similar results. This problem is exacerbated when the number of parameters is significant and only limited information about their interactions and their effects on the output is available. However, it is not always necessary to include all model parameters in the optimization process because some of them could be measured or estimated, and some may have negligible effects on the output of the model for a particular application. A sensitivity analysis (SA) can identify the most influential parameters and their interactions and how these parameters affect the output (Saltelli et al., 2005).

The principal steps of a SA are: Factors Prioritization (FP), Factors Fixing (FF), Variance Cutting (VC), and Factors Mapping (FM) (Saltelli and Tarantola, 2004). The aim of FP is to identify factors that one should measure in order to obtain the greatest reduction in the uncertainty of the output. Conversely, FF identifies factors that are non-influential. By applying these two settings, the modeler is able to reduce the dimension of the optimization problem and have a complete appreciation of the parameters' influences and interactions.

Most SAs performed in the literature of environmental sciences are the so-called 'one-at-a-time' (OAT) sensitivity analyses, performed by changing the value of parameters one-at-a-time while keeping the others constant (Chevion and Coquet, 2009; Houska et al., 2013; Rezaei et al., 2015). However, when the model includes interactions between parameters, results of the OAT analysis are inaccurate because parameter interactions can be identified only by changing multiple parameters simultaneously. For this reason, when the property of a model is a priori unknown, a Global Sensitivity Analysis (GSA) is always preferred (Saltelli and Annoni, 2010). Practitioners call this analysis a model-free setting.

One of the most widespread algorithms for the GSA is the variance-based Sobol' method (Sobol', 2001). Variance-based methods aim to quantify the amount of variance that each parameter contributes to the unconditional variance of the model output. For the Sobol' method, these amounts are represented by Sobol's sensitivity indices (SI's). These indices give quantitative information about the variance associated with a single parameter or related to interactions of multiple parameters. For a more complete explanation about the Sobol' method, please refer to Sobol' (2001).

Sobol's sensitivity indices are expressed as follows:

$$\text{First Order } S_i = \frac{V_i}{V} \quad (17)$$

$$\text{Second Order } S_{ij} = \frac{V_{ij}}{V} \quad (18)$$

$$\text{Total } S_T = S_i + \sum_{j \neq i} S_{ij} + \dots \quad (19)$$

where V_i is the variance associated with the i th parameter and V is the total variance. The first-order index, S_i , is denoted in the literature as the "main effect". This index can be described as the fraction of the model output variance that would disappear when parameter X_i is fixed. When the model is additive, i.e., when it does not include interactions between input factors,

then the first-order index is sufficient for decomposing the model's variance. For additive models, the following relation is valid:

$$\sum_i S_i = 1 \quad (20)$$

Even when the model includes interactions between parameters, the first-order index remains the measure to use for FP (Saltelli and Tarantola, 2004). On the other hand, the total effect index, S_T , gives information about a non-additive part of the model. A significant difference between S_T and S_i indicates an important role of an interaction for the parameter considered. Essentially, the total effect index, S_{Ti} , gives a fraction of the total variance that would be left when all factors but X_i were fixed. $S_{Ti} = 0$ is a condition necessary and sufficient for X_i to be non-influential. Therefore, X_i can be fixed at any value within its range of uncertainty without affecting the output unconditional variance. The total effect is the measure to use for FF.

Considering that environmental models are generally highly nonlinear, it is almost impossible to calculate the variances using analytical integrals. Hence, Monte Carlo integrals are often applied, which are based on sampling the parameter space in q samples. Obviously, the accuracy in the estimation of integrals becomes more accurate as the number of samples increases, which also increases the computational cost of the SA. For an accurate description of the calculation of Sobol's indices please refer to Saltelli (2010).

Basically, the calculation of Sobol's indices requires $q \cdot (2p+1)$ model evaluations, where p is the number of input factors. However, Saltelli (2002) introduced a method that requires only $q \cdot (p+2)$ model evaluations. To sample the parameters' space we used Sobol's quasi-random sampling technique (Sobol', 2001).

One of the most important aspects of the GSA is the choice of the number of samples, q . An increase in the number of samples will increase the accuracy of Sobol's indices. However, a high q implies a higher number of model evaluations. The number of samples is case-sensitive; it depends on the structure of the model and on the type of simulations performed. A convergence analysis of Sobol's indices is the recommended procedure for estimating q .

However, this approach is time consuming because it needs to repeat the GSA several times by increasing the number of samples until the variability of indices between two consecutive analyses is below a threshold value for all parameters.

In a recent study, Nossent et al. (2011) gave a comprehensive description of the influence of q on the accuracy of a GSA for an environmental model that included 26 parameters. Nossent et al. (2011) reported that for most parameters, less than 5000 samples were sufficient to reach a stable solution. An extensive review of the GSA in hydrological models is reported in Song et al. (2015). Here, we report the number of model runs for each GSA performed, together with the type of GSA, the number of parameters of the model, and the objective function used. For the GSA based on Sobol's method, the number of model runs rarely exceeds 100,000. Due to considerations discussed above, a value of $q=5000$ was chosen in our study. Table 3.2 summarizes the characteristics of the GSA for the two scenarios considered.

Table 3.2 Number of parameters and HYDRUS-1D runs for both scenarios.

| Scenario | Number of parameters | Model runs |
|-----------------|-----------------------------|-------------------|
| I | 16 | 90000 |
| II | 20 | 110000 |

In order to assess the accuracy of estimations of the sensitivity indices, the bootstrap confidence intervals (BCIs) (Efron and Tibshirani, 1986) were estimated. The basic idea of the bootstrapping is that, in absence of any other information about the distribution, the sample contains all the available information about the underlying distribution. In our particular case, we were interested in computing the uncertainty of estimated sensitivity indices. However, since their distribution is unknown it is not possible to compute the confidence intervals analytically. The rationale of the bootstrap method is to replace the unknown distribution with its empirical distribution and to compute the sensitivity indices using a Monte Carlo simulation approach where samples are generated by resampling the original sample used for the

sensitivity analysis. In our case, the q samples used for the model evaluation were sampled 1000 times with replacement, whereby Sobol's indices were calculated for each resampling. In this way, 95% confidence intervals are constructed by using the percentile method and the moment method (Archer et al., 1997).

The sensitivity analysis was conducted using the programming language Python and in particular, the Sensitivity Analysis Library (SALib) (Usher et al., 2015). An elaborated script overwrites the input file containing the parameters for different materials at each iteration. The script then executes HYDRUS-1D, which usually runs less than one second. If the HYDRUS-1D run is not finished after 15 seconds, it is considered non-convergent; the script then terminates the process and attributes a large negative value to the objective function. The same negative value is attributed when the length of the modeled hydrograph is shorter than one month, which indicates that the run was unsuccessful. Values of the objective function are stored in a one-dimensional array for the subsequent computation of sensitivity indices. Table 3.3 reports the initial range of all evaluated parameters in the two scenarios. The initial conditions were not included in the GSA because their effects on the hydrograph for a month-long simulation are assumed to be limited to only the first few days.

Table 3.3 Ranges of parameters used in the GSA for both scenarios.

| | Scenario I | Scenario II |
|-------------------|----------------------|--------------------|
| Parameter | Initial range | |
| θ_{s1} [-] | 0.2-0.5 | 0.2-0.5 |
| a_1 [1/cm] | 0.001-0.3 | 0.001-0.3 |
| n_1 [-] | 1.1-4.5 | 1.1-4.5 |
| K_{s1} [cm/min] | 1.0-20.0 | 1.0-20.0 |
| θ_{s2} [-] | 0.2-0.5 | 0.2-0.5 |
| a_2 [1/cm] | 0.001-0.3 | 0.001-0.3 |

| | | |
|----------------------|-----------|---------------|
| n_2 [-] | 1.1-4.5 | 1.1-4.5 |
| K_{s2} [cm/min] | 1.0-20.0 | 1.0-20.0 |
| θ_{s3} [-] | 0.01-0.40 | 0.001-0.1 |
| a_3 [1/cm] | 0.001-0.3 | 0.001-0.3 |
| n_3 [-] | 1.1-4.5 | 1.1-4.5 |
| K_{s3} [cm/min] | 1.0-100.0 | 1.0-100.0 |
| $\theta_{s,im3}$ [-] | - | 0.15-0.4 |
| ω_3 [1/min] | - | 0.00001-0.009 |
| θ_{s4} [-] | 0.01-0.4 | 0.001-0.1 |
| a_4 [1/cm] | 0.001-0.3 | 0.001-0.3 |
| n_4 [-] | 1.1-4.5 | 1.1-4.5 |
| K_{s4} [cm/min] | 1.0-100.0 | 1.0-100.0 |
| $\theta_{s,im4}$ [-] | - | 0.15-0.4 |
| ω_4 [1/min] | - | 0.00001-0.009 |

3.2.2.4 Monte Carlo Filtering

In the context of an optimization framework, results of the GSA can be used to extract useful information about the problem structure. The GSA preliminarily identifies the subset of input factors that drive most of the variation in the model output; to establish their optimal values, these sensitive parameters can be further investigated by using a Monte Carlo filtering approach. Filtering techniques are used to explore the parameter space pertaining to the single or multiple optima. This is particularly relevant when dealing with mechanistic models that almost always contain ill-defined parameters and are thus referred to as over-parameterized models (Draper and Smith, 1981).

The Monte Carlo filtering is often coupled with the regionalized sensitivity analysis (RSA) (Hornberger and Spear, 1981). The RSA generally requires two tasks: (a) a qualitative description of the system behavior, and (b) a binary classification of the model output that

divides solutions into two behavioral and non-behavioral groups. However, the main drawback of the RSA is that no higher-order analysis is performed and thus interactions between parameters are not investigated. In the GSA, a complete description of main effects and interactions is given. The GSA has been combined effectively with the GLUE analysis (Beven and Binley, 1992) in the context of the parameter optimization (Ratto et al., 2001). In Ratto et al. (2001), the sample generated for the GLUE analysis is also used for the computation of variance-based sensitivity indices.

In this study, the GSA is coupled with a basic Monte Carlo filtering. The aim of this step is to identify *behavioral* regions in the parameter space and to reduce the uncertainty in the following parameter estimation step by using the same sample and runs of the GSA. For each parameter set used in the GSA, a value of the objective function is calculated. Potential solutions are divided into two groups: *behavioral*, solutions with $NSE > 0.0$, and *non-behavioral*, solutions with $NSE \leq 0.0$. Two different types of analysis were performed on the filtered sample: a) Kernel density estimation and b) correlation analysis.

3.2.2.5 Kernel Density Estimation (KDE)

The KDE plots have been used to identify regions with a high density of *behavioral* solutions. The KDE is a non-parametric estimator of the probability density function (PDF) of a random variable (Silverman, 1981). A kernel is a special type of PDF with an added property that it must be even. The KDE bi-variate plots have been used because they give a smooth qualitative representation of PDFs in a bi-dimensional space. The uni-variate KDE has also been computed for each parameter. The KDE plots have been calculated using a Gaussian kernel and the Scott procedure for the determination of a bandwidth (Scott, 1992).

3.2.2.6 Correlation Analysis

The correlation analysis helps to identify particular interaction structures between parameters. Detecting high values of correlation coefficients suggests a way to reduce the input factor space. In particular, when the coefficient is positive, the couple of parameters acts in the model as a quotient/difference, and when it is negative, the parameters act as a product/sum.

3.2.2.7 Particle Swarm Optimization

Inverse modeling is a procedure to estimate unknown parameters of the model from experimental data. One of the major reasons to apply inverse modeling is to estimate parameters that cannot be directly measured for various reasons. Numerous applications of inverse modeling for the estimation of soil hydraulic properties exist in the literature (Abbaspour et al., 2004; Hopmans et al., 2002; Vrugt et al., 2008, 2004). The gradient methods (Marquardt, 1963) have been used most widely among hydrologists and soil scientists. However, these methods are sensitive to the initial values of optimized parameters, and the algorithm often remains trapped in local minima, especially when the response surface exhibits a multimodal behavior. These considerations inspired researchers to develop and use global optimization techniques such as the annealing-simplex method (Pan and Wu, 1998), genetic algorithms (Ines and Droogers, 2002), shuffled complex methods (Vrugt et al., 2003), and ant-colony optimization (Abbaspour et al., 2001), among many others.

In this paper, a global search method based on Particle Swarm Optimization (PSO) (Kennedy and Eberhart, 1995) is used. PSO has been used in multiple studies involving inverse modeling with complex environmental models (Gill et al., 2006; Jiang et al., 2010; Zambrano-

Bigiarini and Rojas, 2013). However, so far it has not been used for the determination of unsaturated hydraulic properties. PSO is a relatively new algorithm for evolutionary computation methodology, but its performance has proven to be comparable to various other, more established methodologies (Kennedy and Spears, 1998; Shi and Eberhart, 1999). One of the main advantages of PSO is the easiness of its implementation (Liang et al., 2006). PSO is characterized by an algorithm based on a social-psychological metaphor involving individuals that interact with each other in a social world. PSO was inspired by the behavior of schools of fish or flocks of birds as they seek food or other resources. In PSO, collections of “particles” explore the search space, looking for a global or near-global optimum. Particles in PSO keep track of their best positions thus far obtained in the search space and the best positions obtained by their neighboring particles. The global best position is what all particles tend to follow. A detailed description of the PSO algorithm is given in Shi and Eberhart (1998).

The most important parameters in the PSO are: c_1 , c_2 , and w . c_1 and c_2 are constant parameters known as the cognitive and social parameters, respectively, and w is the inertia-weight, which plays a key role in the optimization process by providing balance between exploration and exploitation. A large w facilitates a global search while a small one facilitates a local search. The w parameter is very similar to the “temperature” parameter in the simulated annealing algorithm. While several strategies have been used in the literature for the inertia weight, in this study, a constant value of w has been used (Shi and Eberhart, 1998).

In PSO, each particle is influenced by its σ nearest neighbors. The arrangement of neighbors that influence a particle is called the *topology* of the swarm. Different types of neighborhoods are reported in the literature (Akat and Gazi, 2008). In this study, the *all* topology is used, in which the neighborhood encompasses the entire swarm. The PSO parameters used in this study for both scenarios are reported in Table 3.4 and are as suggested by Pedersen (2010).

Table 3.4 Parameters used in the PSO optimization.

| N | c_1 | c_2 | w |
|-----------|--------|-------|--------|
| 69 | -0.267 | 3.395 | -0.444 |

A modified version of the PySwarm Python Library was used for the PSO analysis. Similar to the GSA, a Python script has been written for the optimization process. The script overwrites the input file of HYDRUS-1D containing the hydraulic parameters for the different layers, runs the executable module, and retrieves the value of the objective function. A large negative value of NSE is attributed to non-convergent runs, as defined above.

3.3 Results and Discussion

3.3.1 Sensitivity Analysis – Scenario I

As discussed above, the basic outcome of Sobol's SA are the first-order (S_1) and total (S_T) sensitivity indices. Table 3.5 presents these two indices and their relative bootstrap confidence intervals (BCI). In the left part of Table 3.5 (S_1), it can be seen that only two parameters exhibit a significant direct influence on the output's variance, the pore-size distribution index n_1 and the air-entry pressure parameter a_1 . The third most influential parameter, the saturated hydraulic conductivity K_{s1} , has the effect, which is only half of the second most influential parameter, a_1 . Ten parameters have a first-order index lower than 1%, which indicates that their main effect on the output variance is negligible. Table 3.5 also shows that the sum of all first-order indices is less than 1, which means that the model is non-additive. Only 56% of variance is attributable to the first-order effects, which indicates that interactions between parameters play a fundamental role.

Table 3.5 First-order (S_1) and total (S_T) effect indices (in decreasing order) with their bootstrap confidence intervals (BCI) for parameters of Scenario I.

| Parameter | S_1 | S_1 (BCI) | Parameter | S_T | S_T (BCI) |
|-------------------|--------|-------------|-------------------|-------|-------------|
| n_1 [-] | 0.298 | 0.054 | n_1 [-] | 0.745 | 0.042 |
| a_1 [1/cm] | 0.102 | 0.040 | a_1 [1/cm] | 0.508 | 0.032 |
| K_{s1} [cm/min] | 0.051 | 0.040 | K_{s1} [cm/min] | 0.421 | 0.032 |
| θ_{s3} [-] | 0.023 | 0.024 | θ_{s1} [-] | 0.247 | 0.025 |
| a_4 [1/cm] | 0.020 | 0.023 | n_4 [-] | 0.224 | 0.146 |
| a_2 [1/cm] | 0.017 | 0.022 | K_{s3} [cm/min] | 0.210 | 0.127 |
| n_3 [-] | 0.014 | 0.029 | n_3 [-] | 0.194 | 0.035 |
| K_{s4} [cm/min] | 0.009 | 0.025 | a_3 [1/cm] | 0.181 | 0.024 |
| n_4 [-] | 0.009 | 0.035 | a_2 [1/cm] | 0.176 | 0.024 |
| θ_{s1} [-] | 0.009 | 0.028 | n_2 [-] | 0.176 | 0.028 |
| n_2 [-] | 0.007 | 0.023 | a_4 [1/cm] | 0.170 | 0.033 |
| K_{s3} [cm/min] | 0.004 | 0.022 | θ_{s3} [-] | 0.167 | 0.031 |
| θ_{s4} [-] | 0.001 | 0.022 | θ_{s2} [-] | 0.151 | 0.030 |
| a_3 [1/cm] | -0.001 | 0.024 | K_{s2} [cm/min] | 0.138 | 0.023 |
| θ_{s2} [-] | -0.004 | 0.019 | K_{s4} [cm/min] | 0.138 | 0.038 |
| K_{s2} [cm/min] | -0.005 | 0.016 | θ_{s4} [-] | 0.136 | 0.022 |
| Sum | 0.563 | | | > 1.0 | |

The right part of Table 3.5 (S_T) shows that almost 75% of variance in simulated outflow is caused by n_1 , either by the variation of the parameter itself (30%) or by interactions with other parameters. Together with a_1 (51%) and K_{s1} (42%), it is the most influential parameter for simulated flow. It can be noted that the saturated hydraulic conductivity, K_{s1} , has a relatively low main effect but a relatively high total effect. That indicates that this parameter has a limited direct effect on the variance of the objective function, but it has an effect in interactions with other parameters.

The effect of the sub-base layer on the output is less significant, while the wear layer strongly conditions the output. That behavior is in agreement with results reported in the literature. Illgen et al. (2007), in his laboratory campaign, confirmed that the wear layer has the major influence on the infiltration capacity of the permeable pavement, while the base and sub-

base layers have a minor impact and act as a storage tank. The total index is always greater than zero, which implies that all parameters influence the output variance either directly or by their interactions, and thus no parameter can be fixed without affecting the uncertainty of the output.

Scatter plots for the plain Monte Carlo runs for the two most sensitive parameters, a_1 and n_1 , are displayed in Figure 3.3. The scatter plots show that there is no clear pattern of factors driving bad solutions. Particular trends in the solutions were further identified by the regression lines. They indicate that there is a trend for parameter a_1 , with admissible solutions in the left part of the plot. On the other hand, the distribution of values for parameter n_1 is flat, and thus no conclusions can be made about the position of a denser region of *behavioral* solutions in the high-dimensional space.

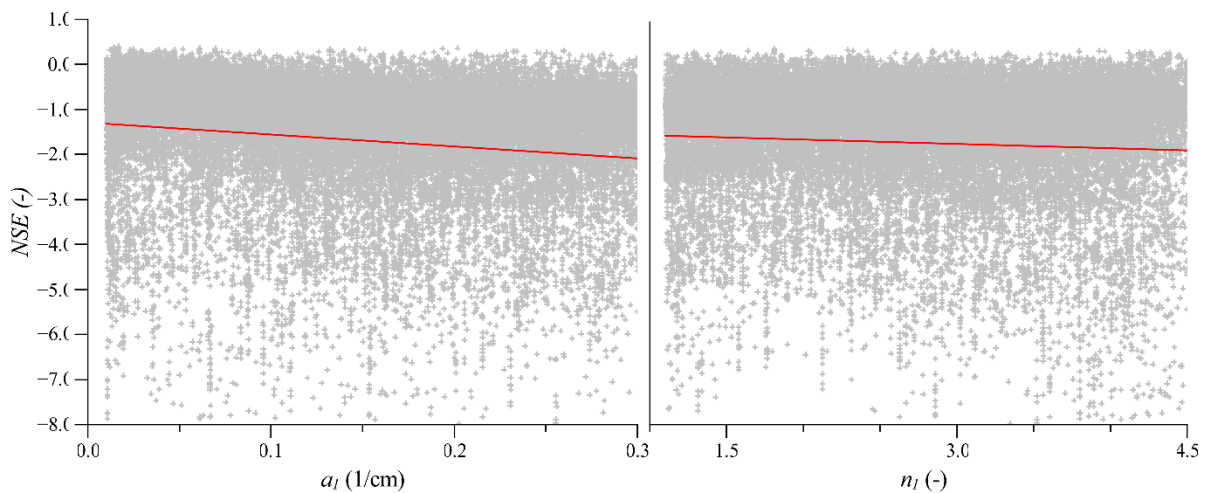


Figure 3.3 Scatter plots for pair relations a_1 -NSE (left) and n_1 -NSE (right) for Scenario I. The red line is a regression line.

3.3.2 Monte Carlo Filtering – Scenario I

A Monte Carlo Filtering procedure was applied to the runs of the GSA. The threshold value of $NSE = 0.0$ produced a filtered sample composed of 1,452 *behavioral* solutions. Figure 4 shows the univariate and bivariate KDE plots and the correlation plots for the wear layer.

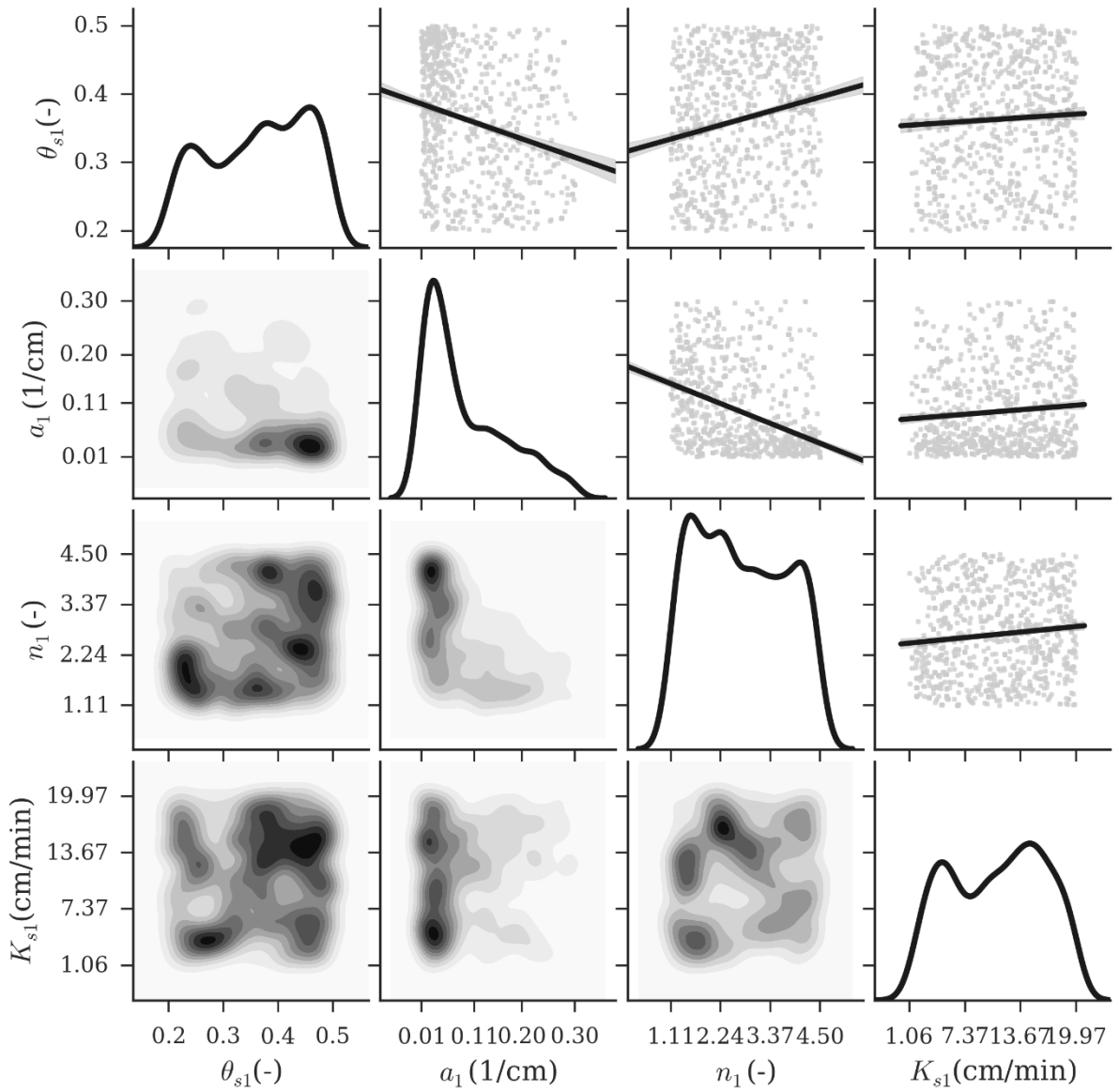


Figure 3.4 Bivariate KDE plots (below diagonal), univariate KDE plots (diagonal), and correlation plots (above diagonal) for Scenario I.

The maximum Pearson correlation coefficient (in absolute values) was 0.42 between parameters a_1 and n_1 . It is also evident from Figure 4 that a moderate negative correlation is present for parameters θ_{s1} - a_1 , and a positive correlation for parameters θ_{s1} - n_1 , while for the other parameters, the correlation is negligible. The univariate KDEs for parameters θ_{s1} , n_1 , and K_{s1} indicate a platykurtic distribution of *behavioral* solutions characterized by multimodality. Parameter a_1 exhibits a leptokurtic distribution, for which a denser region of good solutions is clearly identifiable in the range of 0.001-0.1.

This behavior is more clear in the bivariate KDE plots. The bivariate KDE for a_1 - n_1 highlights the presence of a denser region for values of n_1 in the range 2.5-4.5, a behavior that was not evident from the univariate KDE. The comparison between univariate and bivariate plots reveals that the latter gives a much more comprehensive description of the response surface. This aspect is exacerbated when the model is governed by interactions between parameters, which is clearly highlighted by Sobol's indices. In such a case, the high-dimensional inspection of the parameter space provides significant information.

The saturated hydraulic conductivity, K_{s1} , for which the univariate KDE indicates a multimodal behavior, exhibits a denser region in the range of 10.0-20.0; this region is clearly identifiable in the bivariate plot of K_1 - n_1 .

3.3.3 Sensitivity Analysis – Scenario II

Results of the GSA for Scenario II are reported in Table 3.6. Also for Scenario II, parameters a_1 and n_1 exhibit the highest main effects on the output's variance (about 35%). For Scenario II, the differences are even more evident than for Scenario I. Parameters n_1 and a_1 have a first-order index of 30% and 5%, respectively, while all remaining parameters remain well under 5%. Nine parameters have a first-order index lower than 1%. The main effects represent 53% of the output variance, which clearly indicates both that the model output is again (similarly as for Scenario I) partially driven by interactions between parameters, and that the model is non-additive.

Table 3.6 First-order (S_1) and total (S_T) effect indices (in decreasing order) with their bootstrap confidence intervals (BCI) for parameter of Scenario II.

| Parameter | S_1 | S_1 (BCI) | Parameter | S_T | S_T (BCI) |
|----------------------|--------|-------------|----------------------|-------|-------------|
| n_1 [-] | 0.302 | 0.026 | n_1 [-] | 0.640 | 0.023 |
| a_1 [1/cm] | 0.054 | 0.029 | a_1 [1/cm] | 0.387 | 0.027 |
| θ_{s3} [-] | 0.030 | 0.045 | n_3 [-] | 0.383 | 0.020 |
| n_3 [-] | 0.026 | 0.024 | θ_{s3} [-] | 0.294 | 0.027 |
| K_{s3} [cm/min] | 0.018 | 0.022 | a_3 [1/cm] | 0.291 | 0.022 |
| a_4 [1/cm] | 0.018 | 0.020 | θ_{s1} [-] | 0.271 | 0.019 |
| θ_{s2} [-] | 0.017 | 0.018 | a_4 [1/cm] | 0.269 | 0.019 |
| θ_{s4} [-] | 0.014 | 0.022 | K_{s1} [cm/min] | 0.259 | 0.018 |
| a_3 [1/cm] | 0.013 | 0.025 | n_4 [-] | 0.256 | 0.013 |
| K_{s2} [cm/min] | 0.012 | 0.026 | a_2 [1/cm] | 0.229 | 0.017 |
| K_{s4} [cm/min] | 0.011 | 0.031 | K_{s3} [cm/min] | 0.222 | 0.017 |
| θ_{s1} [-] | 0.007 | 0.023 | n_2 [-] | 0.217 | 0.022 |
| $\theta_{s,im3}$ [-] | 0.006 | 0.017 | θ_{s4} [-] | 0.201 | 0.017 |
| a_2 [1/cm] | 0.005 | 0.016 | K_{s2} [cm/min] | 0.195 | 0.023 |
| K_{s1} [cm/min] | 0.001 | 0.022 | K_{s4} [cm/min] | 0.186 | 0.021 |
| ω_4 [1/min] | -0.001 | 0.027 | θ_{s2} [-] | 0.185 | 0.018 |
| n_2 [-] | -0.001 | 0.026 | $\theta_{s,im3}$ [-] | 0.149 | 0.016 |
| ω_3 [1/min] | -0.003 | 0.021 | ω_3 [1/min] | 0.143 | 0.016 |
| $\theta_{s,im4}$ [-] | -0.004 | 0.020 | $\theta_{s,im4}$ [-] | 0.138 | 0.013 |
| n_4 [-] | -0.006 | 0.017 | ω_4 [1/min] | 0.125 | 0.020 |
| Sum | 0.534 | | | > 1.0 | |

The right part of Table 3.6 (S_T) shows that the output variance is largely influenced by n_1 , either directly (30%) or by interactions with other parameters (64%). Similar to Scenario I, parameters a_1 and n_1 are the most influential parameters, and the model's output is mainly driven by the wear layer. Four of the first eight most influential parameters are related to the wear layer. The main difference between Scenarios I and II is the influence of the base and sub-base layers on the model's output. This is evident from Figure 5, in which the average S_T for each layer is reported for both scenarios. For both scenarios, modeling results are most sensitive to the wear layer, which strongly influences the output's variance. However in Scenario II, the influence of the wear layer is partially reduced and redistributed to other layers. It is evident that the adoption of the dual-porosity model for the unsaturated hydraulic properties significantly affects the influence of the base and sub-base layers on the model's output. The dynamics of sensitivity indices between the two scenarios suggest that the physical description of unsaturated flow in the sub-base layer is an important element in numerical simulations.

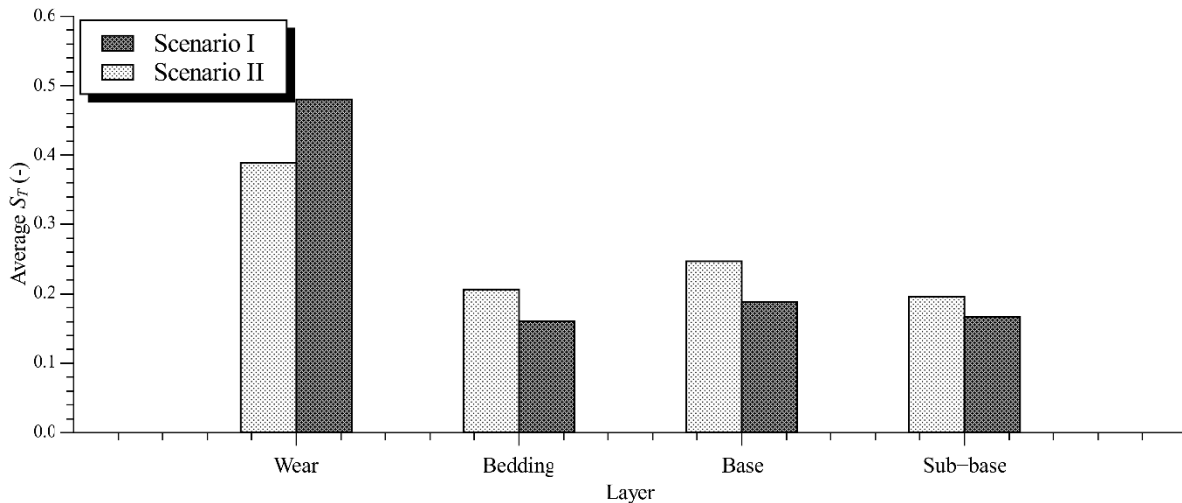


Figure 3.5 The average total index, S_T , for different layers for both scenarios.

Similar to scenario I, all parameters influence the model's output, either by the variation of the parameters themselves or by their mutual interactions. The condition for FF is never achieved for all parameters.

Scatter plots for the plain Monte Carlo runs for the two most sensitive parameters, a_1 and n_1 , are displayed in Figure 6. It can be seen that there is again no clear pattern of factors driving bad solutions. The regression lines indicate that there is a slight trend, which is higher for parameter a_1 , to have admissible solutions in the left part of the plot. The optimum appears flat, however.

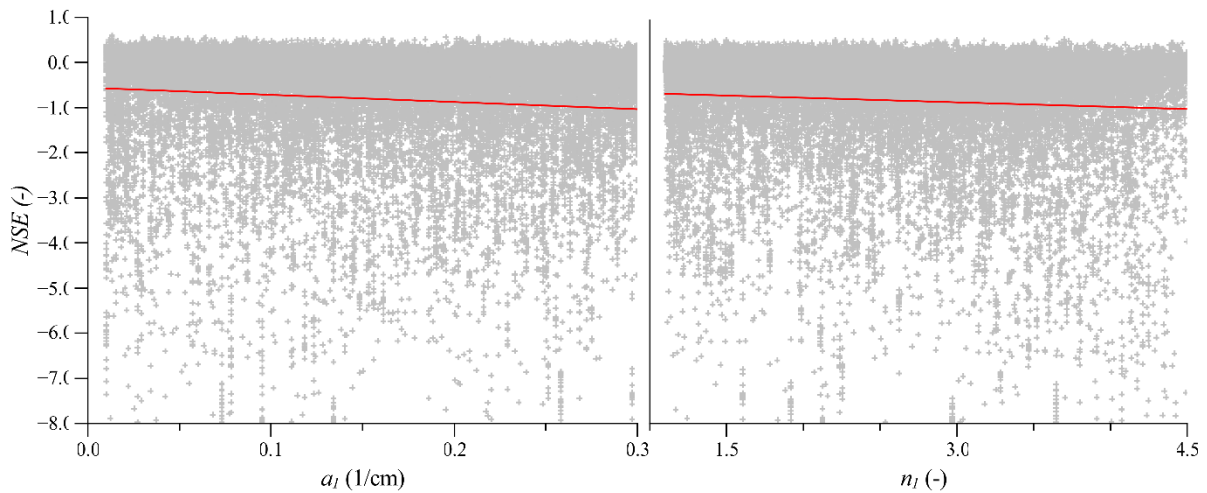


Figure 3.6 Scatter plots for pair relations a_1 -NSE (left) and n_1 -NSE (right) for Scenario II. The red line is a regression line.

3.3.4 Monte Carlo Filtering – Scenario II

A Monte Carlo Filtering procedure was again applied to the runs of the GSA. The filtered sample now consisted of 28,107 *behavioral* solutions. The filtered sample of *behavioral* solutions for Scenario II was considerably larger than for Scenario I. This indicates that the implementation of the dual-porosity model leads to higher values of the objective function.

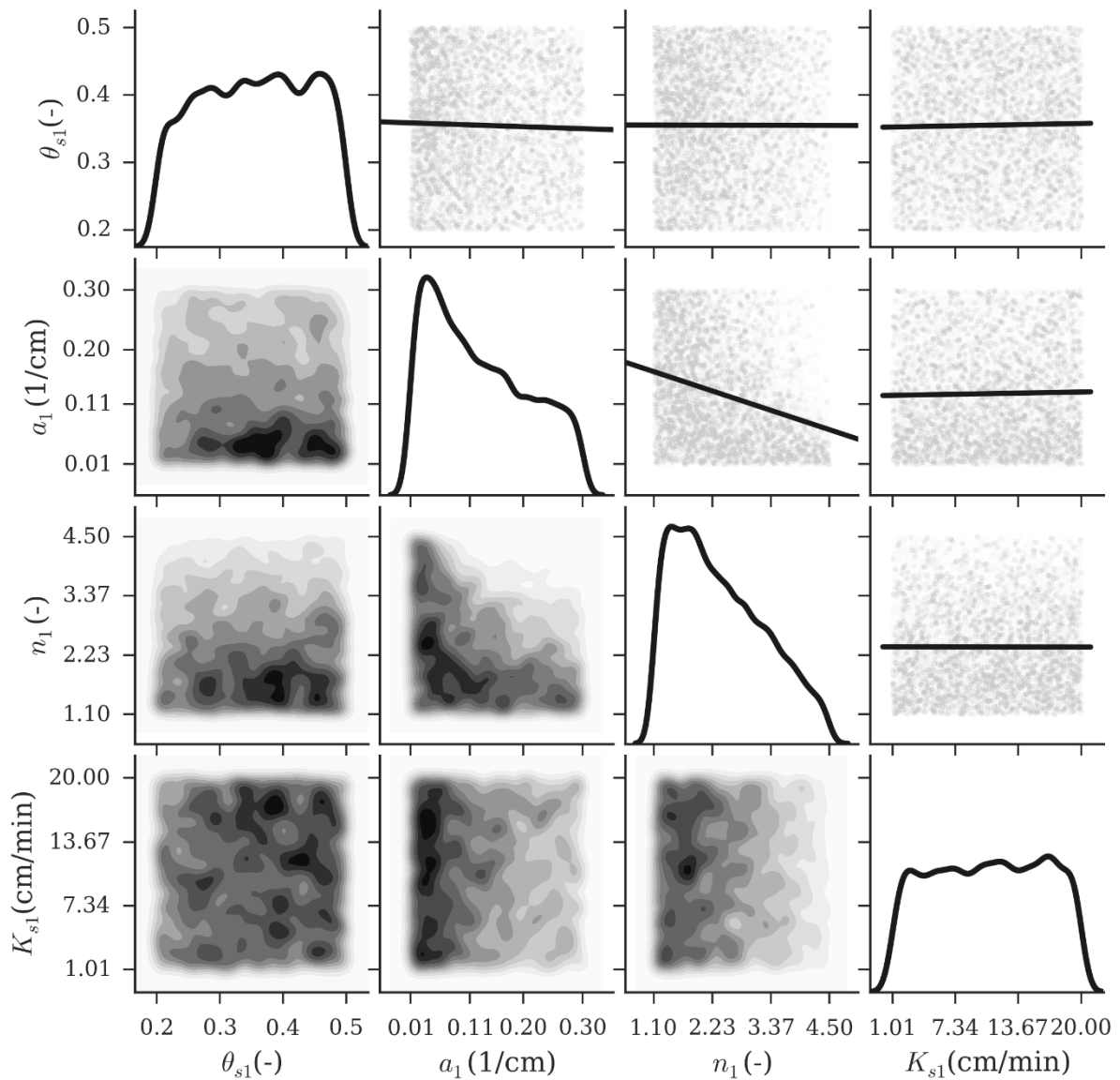


Figure 3.7 Bivariate KDE plots (below diagonal), univariate KDE plots (diagonal), and correlation plots (above diagonal) for Scenario II.

Figure 7 shows the univariate and bivariate KDE plots as well as the correlation plots for parameters of the wear layer. It is evident that no clear correlation exists between various parameters (Fig. 7), except for a negative correlation trend between parameters a_1 and n_1 , but

only with a small magnitude. The maximum correlation coefficient, in absolute values, was -0.531 between parameters a_4 and n_4 .

The univariate KDE for parameters θ_{s1} - K_{s1} indicates a platykurtic distribution of *behavioral* solutions without a clear identification of a denser region across the parameter space. On the other hand, for parameters a_1 and n_1 , the univariate KDEs indicate a more leptokurtic distributions, especially for n_1 , for which a denser region of solutions between 1.1-2.8 is identifiable.

The bivariate KDEs give a better description of the location of *behavioral* regions in the bidimensional parameter space than the univariate KDEs. The bivariate KDE for the two most sensitive parameters, a_1 and n_1 , indicate the presence of a denser region in the range of $n_1=(1.1, 2.8)$, and $a_1=(0.01, 0.15 \text{ 1/cm})$. The bivariate plots, θ_{s1} - a_1 and θ_{s1} - n_1 , indicate the presence of a denser region in the range of $\theta_{s1}=(0.25, 0.40)$, a region that was not clearly indicated by the univariate plot for θ_{s1} . The saturated hydraulic conductivity, K_{s1} , exhibits a multimodal behavior characterized by several potential regions of interest. A potential *behavioral* region may be identified in the range of $K_{s1}=(7.0, 15.0 \text{ cm/min})$.

3.3.5 Particle Swarm Optimization

The results and conclusions from the coupled GSA-Monte Carlo filtering analysis were used to reduce the ranges of parameters for the PSO. The reduction was applied only for parameters that exhibited well identifiable *behavioral* regions in multivariate plots. The original ranges were kept for parameters that displayed high multimodality, in order to avoid the convergence of PSO to the local optimum. Table 3.7 reports the new ranges for all parameters.

Table 3.7 Reduced ranges of optimized parameters for the optimization process.

| | Scenario I | Scenario II |
|----------------------|----------------------|--------------------|
| Parameter | Reduced range | |
| θ_{s1} [-] | 0.2-0.5 | 0.2-0.4 |
| a_1 [1/cm] | 0.001-0.1 | 0.001-0.15 |
| n_1 [-] | 3.0-4.5 | 1.1-2.8 |
| K_{s1} [cm/min] | 10.0-20.0 | 1.5-20.0 |
| θ_{s2} [-] | 0.25-0.5 | 0.2-0.4 |
| a_2 [1/cm] | 0.2-0.3 | 0.1-0.2 |
| n_2 [-] | 1.1-4.5 | 1.1-4.5 |
| K_{s2} [cm/min] | 1.0-20.0 | 3.0-20.0 |
| θ_{s3} [-] | 0.20-0.40 | 0.001-0.05 |
| a_3 [1/cm] | 0.001-0.05 | 0.001-0.05 |
| n_3 [-] | 1.1-4.5 | 1.5-4.5 |
| K_{s3} [cm/min] | 1.0-100.0 | 20.-100.0 |
| $\theta_{s,im3}$ [-] | - | 0.2-0.4 |
| ω_3 [1/min] | - | 0.00001-0.009 |
| θ_{s4} [-] | 0.01-0.2 | 0.001-0.05 |
| a_4 [1/cm] | 0.15-0.3 | 0.15-0.3 |
| n_4 [-] | 2.0-4.0 | 1.5-3.5 |
| K_{s4} [cm/min] | 1.0-100.0 | 1.0-100.0 |
| $\theta_{s,im4}$ [-] | - | 0.15-0.3 |
| ω_4 [1/min] | - | 0.00001-0.009 |

Figure 8 compares measured and modeled hydrographs for the two scenarios. The PSO for Scenarios I and II resulted in *NSE* values of 0.43 and 0.81, respectively. Both *NSE* values of the objective function are higher than zero and thus admissible (Moriassi et al., 2007). However, the implementation of the dual-porosity model for the base and sub-base layers in Scenario II provides a more accurate description of the hydraulic behavior of the permeable

pavement. In particular, the dual-porosity model is able to accurately reproduce the fast hydraulic response of the permeable pavement and the long-tailing behavior of the measured hydrograph. The modeled hydrograph for Scenario I appears less accurate in reproducing the dynamics of the observed hydrograph, especially the fast response of the pavements to precipitation.

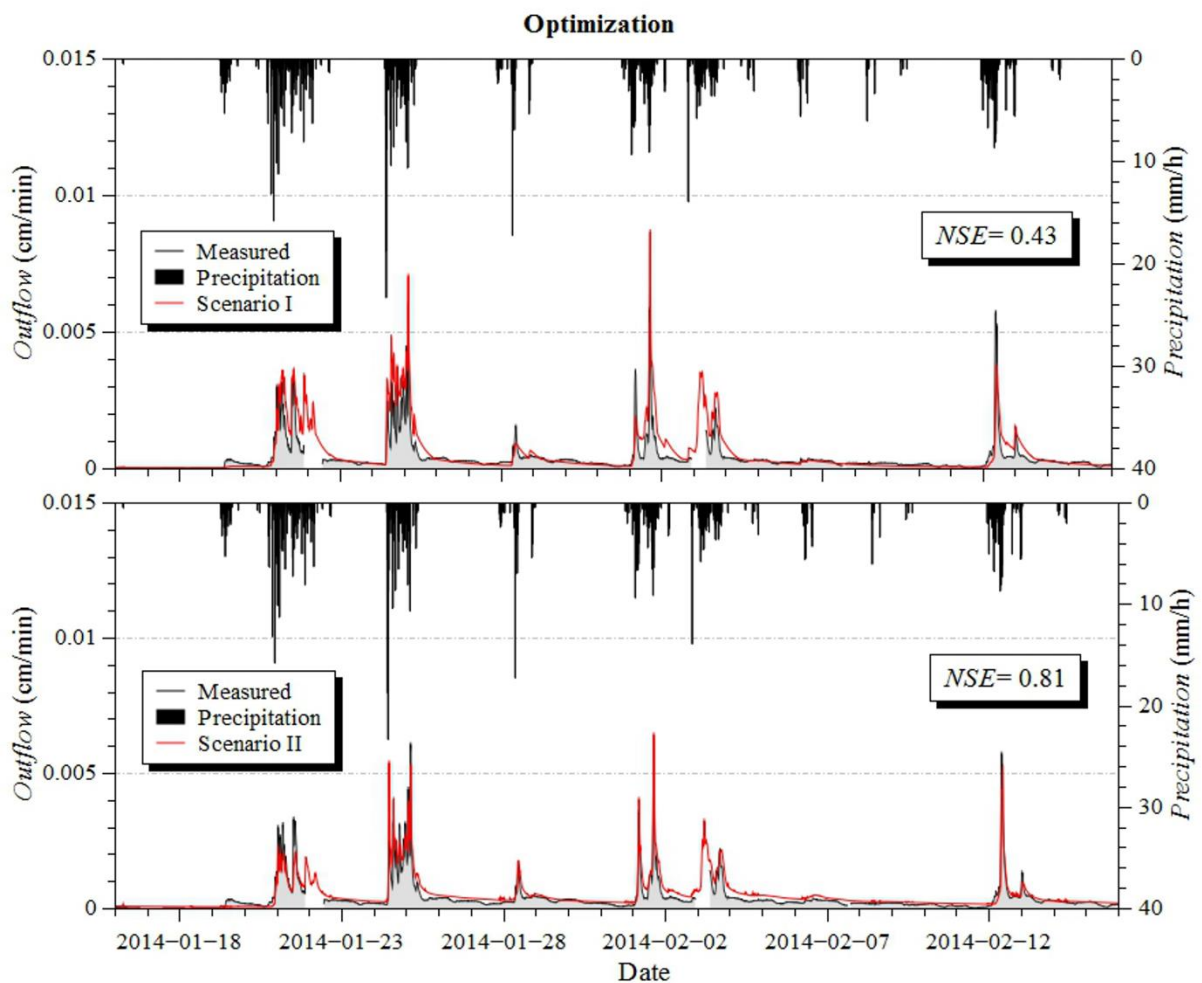


Figure 3.8 Comparison between the modeled and measured hydrographs for Scenarios I (top) and II (bottom) for the optimization process.

Optimized parameters for the two scenarios are reported in Table 3.8. Significant differences emerge between the two scenarios in terms of estimated values of the saturated water contents, θ_{s1} and a_1 ; differences between estimated values of the saturated hydraulic conductivities, K_{s1} and n_1 , are less pronounced. For layer 2, while estimated values of saturated water contents are very similar, huge differences arise between estimated pore-size distribution indices, n_2 , which for Scenario I is less than half of its value for Scenario II. Also, K_{s2} is considerably lower for Scenario II than for Scenario I. Estimated values of dual-porosity parameters confirm the assumptions made about the fractured nature of the base and subbase layers. While the saturated water content for the mobile domain is very low, the porous matrix possesses a high storage capacity as indicated by the large value of the immobile saturated water content. In particular, the overall porosity of the base layer is about 40% and 30% for the subbase layer. The result for the base layer is slightly higher than the prescriptions of ICPI, which recommends a porosity of 30-35%. The estimated porosity for the subbase layer is 30%, which is lower than the prescribed porosity of about 40%. This difference can be related to the simplifications made in the mobile-immobile dual porosity model for the description of preferential flow and uncertainties related to the effective gradation of the stone material used. However, the significant increase in the accuracy between the single-porosity model and the dual-porosity model suggests that the hydraulic behavior of the base and subbase layers is strongly affected by fast preferential flows in interconnected fractures and the accumulation of water in the rock matrix. This behavior is in agreement with results reported in the literature. For example, Illgen et al. (2007) reported that the water contents in the base and sub-base layers only marginally increased during rainfall events, and that the lower layers act as a storage tank.

Table 3.8 Optimized soil hydraulic parameters for both scenarios.

| Scenario I | | | | | | | | | |
|-------------------|----------------|----------------|------------|---------|----------------|---------|---------------------|---------------------|------------------|
| Layer | θ_r [-] | θ_s [-] | a [1/cm] | n [-] | K_s [cm/min] | L [-] | $\theta_{r,im}$ [-] | $\theta_{s,im}$ [-] | ω [1/min] |
| Wear | 0.045 | 0.2 | 0.002 | 3.0 | 10 | 0.5 | - | - | - |
| Bedding | 0.03 | 0.3 | 0.3 | 4.47 | 20 | 0.5 | - | - | - |

| | | | | | | | | | |
|--------------------|-------|-------|-------|------|------|-----|---|------|---------|
| Base | 0 | 0.2 | 0.023 | 2.85 | 68.7 | 0.5 | - | - | - |
| Sub-base | 0 | 0.01 | 0.27 | 2.41 | 96.7 | 0.5 | - | - | - |
| Protection | 0.03 | 0.3 | 0.3 | 4.47 | 20 | 0.5 | - | - | - |
| Scenario II | | | | | | | | | |
| Wear | 0.045 | 0.287 | 0.03 | 2.67 | 7.33 | 0.5 | - | - | - |
| Bedding | 0.03 | 0.298 | 0.113 | 3.04 | 3.87 | 0.5 | - | - | - |
| Base | 0 | 0.044 | 0.021 | 4.33 | 93.2 | 0.5 | 0 | 0.35 | 0.00017 |
| Sub-base | 0 | 0.001 | 0.247 | 2.17 | 56.3 | 0.5 | 0 | 0.29 | 0.0013 |
| Protection | 0.03 | 0.298 | 0.113 | 3.04 | 3.87 | 0.5 | - | - | - |

Both scenarios exhibit low values of porosity for the base and sub-base layers. For scenario II, the total porosity is divided between the mobile and immobile domains. Flow is restricted only to highly conductive and interconnected fractures, which represent a relatively small part of the domain, while the immobile domain provides the storage capacity. While Scenario II assumes overlapping and interacting continua, Scenario I assumes a single continuum approach for all layers. When the optimized value of porosity is very low, such as for the sub-base layer, it is necessary to interpret the optimized values differently than for typical Richards' type flow. In such case, especially for flow in crushed stones, the model tends to approximate a combination of film flow and fingering that likely occur in this layer. This hydraulic behavior is similar to the one reported, for example, by Hodnet and Bell (1990) for unsaturated flow in a medium composed largely of chalk cobbles. In their study, Tokunaga and Wan (1997) analyzed the influence of film flow on unsaturated flow in fractures. High velocities of film flow measured in their study suggested that film flow contributed significantly to preferential flow in fractured rocks. Our model, based on a macroscopic description of this fast unsaturated flow, shares some similarities with the active fracture model proposed by Liu et al. (1998). This approach divides the pore space into two parts, active and inactive. Flow and transport occurs only within the active pore space, with the inactive part simply bypassed. Liu et al. (1998) further assumed that van Genuchten (1980) relations are

approximately valid for the active pore space. In a separate study, Liu et al. (2003) reports values of porosity between 0.01 and 0.03 for the pore space used with the active fracture model.

3.3.6 Confidence Regions

Since parameter estimation involves a variety of possible errors, including measurement errors, model errors, and numerical errors, an uncertainty analysis of the optimized parameters constitutes an important part of parameter estimation. In order to evaluate the uncertainty associated with the estimated parameters, a confidence region around the best solutions optimized with PSO were calculated using HYDRUS-1D. HYDRUS-1D uses the linear approximation method to identify the confidence region around estimated parameters β , resulting in ellipsoid contours centered at β .

Table 3.9 Confidence intervals (CI) for optimized parameters for both scenarios.

| Parameter | Scenario I | | Scenario II | |
|-------------------|------------|--------|-------------|--------|
| | Value | CI | Value | CI |
| θ_{s1} [-] | 0.2 | 0.057 | 0.287 | 0.007 |
| a_1 [1/cm] | 0.002 | 0.0006 | 0.029 | 0.0008 |
| n_1 [-] | 3 | 0.783 | 2.67 | 0.058 |
| K_{s1} [cm/min] | 10 | 4.4 | 7.33 | 0.272 |
| θ_{s2} [-] | 0.3 | 0.072 | 0.29 | 0.009 |
| a_2 [1/cm] | 0.3 | 0.062 | 0.11 | 0.002 |
| n_2 [-] | 4.47 | 1.08 | 3.04 | 0.052 |
| K_{s2} [cm/min] | 20 | 6.5 | 3.87 | 0.084 |
| θ_{s3} [-] | 0.2 | 0.048 | 0.044 | 0.001 |
| a_3 [1/cm] | 0.023 | 0.003 | 0.021 | 0.0005 |
| n_3 [-] | 2.85 | 0.537 | 4.33 | 0.139 |
| K_{s3} [cm/min] | 68.73 | 19.7 | 93.2 | 3.172 |

| | | | | |
|----------------------|------|-------|---------|----------|
| $\theta_{s,im3}$ [-] | - | - | 0.35 | 0 |
| ω_3 [1/min] | - | - | 0.00017 | 0.000003 |
| θ_{s4} [-] | 0.01 | 0.002 | 0.001 | 0.00003 |
| a_4 [1/cm] | 0.27 | 0.018 | 0.247 | 0.004 |
| n_4 [-] | 2.41 | 0.121 | 2.17 | 0.039 |
| K_{s4} [cm/min] | 96.7 | 9.2 | 56.3 | 1.051 |
| $\theta_{s,im4}$ [-] | - | - | 0.288 | 0 |
| ω_4 [1/min] | - | - | 0.0013 | 0.00002 |

Although restrictive and only approximately valid for nonlinear problems, an uncertainty analysis provides a means to compare confidence intervals between parameters, thereby indicating which parameters should be independently measured or estimated. Confidence intervals have been calculated using the Student's t distribution with a confidence level of 95%. It is evident from Table 9 that confidence intervals are narrower for Scenario II, and that the most uncertain parameters are the saturated hydraulic conductivities for different layers.

3.3.7 Model Validation

In order to evaluate the reliability of the estimated parameters, the model has been validated on another independent set of experimental data. Figure 10 shows a comparison between measured and modeled hydrographs for the two scenarios during the validation period.

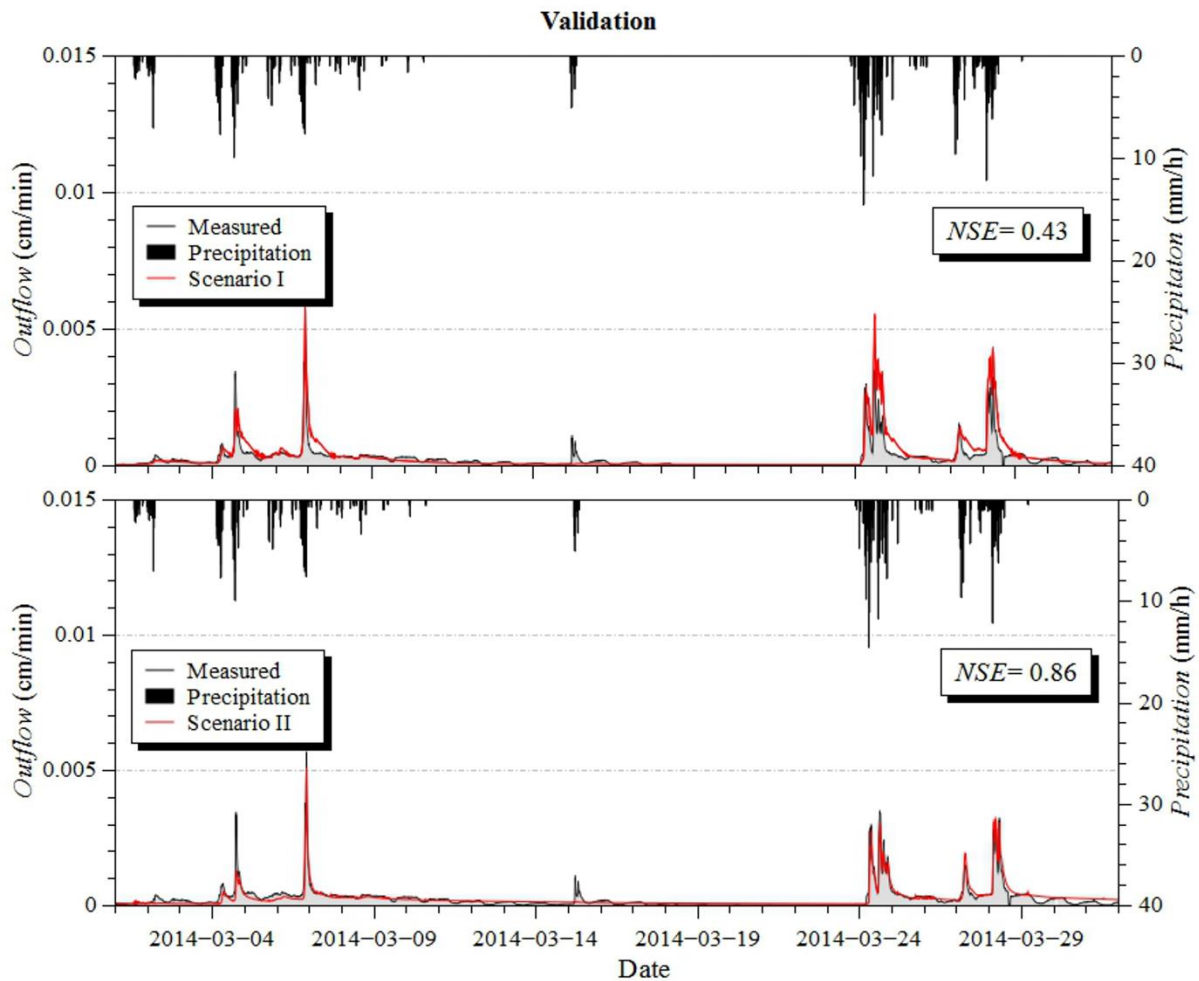


Figure 3.9 Comparison between the modeled and measured hydrograph for the two scenarios for the validation period.

The value of the objective functions are $NSE = 0.43$ for Scenario I and $NSE = 0.86$ for Scenario II. For Scenario I, the value of the objective function remains the same, which confirms the reliability of the calibrated model. Although the simulated hydrograph provides an overall sufficiently accurate description of the hydraulic behavior of the pavement, it is less accurate during rainfall events, which may be a time period of main interest. For Scenario II, the value of the objective function actually increased and reached the value $NSE = 0.86$, which

is very high and reflects the accuracy of the modeled hydrograph. Also the description of the hydraulic behavior of the pavement during rainfall events is optimal. This capability of the calibrated model is important when dealing with the analysis of combined traditional drainage systems and LID techniques. A correct description of the hydrograph during precipitation gives information about the lag time and the intensity of peak flow, which are fundamental for both a comprehensive hydraulic analysis of drainage systems, and for the evaluation of benefits of LIDs implementation. The initial part of the hydrograph appears to be underestimated, which may be related to the influence of the unknown initial conditions. The model was not able to reproduce outflow induced by the precipitation event on March 15. This may be related to an overestimation of potential evaporation calculated using a literature value of albedo, which could result in an overestimation of the storage capacity of the pavement at the beginning of the precipitation event, which had a total volume of 6 mm. As a result, the model predicted that the pavement retained all the precipitation volume. A better characterization of evaporation could help in increasing the accuracy of the model, which is already high.

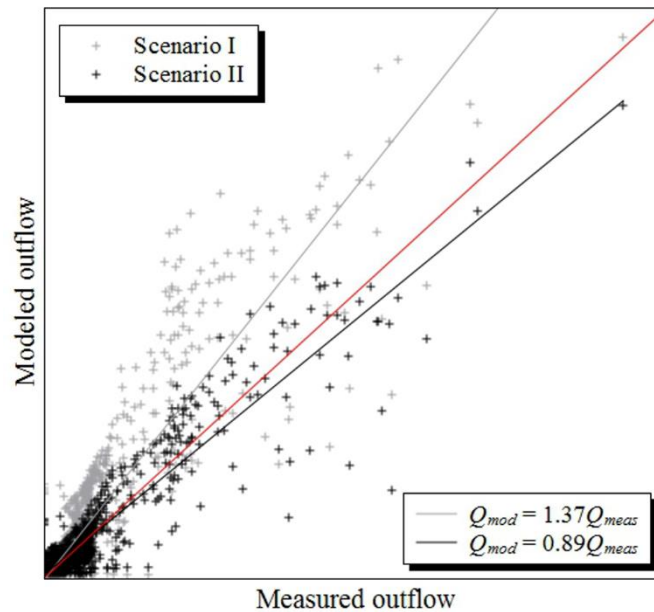


Figure 3.10 Comparison between the modeled and measured outflows for the two scenarios for the validation period.

Figure 10 directly compares the measured outflows with those calculated by the two modeling scenarios. The red bisector line represents conditions when modeled and measured outflows are perfectly matched. Linear regression lines are reported for both scenarios. Since the Scenario I tends to overestimate the outflow fluxes, the difference between the bisector and the linear regression line (gray) for scenario I is substantial. On the other hand, Scenario II tends to only slightly underestimate the outflow fluxes, and thus the slopes of the bisector and the linear regression line (black) for Scenario II are similar. The simulated hydrographs for both scenarios tend to introduce some bias in the estimation of peak flows. This aspect is related to the choice of the *NSE* as the objective function for the optimization. The *NSE* is focused on the general behavior of the hydrograph rather than on particular components such as peak flows. A multi-objective optimization that would include an objective function targeted to peak flow estimates could represent a more appropriate approach if estimates of peak flows were the main goal of calibration. However, even of great interest, the multi-objective optimization is

out of the scope of this paper. Overall, the validation process demonstrated the reliability of the calibrated models for both scenarios.

3.4 Conclusions

In this paper, we investigated the suitability of the mechanistic model, HYDRUS-1D, to correctly describe the hydraulic behavior of a permeable pavement installed at the University of Calabria. We considered two different scenarios in describing the system. In Scenario I, we assumed that flow on all layers can be described using a single-porosity model, while in Scenario II, we assumed that a dual-porosity mobile-immobile model is needed to describe flow in the base and subbase layers. The widely used Nash-Sutcliffe efficiency index was used to assess the models. A Global Sensitivity Analysis, coupled with a Monte Carlo filtering procedure, was carried out before the model calibration. Sensitivity analysis results suggested that the model is non-additive and mainly driven by parameter interactions in both scenarios. The first-order effects only accounted for 56% of output variance for Scenario I and 53% for Scenario II. Sensitivity analysis also revealed that the wear layer mainly influenced the hydraulic behavior of the pavement. A subsequent Monte Carlo filtering procedure was applied to the runs performed during the sensitivity analysis in order to identify the *behavioral* regions and to reduce parameter uncertainty. Both univariate and bivariate Kernel Density Estimation plots were used to inspect the response surfaces and identify the *behavioral* regions. This analysis revealed the high multimodality of the response surfaces, which suggested the use of a global optimization algorithm for parameter estimation. Correlation coefficients of the filtered sample were also computed, indicating a general low correlation between parameters. Based on the results of the Monte Carlo filtering, a heuristic global optimization method based on the Particle Swarm algorithm was used for parameter estimation. The calibrated model for Scenario I exhibited an optimum $NSE = 0.43$, while for Scenario II, it reached $NSE=0.81$. The

optimized parameters were then validated against an independent set of experimental data, resulting in $NSE = 0.43$ for Scenario I and $NSE = 0.86$ for Scenario II. The results of optimization and validation clearly indicated that the implementation of the dual-porosity model for the base and subbase layers produced more accurate results than the single-porosity model and described much better the hydraulic behavior of pervious pavement. Results also confirmed the validity of the assumption that the hydraulic behavior of the base and subbase layers was similar to the behavior of a fractured rock, which is characterized by the highly permeable interconnected fractures and the highly storative rock matrix. The main advantage in using a simple, dual-porosity, mobile-immobile model with a saturation-based mass transfer is that this model requires only two additional parameters compared to the single-porosity model. Further significant improvements could be obtained by characterizing the hydraulic properties of the wear layer in the laboratory, as suggested by the sensitivity analysis.

Chapter 4 On the use of surrogate-based modeling for the numerical analysis of Low Impact Development techniques

4.1 Introduction

During the last few decades, stormwater management has become a major component of the prevention of floods in urban areas and for the preservation of water resources. An increase of impervious surfaces, connected with demographic growth, has altered the natural hydrological cycle by reducing the infiltration and evaporation capacity of urban catchments while also increasing surface runoff. In their report, the Organization for Economic Co-operation and Development (OECD) (2013) identified an expected increase in flash and urban floods in large parts of Europe as one of the major issues for the future.

In this context, urban drainage systems play a fundamental role in improving the resilience of cities. In recent years, an innovative approach to land development known as a Low Impact Development (LID) has gained increasing popularity. A LID is a 'green' approach to storm water management that seeks to mimic the natural hydrology of a site using decentralized micro-scale control measures (Coffman, 2002). LID practices consist of bioretention cells, infiltration wells/trenches, storm water wetlands, wet ponds, level spreaders, permeable pavements, swales, green roofs, vegetated filter/buffer strips, sand and gravel filters, smaller culverts, and water harvesting systems. Several studies have evaluated the benefits of LIDs. For example, Newcomer et al. (2014) used a numerical model to demonstrate the benefits of LIDs, and an infiltration trench in particular, on recharge and local groundwater resources for future climate scenarios. In another paper, Berardi et al. (2014) demonstrated how green

roofs may contribute to the development of more sustainable buildings and cities. Green Roofs (GR) were able to significantly reduce peak rates of storm water runoff (Getter et al., 2007) and retain rainfall volumes with retention efficiencies ranging from 40% to 80% (Bengtsson et al., 2004). Permeable pavements offered great advantages in terms of runoff reduction (Carbone et al., 2014; Collins et al., 2008), water retention, and water quality (Brattebo and Booth, 2003). Even though the results of available studies are encouraging, more research is needed to precisely assess the impact of LIDs on the hydrological cycle.

As pointed out by several authors (e.g., Elliot and Trowsdale, 2007; Wong et al., 2006), there is a strong demand for predictive models that can be applied across a range of locations and conditions to predict the general performance of a range of stormwater treatment measures. In recent years, researchers have focused their attention on applying and developing empirical, conceptual, and physically-based models for LIDs analysis. In their review article, Li and Babcock (2014) reported that there were more than 600 papers published worldwide involving green roofs, with a significant portion of them related to modeling. Several studies demonstrated that physically-based models can provide a rigorous description of various relevant processes such as variably-saturated water flow, evaporation and root water uptake, solute transport, heat transport, and carbon sequestration. Brunetti et al. (2016) used a mechanistic model, HYDRUS-3D (Šimůnek et al., 2016, 2008), to analyze an extensive green roof in a Mediterranean climate. The model, previously validated against field scale measurements, was used to investigate the hydraulic response of a green roof to single precipitation events and its hydrological behavior during a two-month period. Metselaar (2012) used the SWAP model (van Dam et al., 2008) to simulate the one-dimensional water balance of a substrate layer on a flat roof with plants. Li and Babcock (2015) used HYDRUS-2D to model the hydrologic response of a pilot green roof system. The model was calibrated using water content measurements obtained with TDR (Time Domain Reflectometer) sensors. The calibrated model was then used to simulate the potentially beneficial effects of irrigation management on the reduction of runoff volumes. The VFSMOD model (Munoz-Carpena and

Parsons, 2004) was extensively used for the analysis of the hydraulic behavior and solute transport of vegetated filter strips (Abu-Zreig et al., 2001; Dosskey et al., 2002).

However, physically-based modeling often involves highly nonlinear, partial, differential equations that are solved using various numerical approximation methods, requiring a high computational cost. Moreover, a comprehensive simulation framework includes model calibration, sensitivity analysis, and uncertainty quantification aimed at enhancing confidence in the model and its ability to describe real world systems. These tasks require running the simulation model hundreds or thousands of times and thus the computational cost exponentially increases.

Surrogate modeling focuses on developing and using a computationally inexpensive *surrogate* of the *original* model. The main aim is to approximate the response of an original simulation model, which is typically computationally intensive, for various quantities of interest (Razavi et al., 2012). Surrogate models have been widely applied in various water-related and environmental modeling problems. Khu and Werner (2003) used artificial neural networks (ANN) in conjunction with genetic algorithms (GA) to reduce the computational budget required in the uncertainty quantification framework of the rainfall-runoff model SWMM. The GA was first used to identify the areas of higher importance in the parameter space and ANNs were then used to approximate the response surface in these areas (Khu and Werner, 2003). Borgonovo et al. (2012) tested a surrogate model for the estimation of the sensitivity indices of an environmental model. Zhang et al. (2009) evaluated ANN and Support Vector Machine (SVM) for approximating the Soil and Water Assessment Tool (SWAT) model in two watersheds. Keating et al. (2010) used a surrogate model to carry out a comparison between the null-space Monte Carlo sampling (NSMC) and the Differential Evolution Adaptive Metropolis (DREAM) algorithm for parameter estimation and uncertainty quantification. In another study, Laloy et al. (2013) used Polynomial Chaos Expansion (PCE) to emulate the output of a large-scale flow model. The surrogate model was used in a Bayesian analysis framework to derive the posterior distribution of different parameters. In their study, Younes et al. (2013) used a surrogate model to estimate three soil hydraulic parameters from a

drainage experiment. In particular, PCE was used to run a Monte Carlo Markov Chain (MCMC) analysis. However, although the widespread diffusion of surrogate modeling tools could drastically reduce computational budgets, their use for physically-based modeling of LIDs is still unexploited.

The primary objective of this paper is to investigate the suitability of surrogate modeling for the numerical analysis of LIDs techniques by analyzing data from a real case study. The mechanistic model HYDRUS-2D is first used to simulate the hydraulic behavior of a Stormwater Filter (SF) at the University of Calabria, Italy. The surrogate model, based on kriging, is then used to carry out a Global Sensitivity Analysis (GSA) and a Global Optimization of soil hydraulic parameters. The use of a surrogate model for the sensitivity analysis of model outputs to soil hydraulic properties represents a new application of this technique that can provide a significant contribution in this field.

The problem is addressed in the following way. First, the evaporation method is used to measure the soil hydraulic properties of the vegetated substrate above the gravel filter, for which the hydraulic properties were unknown. The measured soil hydraulic properties of the vegetated substrate and the selected ranges of parameters of the filter layer are then used in HYDRUS-2D to set up the model. A Latin Hypercube Sampling (LHS) plan is used to build a first trial of the surrogate model. Before continuing with the other tasks, the surrogate model is validated and improved by using specific infill criteria. Once validated, the surrogate model is first used for the GSA based on Sobol's method to compute the sensitivity measures, and then for the inverse parameter estimation carried out using the Particle Swarm Optimization (PSO) algorithm. Finally, estimated parameters are used in the original mechanistic model for the validation purpose.

4.2 Materials and Methods

4.2.1 Stormwater Filter and Site Description

The University of Calabria is located in the south of Italy, in the vicinity of Cosenza (39°18' N 16°15' E). The climate is Mediterranean with a mean annual temperature of 15.5 °C and average annual precipitation of 881.2 mm. The stormwater filter (SF) has a surface area of 125 m², an average slope of 2%, and a total profile depth of 0.75 m. Figure 1 shows a schematic of the SF.

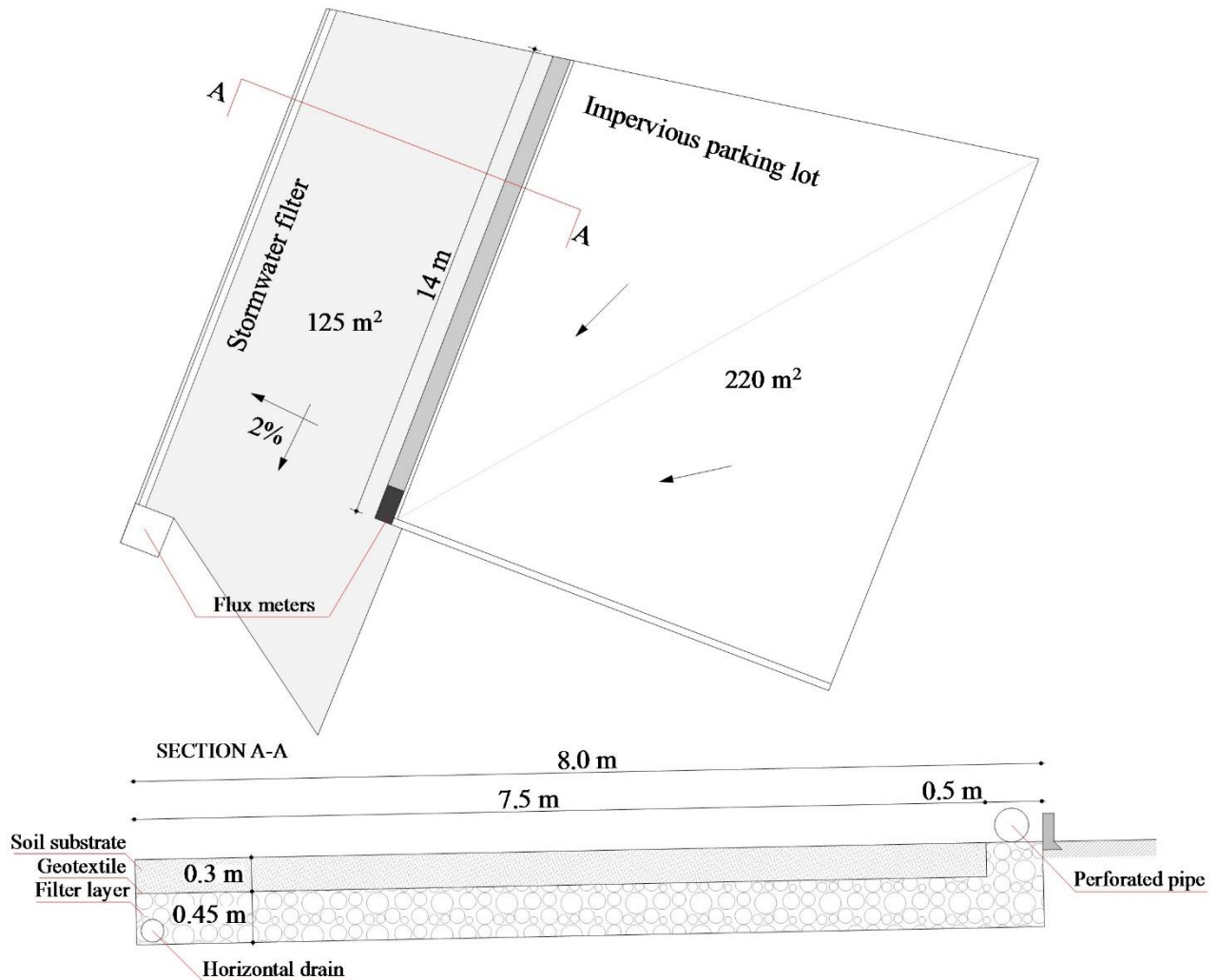


Figure 4.1 A schematic of the experimental site (top) and a typical cross-section (bottom) of the stormwater filter.

The filter layer is covered by a vegetated soil substrate with a measured bulk density of 1.59 g/cm^3 . A high permeability geotextile with a fiber area weight of 60 g/m^2 is placed at the interface between the soil substrate and the filter layer to prevent fine particles from migrating into the underlying layer. The filter layer is composed of a gravelly material characterized by

a high permeability. An impervious membrane is placed at the bottom of the profile to prevent water from percolating into deeper horizons.

The SF is used to treat stormwater runoff from the adjoining impervious parking lot, which is characterized by an area of 220 m². Stormwater runoff from the parking lot is first conveyed into a manhole and then to an instrumented channel where the flow rate is measured by a flow meter composed of a rectangular, sharp crested weir coupled with a pressure transducer. The pressure transducer (Ge Druck PTX1830) measures the water level inside the channel and has a range of measurements of 75 cm with an accuracy of 0.1% of the full scale. The pressure transducer was calibrated in the laboratory using a hydrostatic water column, linking the electric current intensity with the water level inside the column. An exponential head-discharge equation for the flow meter was obtained by fitting the experimental data.

Measured runoff is next conveyed into a 14 m long, horizontal perforated pipe where it is distributed on the top of the filter layer (Fig. 1). As shown in Figure 1, the soil substrate is not used to treat stormwater runoff, which is directly routed into the filter, but only to increase the retention and evapotranspiration capacity of the system itself. The baseflow is collected in a horizontal drain, which consists of a perforated PVC pipe, and is conducted to a manhole for quantity and quality measurements. A second flow meter, composed of a PVC pipe with a sharp-crested weir and a pressure transducer, measures the flow rate. Runoff and baseflow data were acquired with a time resolution of one minute and stored in a SQL database. No measurements of pressure heads or volumetric water contents inside of the filter were taken.

A weather station located directly at the site measures precipitation, wind velocity and direction, air humidity, air temperature, atmospheric pressure, and global solar radiation. Rain data are measured using a tipping bucket rain gauge with a resolution of 0.254 mm and an acquisition frequency of one minute. Climatic data are acquired with a frequency of five minutes. Data are processed and stored in the SQL database.

Two month-long data sets were selected for the analysis (Fig. 2). The first data set, which started on 2014-01-15 and ended on 2014-02-15, was used for obtaining the surrogate model. The second data set, which started on 2014-03-01 and ended on 2014-03-31, was used for

model validation. The precipitation totals for the first and second data sets were 274 and 174 mm, respectively. The second data set was selected because it had significantly different meteorological dynamics than during the first period. The optimization set is characterized by multiple rain events with few dry periods. The validation set has fewer rain events, which are concentrated at the beginning and end of the time period and separated by a relatively long dry period.

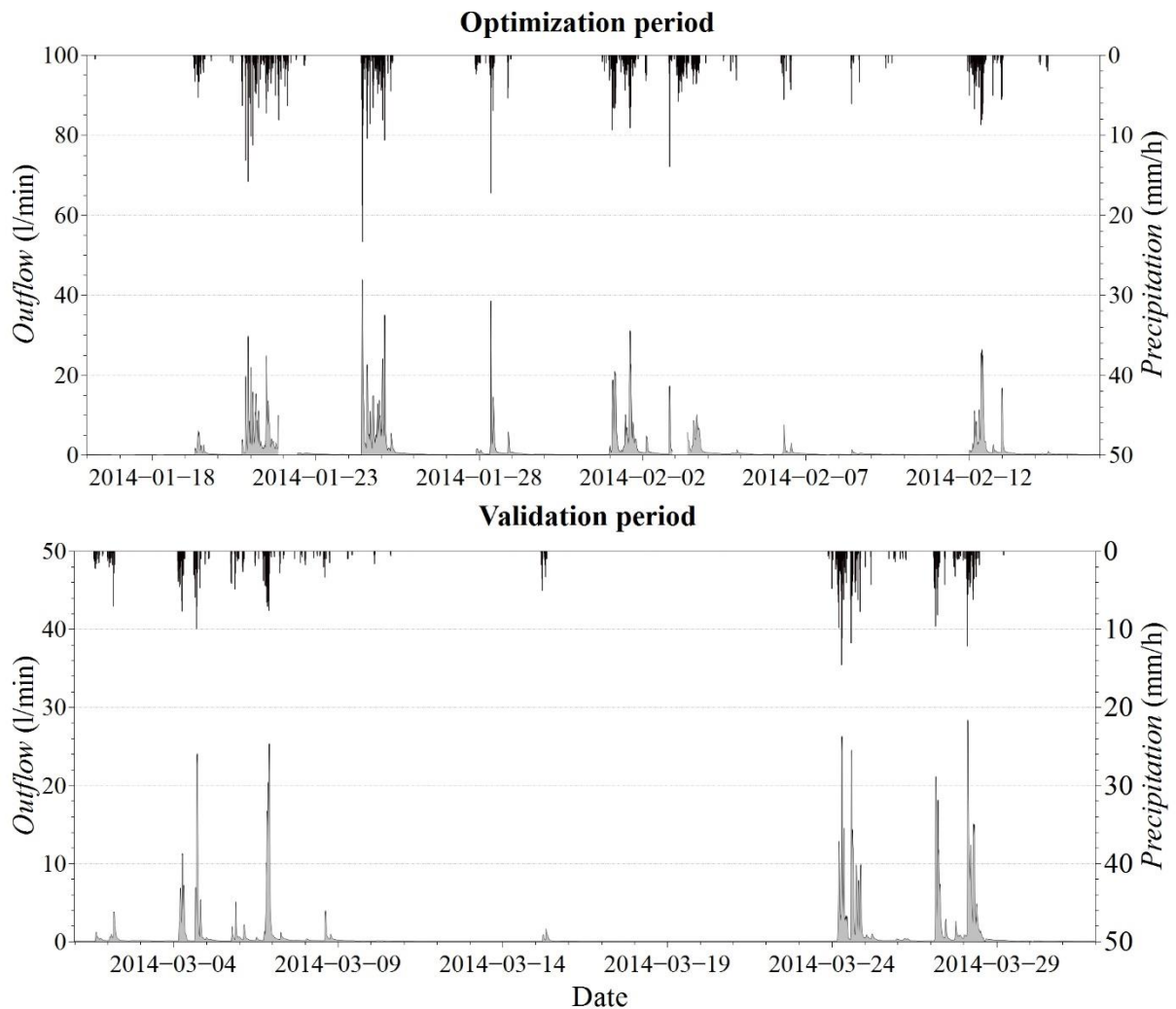


Figure 4.2 Precipitation (black line) and subsurface flow (grey line) for the optimization (top) and validation (bottom) periods, respectively.

Hourly reference evapotranspiration was calculated using the Penman-Monteith equation (Allen et al., 1998). Considering that vegetation mainly consisted of herbaceous plants, an average value of albedo of 0.23 was assumed in calculations of net short-wave radiation (Breshears et al., 1997).

4.2.2 Evaporation Method and Parameter Estimation

4.2.2.1 Evaporation Method

Modeling of water flow in unsaturated soils by means of the Richards equation requires knowledge of the water retention function, $\theta(h)$, and the hydraulic conductivity function, $K(h)$, for each soil layer of the SF, where θ is the volumetric water content [L^3L^{-3}], h is the pressure head [L], and K is the hydraulic conductivity [LT^{-1}]. In order to reduce the dimensionality of the optimization problem, the soil hydraulic properties of the soil substrate were measured in the laboratory using a simplified evaporation method with an extended measurement range (down to -9,000 cm), as proposed by Schindler et al. (2010a, 2010b). For a detailed description of the modified evaporation method, please refer to Schindler et al. (2010a, 2010b).

Peters and Durner (2008) conducted a comprehensive error analysis of the simplified evaporation method and concluded that it is a fast, accurate, and reliable method to determine soil hydraulic properties in the measured pressure head range, and that the linearization hypothesis introduced by Schindler (1980) causes only small errors. The above cited method has already been used in the LIDs analysis for the determination of the unsaturated soil hydraulic properties of a green roof substrate (Brunetti et al., 2016b). In that study, the measured soil hydraulic properties were used in HYDRUS-3D to simulate the hydraulic behavior of a green roof and validated by providing optimal correspondence between simulated and measured outflows. The simplified evaporation method was similarly used in this study for the determination of the unsaturated hydraulic properties of the soil substrate. For a complete description of the system, please refer to UMS GmbH (2015).

The soil for the laboratory analysis was directly sampled from the SF using a stainless-steel sampling ring with a volume of 250 ml. The soil sample was saturated from the bottom before starting the evaporation test. The measurement unit and tensiometers were degassed using a vacuum pump, in order to reduce the potential nucleation sites in the demineralized water. Since Peters and Durner (2008) suggested a reading interval for structured soils of less

than 0.1 day, the reading interval was set to 20 minutes in order to have high resolution measurements. At the end of the experiment, the sample was placed in an oven at 105°C for 24 hours, and then the dry weight was measured.

4.2.2.2 Parameter Estimation

The numerical optimization procedure, HYPROP-FIT (Pertassek et al., 2015), was used to simultaneously fit retention and hydraulic conductivity functions to experimental data obtained using the evaporation method. Fitting was accomplished using a non-linear optimization algorithm that minimizes the sum of weighted squared residuals between model predictions and measurements. The software uses the Shuffled Complex Evolution (SCE) algorithm proposed by Duan et al. (1992), which is a global parameter estimation algorithm. The goodness-of-fit was evaluated in terms of the Root Mean Square Error (RMSE), while the Akaike information criterion (AIC) (Hu, 1987) was used to choose between different hydraulic conductivity functions. The software also provides 95% confidence intervals to assess the uncertainty in parameter estimation. In order to calculate the parameter uncertainties a linear approximation of the covariance matrix for each estimated parameter is calculated. The confidence interval for the i -th parameter is then computed by combining the covariance matrix and the upper $a/2$ quantile of the Student's t -distribution, where a is set to 0.05 for the computation of the 95% confidence intervals.

4.2.3 Modeling Theory

4.2.3.1 Water Flow and Root Water Uptake

The HYDRUS-2D software (Šimůnek et al., 2008) was used to model the hydraulic behavior of the SF. HYDRUS-2D is a two-dimensional model for simulating the movement of

water, heat, and multiple solutes in variably-saturated porous media. HYDRUS-2D numerically solves the Richards equation for multi-dimensional unsaturated flow:

$$\frac{\partial \theta}{\partial t} = \nabla[K \cdot \nabla(h + z)] - S \quad (21)$$

where t is time (T), z is the vertical coordinate (L), and S is a sink term ($L^3L^{-3}T^{-1}$), defined as a volume of water removed from a unit volume of soil per unit of time due to plant water uptake. The unimodal van Genuchten–Mualem (VGM) model (van Genuchten, 1980) was used to describe the soil hydraulic properties of the two layers:

$$\Theta = \begin{cases} \frac{1}{(1 + (\alpha|h|)^n)^m} & \text{if } h \leq 0 \\ 1 & \text{if } h > 0 \end{cases} \quad (22)$$

$$\Theta = \frac{\theta - \theta_r}{\theta_s - \theta_r}$$

$$K = \begin{cases} K_s \Theta^L \left[\left(1 - \left(1 - \Theta^{\frac{1}{m}} \right) \right)^m \right]^2 & \text{if } h < 0 \\ K_s & \text{if } h > 0 \end{cases} \quad (23)$$

$$m = 1 - \frac{1}{n}$$

where Θ is the effective saturation (-), α is a shape parameter related to the inverse of the air-entry pressure head (L^{-1}), θ_s and θ_r are the saturated and residual water contents, respectively (-), n and m are pore-size distribution indices (-), K_s is the saturated hydraulic conductivity (LT^{-1}), and L is the tortuosity and pore-connectivity parameter (-).

While the soil hydraulic properties of the soil substrate were determined using the simplified evaporation method, those of the filter were optimized in the surrogate analysis framework. However, not all parameters were included in the optimization process. The residual water content θ_r was fixed to 0, considering that the filter is composed of coarse gravel,

and the tortuosity L was set to 0.5, which is a common value in the literature. The initial range of the investigated parameters is reported in Table 4.1.

Table 4.1 Ranges of investigated parameters for the surrogate-based analysis.

| Parameter | Range |
|-------------------|------------|
| θ_s [-] | 0.1-0.3 |
| α [1/cm] | 0.001-0.3 |
| n_1 [-] | 3.0-7.0 |
| K_{s1} [cm/min] | 30.0-100.0 |

Feddes et al. (1978) defined S as:

$$S(h) = a(h) \cdot S_p \quad (24)$$

where $a(h)$ is a dimensionless water stress response function that depends on the soil pressure head h and has a range of values between 0 and 1, and S_p is the potential root water uptake rate. Feddes et al. (1978) proposed a water stress response function in which water uptake is assumed to be zero close to soil saturation (h_1) and for pressure heads larger (in absolute values) than the wilting point (h_5). Water uptake is assumed to be optimal between two specific pressure heads (h_2 , h_3 or h_4), which depend on a particular plant. At high potential transpiration rates (5 mm/day in the model simulation) stomata start closing at lower pressure heads (h_3) (in absolute value) than at low potential transpiration rates (1 mm/d) (h_4). Parameters of the stress response function for a majority of agricultural crops can be found in various databases (e.g., Taylor and Ashcroft, 1972; Wesseling et al., 1991). Considering that the vegetation cover was mainly constituted of herbaceous plants, parameters reported for grass in Wesseling et al. (1991) were used in this study.

The local potential root water uptake S_p was calculated from the potential transpiration rate T_p . Beer's equation was first used to partition reference evapotranspiration, calculated using the Penman-Monteith equation (Allen et al., 1998), into potential transpiration and potential soil evaporation fluxes (e. g., Ritchie, 1972). The partitioning of evapotranspiration

into potential transpiration and potential evaporation allows the computation of different actual fluxes in the soil-vegetation system. The Leaf Area Index (LAI) is needed to partition evaporation and transpiration fluxes. In this study, a LAI value of 2.29 as reported by Blanus et al. (2013) for a *sedum* mix was used, considering its similarity with the installed vegetation. For a detailed explanation of evapotranspiration partitioning, please refer to Sutanto et al. (2012).

HYDRUS-2D allows for the consideration of a spatially variable root distribution. In this study, a homogeneous root zone within a depth of 15 cm was defined. The root density was assumed to be uniform inside the root zone and zero in the remaining part of the numerical domain. The total potential transpiration flux from a transport domain is equal in HYDRUS to potential transpiration T_p , multiplied by the surface length associated with vegetation. This total potential transpiration flux is then distributed over the entire root zone for the computation of the actual root water uptake.

4.2.3.2 Numerical Domain and Boundary Conditions

The two-dimensional domain had a length of 8.0 m and a depth of 0.75 m. The geotextile was not included in the model considering its negligible thickness, its limited hydraulic effect due to its high permeability, and that its sole function was to separate the soil substrate from the filter layer. The domain was discretized into two-dimensional triangular elements using the MESHGEN tool of HYDRUS-2D. The mesh was refined in the right part of the domain, where the effect of the surface runoff from the parking lot was simulated. This refinement was necessary in order to numerically accommodate the significant pressure head gradients generated by infiltration of runoff, and thus to reduce the mass balance errors. The generated FE mesh had 736 nodes and 1,350 two-dimensional elements. The quality of the FE mesh was assessed by checking the mass balance error reported by HYDRUS-2D at the end of the

simulation. Mass balance errors, which in this simulation were always below 1%, are generally considered acceptable at these low levels.

The surface of the SF was exposed to precipitation, evapotranspiration, and surface runoff from the impervious parking lot. As a result, in HYDRUS, two different boundary conditions were specified at the top of the modeled domain, as well as at its bottom (Fig. 4.3).

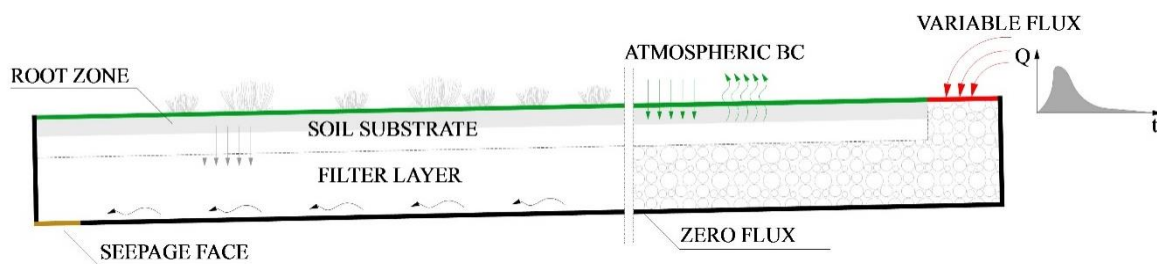


Figure 4.3 The spatial distribution of applied boundary conditions.

The “Atmospheric” boundary condition, which was assigned on the surface of the soil substrate (green line in Fig. 4.3), can exist in three different states: (a) precipitation and/or potential evaporation fluxes, (b) a zero pressure head (full saturation) during ponding when both infiltration and surface runoff occurs, and (c) an equilibrium between the soil surface pressure head and the atmospheric water vapor pressure head when atmospheric evaporative demand cannot be met by the substrate. The threshold pressure head, which was set to -10,000 cm, divides the evaporation process from the soil surface into two stages: (1) a constant rate stage when actual evaporation, equal to potential evaporation, is limited only by the supply of energy to the surface, and (2) the falling rate stage, when water movement to the evaporating sites near the surface is controlled by subsurface soil moisture and the soil hydraulic properties. In such conditions, actual evaporation, calculated as a result of the numerical solution of the Richards equation, is smaller than potential evaporation.

The “Variable Flux” boundary condition, which included both precipitation and measured surface runoff, was used in the area under the perforated pipe (red line in Fig. 4.3). Evaporation was excluded since most of the surface was covered by the perforated pipe, which reduced the exposure of the surface to wind and solar radiation.

A seepage face boundary condition (brown line in Fig. 4.3) was specified at the bottom left corner of the numerical domain to simulate the effect of the horizontal drain. A seepage face boundary acts as a zero pressure head boundary when the boundary node is saturated and as a no-flux boundary when it is unsaturated. A zero flux boundary condition (black line in Fig. 4.3) was applied to all remaining boundaries of the domain to simulate the effect of the impervious membrane placed at the bottom and on the sides of the SF.

The initial conditions were specified in terms of the soil water pressure head and were set to linearly increase with depth, from -90 cm at the top of the flow domain ($z = 0$) to -0.5 cm at the bottom ($z = -75$). The surface layers are assumed to be drier than the bottom layers since they are directly exposed to the atmosphere. The numerical model is expected to be sensitive to the initial conditions only during the first few simulated days.

4.2.4 Surrogate Based Model

4.2.4.1 Kriging

There are two broad families of surrogate modeling techniques: Response Surface Surrogates (RSS) and Lower-Fidelity Surrogates (LFS). While RSS are data-driven techniques for approximating the response surface of high-fidelity (original) models based on a limited number of original model evaluations, LFS are essentially cheaper-to-run, alternative simulation models with different levels of accuracy (Razavi et al., 2012). As pointed out by Razavi et al. (2012) in their review paper, LFS outperforms RSS when the dimensionality of the problem is high and the response surface landscape is characterized by multimodality. In

such circumstances, RSS would need a higher number of original model runs to correctly approximate the response surface. O'Hagan (2006) highlighted how the same number of design sites can lead to different parameters space coverages depending on the dimensionality of the problem. However, when the problem is low-dimensional and the response surface is characterized by a low or moderate multimodality, RSS are preferred since a limited number of high-fidelity model runs is required to build a reliable surrogate model.

The present study involves a SF model with four parameters to be investigated. Considering the low dimensionality of the problem, the kriging response surface approximation technique was used. Unlike other RSS, kriging models have their origins in mining and geostatistical applications involving spatially and temporally correlated data. The kriging technique has also been referred to in the literature as a Gaussian Process (GP) prediction (Rasmussen and Williams, 2006; Sacks et al., 1989). A Gaussian Process is formally defined as being a probability distribution over a (possibly infinite) number of variables, such that the distribution over any finite subset of them is a multi-variate Gaussian. As the Gaussian distribution is fully specified by its mean and covariance matrix, the GP is specified by a mean and a covariance function (Mackay, 1998). The mean is usually assumed to be zero, and, in such circumstances, the covariance function completely describes the GP behavior. One of the most attractive features of GP is that it treats the deterministic response of a computer model as the realization of a stochastic process, in particular a Gaussian random process, thereby providing a statistical basis for fitting. This capability provides a first approximation of uncertainty associated with each value predicted by the surrogate. Another advantage of kriging against other RSS techniques such as Artificial Neural Networks (ANN) or Support Vector Machines (SVM) is that kriging is an exact emulator. An exact emulator precisely predicts all design sites used to build the surrogate, while inexact emulators can introduce bias in such sites. As described by Razavi et al. (2012), an exact emulation is recommended for approximating the deterministic response of computer simulation models. Inexact emulators have smoothing capabilities that can help when the response surface is noisy (e.g., physical

experiments), however this feature can lead to poor approximation of the response surface when it is characterized by multiple local minima.

The kriging model is a combination of a polynomial model and a localized deviation model, which is based on a spatial correlation of samples (eq. 24):

$$y(x) = f(x) + Z(x) \quad (24)$$

where $y(x)$ is an unknown function of interest, $f(x)$ is an approximation function, and $Z(x)$ is the realization of a stochastic process with zero mean, the variance σ^2 , and nonzero covariance. While $f(x)$ globally approximates the response surface through design sites, $Z(x)$ creates localized deviations. The covariance matrix of $Z(x)$ is given by eq. (25):

$$Cov[Z(x^i), Z(x^j)] = \sigma^2 \Psi([R(x^i, x^j)]) \quad (25)$$

where Ψ is the $p \times p$ symmetric correlation matrix and $R(x^i, x^j)$ is the correlation function between two of the p sampled data points. $R(x^i, x^j)$ can assume different forms and is specified by the user. In this study, the Gaussian correlation function has been used (eq. 26):

$$R(x^i, x^j) = \exp\left(-\sum_{k=1}^N \tau_j |x_k^i - x_k^j|^2\right) \quad (26)$$

where N is the number of parameters, τ_j are the unknown correlation parameters used to fit the model, and x_k^i and x_k^j are the k th components of the sample points x^i and x^j . Correlation parameters τ_j are estimated using the maximum likelihood methodology. The “best” kriging model is found by solving a j -dimensional, unconstrained, nonlinear optimization problem. In this study, the PSO global optimization algorithm has been used to identify kriging parameters.

4.2.4.2 Design of Experiments

The first step in the generation of a surrogate model is to sample the response surface at some specific design sites. This procedure is usually referred to in the literature as the Design

of Experiments (DoEs). As pointed out by Razavi et al. (2012), a sufficiently large and well-distributed set of initial design sites is crucial for a successful application of a metamodeling framework. There are several DoEs methods available in the literature. Factorial design (Gutmann, 2001), Latin Hypercube Sampling (LHS) (McKay et al., 1979), and Symmetric Latin Hypercube Sampling (SLHS) (Ye et al., 2000) are the most commonly used. In this study, the LHS has been used. The size of the DoEs sample is strongly dependent on the complexity of the original response surface and computational budget available. The kriging model requires at least $N+1$ design sites to fit, while additional sites will improve the accuracy of the surrogate. Several relations were proposed in the literature to choose the size p of the initial sample (e.g., Gutmann, 2001; Regis and Shoemaker, 2004). In this study, the relation proposed by Jones et al. (1998) has been used (eq. 27):

$$p = 10N \quad (27)$$

Considering that the number of investigated parameters was 4, 40 sampling points were generated using the LHS.

4.2.4.3 Approximation Uncertainty Framework

The surrogate model fitted on a DoEs sample is only the first approximation of the original response function. Its accuracy can be improved using further original model runs (*infill points*) in addition to the initial sampling plan. The distribution of *infill points* strongly depends on the complexity of the original response surface and on the type of analysis conducted. When the purposes of the analysis of the surrogate model includes uncertainty and sensitivity analyses, it is necessary to have an accurate global approximation of the response surface. The adaptive-recursive framework relies on the assumption that the optimal solution of the surrogate represents well the original model. However, this is not always true, especially when the response surface is characterized by high multimodality. When the approximation of the response surface by the surrogate model is limited, this framework is not recommended for

the uncertainty and/or sensitivity analysis. Jones (2001) concluded that the adaptive-framework is helpful at best for local optimization.

In this study, the approximation uncertainty framework was applied to address the shortcoming of the adaptive-recursive framework, which considers uncertainties associated with the approximation. RSS, such as kriging, explicitly provide a measure of uncertainty since they treat the deterministic response of a computer simulation as the realization of a stochastic process. The model can then be evaluated at points with the highest uncertainty, which can then be included among the design sites. Although globally convergent, such an approach requires an impractically large number of original function evaluations. An effective uncertainty based framework should balance exploitation (i.e., fine tuning of a good solution) and exploration (i.e., reducing the overall uncertainty of the surrogate). The expected-improvement approach (Schonlau, 1997) was used in this study. An expected-improvement is a measure that statistically quantifies the obtained improvement when a given point is evaluated by the original model and added to design sites. For a complete description of the expected-improvement approach please refer to Schonlau (1997).

In this study, the expected-improvement approach was used to add 15 *infill points* to the initial design sites. In order to have good accuracy, the surrogate was refitted after each new original model evaluation (Razavi et al., 2012).

4.2.4.4 Surrogate Validation

Validation of the RSS model is important for evaluating the reliability of the surrogate. Although exact emulators such as kriging exactly interpolate the response surface at design sites, their accuracy in unexplored regions of the parameter space must be evaluated. The validation can be conducted by evaluating the agreement between values of the variable of interest predicted by both the surrogate and original models on an independent set of sample points. Cross validation strategies such as k -fold and leave-one-out cross validation have also

been used in the literature (Wang and Shan, 2007). In the present study, an independent set of sample points was generated using the LHS and used to validate the model. Ten points were used to carry out the validation process. The determination coefficient R^2 was used to assess the agreement between predicted and modeled values. As suggested by Forrester et al. (2008), a value of the correlation coefficient higher than 0.8 indicates a surrogate model with good predictive capabilities.

4.2.5 Global Sensitivity Analysis (GSA)

A sensitivity analysis (SA) can identify the most influential parameters, their interactions, and how these parameters affect the output (Saltelli et al., 2005). Most SAs performed in the literature of environmental sciences are the so-called 'one-at-a-time' (OAT) sensitivity analyses, performed by changing the value of parameters one-at-a-time while keeping the other parameters constant (Cheviron and Coquet, 2009; Houska et al., 2013; Rezaei et al., 2015). However, when the model includes interactions between multiple parameters, results of the OAT analysis are inaccurate because parameter interactions can be globally identified only by simultaneously changing multiple parameters. For this reason, when the property of a model is *a priori* unknown, a Global Sensitivity Analysis (GSA) is always preferred (Saltelli and Annoni, 2010). Practitioners call this analysis a model-free setting, which means that a particular application does not depend on particular assumptions regarding the behavior of the model, such as linearity, monotonicity, etc (Saltelli and Annoni, 2010).

Variance-based methods aim to quantify the amount of variance that each parameter contributes to the unconditional variance of the model output. In Sobol's method, these measures are represented by Sobol's sensitivity indices (SIs). These indices give quantitative information about the variance associated with a single parameter or with interactions of multiple parameters. For a more complete explanation about Sobol's method, please refer to Sobol' (2001). Sobol's sensitivity indices are expressed as follows:

$$\text{First Order } S_i = \frac{V_i}{V} \quad (28)$$

$$\text{Second Order } S_{ij} = \frac{V_{ij}}{V} \quad (29)$$

$$\text{Total } S_T = S_i + \sum_{j \neq i} S_{ij} + \dots \quad (30)$$

where V_i is the variance associated with the i th parameter and V is the total variance. The first-order index, S_i , is denoted in the literature as the “main effect.” When the model is additive, i.e., when it does not include interactions between input factors, the first-order index is sufficient for decomposing the model’s variance. For additive models, the following relation is valid:

$$\sum_i S_i = 1 \quad (31)$$

On the other hand, the total effect index, S_T , gives information about a non-additive part of the model. $S_{Ti} = 0$ is a condition necessary and sufficient for X_i to be non-influential. For an accurate description of the calculation of Sobol’s indices please refer to Saltelli (2010).

When the model is nonlinear, as most environmental models are, Sobol’s indices are calculated using Monte Carlo integrals. Obviously, the accuracy in the estimation of integrals becomes more accurate as the number of samples increases, which also increases the computational cost of the SA. However, this limitation is avoided when using a surrogate model since the computational cost associated with the evaluation of a large number of samples is very low (O’Hagan, 2006; Oakley and O’Hagan, 2004). For this reason, 1000 samples for a total of 30,000 surrogate model runs were used in this study. To sample the parameters’ space we used Sobol’s quasi-random sampling technique (Sobol’, 2001).

In order to assess the accuracy of the estimations of the sensitivity indices, the bootstrap confidence intervals (BCIs) (Efron and Tibshirani, 1986) were estimated. The basic idea of the bootstrapping is that the sample contains all available information about the underlying

distribution. In our particular case, we were interested in computing the uncertainty of estimated sensitivity indices. However, since their distribution is unknown it is not possible to compute the confidence intervals analytically. The rationale of the bootstrap method is to replace the unknown distribution with its empirical distribution and to compute the sensitivity indices using a Monte Carlo simulation approach where samples are generated by resampling the original sample used for the sensitivity analysis. In our case, the samples used for the GSA were sampled 1000 times with replacement, whereby Sobol's indices were calculated for each resampling. In this way, 95% confidence intervals are constructed using the percentile method and the moment method (Archer et al., 1997).

4.2.6 Particle Swarm Optimization

Numerous applications of inverse modeling for the estimation of soil hydraulic properties exist in the literature (Abbaspour et al., 2004; Hopmans et al., 2002; Vrugt et al., 2008, 2004). The gradient methods (Marquardt, 1963) have been most widely used among hydrologists and soil scientists. However, these methods are sensitive to the initial values of optimized parameters and the algorithm often remains trapped in local minima, especially when the response surface exhibits a multimodal behavior. These considerations inspired researchers to develop and use global optimization techniques such as the annealing-simplex method (Pan and Wu, 1998), genetic algorithms (Ines and Droogers, 2002), shuffled complex methods (Vrugt et al., 2003), and ant-colony optimization (Abbaspour et al., 2001), among many others.

In this paper, a global search method based on Particle Swarm Optimization (PSO) (Kennedy and Eberhart, 1995) was used. This method simulates the behavior of a flock of birds collectively foraging for food (i.e., searching for the optimum of the objective function). In their recent study, Brunetti et al. (2016b) used PSO to estimate the soil hydraulic properties of a permeable pavement with satisfactory results. PSO is a relatively new algorithm for evolutionary computation methodology, but its performance has proven to be comparable to various other more established methodologies (Kennedy and Spears, 1998; Shi and Eberhart,

1999). One of the main advantages of PSO is the easiness of its implementation (Liang et al., 2006). A detailed description of the PSO algorithm is given in Shi and Eberhart (1998).

In PSO, each particle represents a possible solution of the problem. First, particles are placed in the search space, each characterized by a particular value of the objective function. Each particle then changes its position after exchanging information about its own current and best positions with other members of the swarm. The next iteration starts after all particles have changed their positions. The most important parameters in the PSO are c_1 , c_2 , and w . c_1 and c_2 are constant parameters known as the cognitive and social parameters, respectively, which drive the search behavior of the algorithm. Depending on the values of c_1 and c_2 the PSO can be more or less “responsive”. However, their values should be selected carefully because large values of these parameters can lead to instabilities in the algorithm. w is the inertia-weight, which plays a key role in the optimization process by providing balance between exploration and exploitation. In PSO, each particle is influenced by its nearest neighbors. The arrangement of neighbors that influence a particle is called the *topology* of the swarm. Different types of neighborhoods are reported in the literature (Akat and Gazi, 2008). In this study, the *all* topology is used, in which the neighborhood encompasses the entire swarm. The PSO parameters used in this study for both scenarios are reported in Table 4.2 and are as suggested by Pedersen (2010).

Table 4.2 Parameters used in the PSO optimization.

| <i>Swarm size</i> | c_1 | c_2 | w |
|-------------------|-------|-------|-------|
| 63 | -0.73 | 2.02 | -0.36 |

4.2.7 Objective Function

The Nash-Sutcliffe Efficiency (NSE) index (J E Nash and Sutcliffe, 1970) was used to evaluate the agreement between measured and modeled hydrographs and as the variable of interest in the surrogate analysis:

$$NSE = 1 - \left[\frac{\sum_{i=1}^T (Q_i^{obs} - Q_i^{mod})^2}{\sum_{i=1}^T (Q_i^{obs} - Q_{mean}^{obs})^2} \right] \quad (32)$$

where Q_i^{obs} is the i th measured value, Q_i^{mod} is the i th simulated value, and Q_{mean}^{obs} is the mean value of observed data. The NSE index ranges between $-\infty$ and 1.0, is equal to 1 in case of perfect agreement, and generally, values between 0.0 and 1.0 are considered acceptable (Moriasi et al., 2007). The NSE index was used because it is often reported to be a valid measure for evaluating the overall fit of a hydrograph (Sevat et al., 1991).

It is important to emphasize that subsurface outflow from a LID system is among the most important outputs in the analysis of urban drainage systems. In our case, the stormwater filter was impervious at the bottom and hydraulically connected with the sewer system. An accurate numerical reconstruction of the subsurface hydrograph is thus fundamental in order to quantify its effect on the drainage system.

4.3 Results and Discussion

4.3.1 Evaporation Method

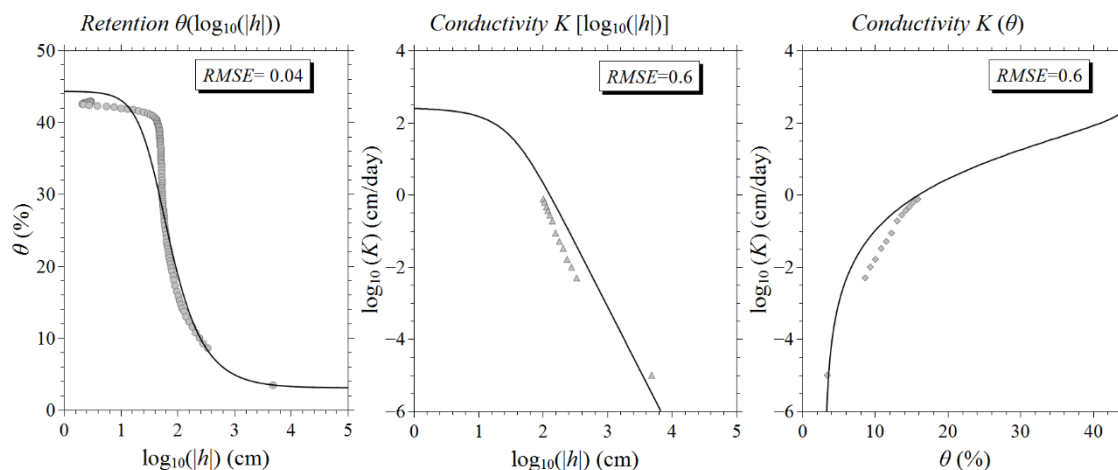


Figure 4.4 Measured values and modeled functions of soil water retention, $\theta(\log_{10}(|h|))$ (left) and the unsaturated hydraulic conductivity, $K(\log_{10}(|h|))$ (center) and $K(\theta)$ (right). Symbols represent the measured values, and full lines the fitted VGM functions.

Soil hydraulic properties measured using the evaporation method are displayed in Figure 4.4. The retention data point close to $\log(|h|)=4$ (h in cm) was obtained by using the air-entry pressure head of the ceramic cup of the tensiometers. Measured retention points were not available in the very dry range, between 2.7 and 3.8, since cavitation occurred in the tensiometers. The behavior of the retention curve appears to be sigmoidal and characterized by a clearly identifiable air-entry pressure head at $\log(|h|)=2$ (h in cm). Below this pressure head, the soil quickly desaturated, indicating a narrow pore-size distribution. Measured points of the hydraulic conductivity function were sparser and concentrated in the dry range between volumetric water contents of 0.10 and 0.20. The measured soil porosity and bulk density were 0.44 and 1.59 g/cm³, respectively.

The unimodal van Genuchten-Mualem model (van Genuchten, 1980) was fitted to measured points using the HYPROP-FIT software. The *RMSE* values for retention and conductivity functions were 0.04 (cm³cm⁻³) and 0.6 (in log K , cm/day), respectively. The VGM

function (full lines in Fig. 4.4) described the retention data well, especially in the dry and medium-wet regions (volumetric water contents of 0.05-0.3), while it introduced some bias near saturation where it poorly described the sharp increase in water retention at the air-entry pressure head. However, the low *RMSE* value was considered acceptable for the purposes of the present study. The *RMSE* value for the hydraulic conductivity was higher, indicating a slightly worse performance of the VGM function in describing the hydraulic conductivity of the substrate. The estimated soil hydraulic parameters (reported with their confidence intervals in Table 4.3) were used in HYDRUS-2D to model the hydraulic behavior of the soil substrate.

Table 4.3 Estimated soil hydraulic parameters and their confidence intervals for the soil substrate

| Parameter | 2.5% | Estimated value | 97.5% |
|------------------------------|-------|-----------------|-------|
| $\theta_r (-)$ | 0.02 | 0.03 | 0.04 |
| $\theta_s (-)$ | 0.43 | 0.44 | 0.45 |
| $\alpha (1/\text{cm})$ | 0.021 | 0.025 | 0.029 |
| $n (-)$ | 1.84 | 1.97 | 2.10 |
| $K_s (\text{cm}/\text{day})$ | 200 | 260 | 320 |
| $L (-)$ | -0.63 | -0.44 | -0.25 |

4.3.2 Kriging Approximation of the Response Surface

The DoEs sample, generated with the LHS technique, was used to build the first approximation of the response surface for the investigated soil hydraulic parameters. First, the HYDRUS-2D model was executed 40 times (Eq. 27), and the *NSE* index was computed for each run and stored in a 1D array. A single run of the original HYDRUS-2D model required almost 1 minute of CPU time on a laptop equipped with a CPU Intel® Core i7-4700 MQ 2.40 GHz processor and 8 GB of RAM. Next, the LHS sample and the *NSE* array were used in the PSO optimization framework to estimate the kriging parameters. To check its accuracy, the

obtained kriging model was validated on another independent sample generated with the LHS. As shown in Figure 4.5, the validation sample covered values of NSE ranging from 0.2 to 0.8, providing information about the response surface for both less and more accurate portions of the parameters space.

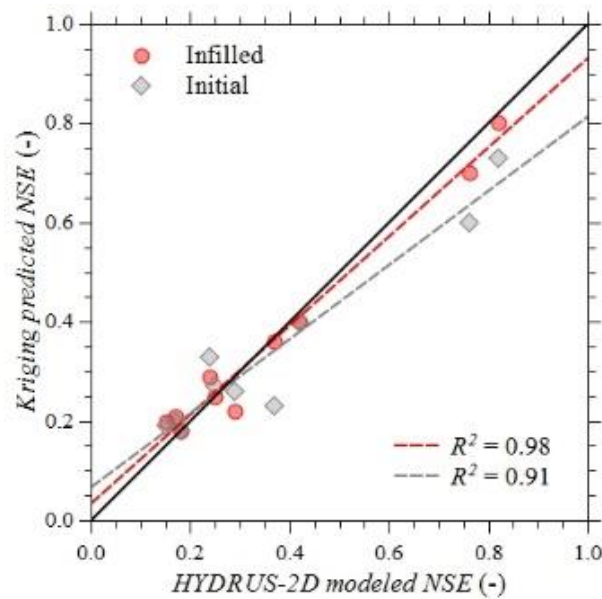


Figure 4.5 Comparison between the HYDRUS-2D and kriging-predicted values of the NSE for the validation sample. The initial (grey diamonds) and infilled (red circles) kriging models are compared. A bisector (a black line) and regression lines for the initial (a dashed grey line) and infilled (a dashed red line) kriging models are reported.

At the first inspection, the kriging model based on the initial sample exhibited a moderate accuracy. The determination coefficient R^2 for the initial kriging model was 0.91, which already indicated an overall accuracy of the surrogate model (Forrester et al., 2008). This confirmed the good coverage of the DoEs sample. However, as shown in Figure 4.5, the surrogate, while being highly accurate for low values of the objective function, introduced a significant bias for high values of NSE , which are those of interest in an optimization

framework. The regression line for the initial surrogate (a dashed gray line in Fig. 4.5) almost overlapped the bisector (a black line in Fig. 4.5), which indicates a perfect agreement between the surrogate and the original model in the range of 0.2-0.4, while it underestimated values of the response surface in the region around 0.8. The underestimation of the response surface values in the region where optimal parameter values are likely located could influence the next surrogate-based optimization of soil hydraulic properties.

To increase the accuracy of the kriging model, the approximation uncertainty framework was used next. As described in the methodology section, 15 *infilled* points were added to the initial design sites using the expected improvement approach. As shown in Figure 4.5 and as expected, the infilled kriging model outperformed the initial kriging model. The determination coefficient R^2 increased to 0.98, indicating that the infilled kriging improved the description of the response surface. This behavior was confirmed by the regression line (a dashed red line in Fig. 4.5), which almost overlapped a bisector line. Moreover, the accuracy of the kriging model improved for high values of NSE , which are those of interest in an optimization process, while remaining similarly high for low values of NSE . This global accuracy of the surrogate is fundamental for the GSA, which explores the response surface landscape. No additional points were added to the design sites considering the relatively high accuracy of the surrogate, and the final surrogate was used for the GSA and optimization.

4.3.3 Global Sensitivity Analysis

The validated kriging model was next used in the GSA. Sobol's sensitivity indices, with their confidence intervals for each parameter, are reported in Table 4.4.

Table 4.4 The first-order (S_1) and total (S_T) effect indices (in a decreasing order) with their bootstrap confidence intervals (BCI) for the soil hydraulic parameters.

| Parameter | S_1 | S_1 (BCI) | S_T | S_T (BCI) |
|------------------|-------------------------|-------------------------------|-------------------------|-------------------------------|
| α [1/cm] | 0.93 | 0.24 | 0.94 | 0.05 |
| K_s [cm/min] | 0.04 | 0.08 | 0.05 | 0.007 |
| n [-] | 0.01 | 0.02 | 0.008 | 0.001 |
| θ_s [-] | 0.002 | 0.01 | 0.001 | 0.001 |
| Sum | ≈ 1.0 | | ≈ 1.0 | |

The sensitivity analysis revealed that the model was additive. This was confirmed by the sum of the first-order indices, which was almost 1, and by negligible differences between the first-order and total-effect indices for each parameter. An additive model $Y=f(X_1, X_2, \dots, X_N)$ can be decomposed into a sum of N functions, where N is the number of parameters. This means that the effects of interactions between model parameters on model results were negligible.

As shown in Table 4.4, the most influential parameter was the shape parameter α . Its first-order (S_1) and total effect (S_T) indices were more than an order of magnitude higher than corresponding indices for the second most influential parameter K_s . The pore-size distribution index n and the saturated water content θ_s exhibited the lowest sensitivity, indicating their marginal role on the output's variance. Moreover, since their total effects were almost zero, these parameters can be fixed to any feasible value in the parameter space without affecting the value of the objective function, reducing the dimensionality of the inverse problem to only two parameters, α and K_s . Such results are very useful in an optimization framework, since they can simplify the parameter estimation procedure. Some of the total effect indices were only slightly larger than the first order indices. This is mainly due to approximation in the numerical integration of the total unconditional variance (Sobol', 2001).

It must be emphasized that additivity is quite unusual for environmental models, which are generally characterized by high nonlinearity and interactions between parameters (Brunetti

et al., 2016a; Nossent et al., 2011). In our particular case, the dominant effect of the α parameter on the hydrograph makes it difficult to identify interactions between parameters. This may also indicate that water flow in the filter layer deviates from the traditional Darcian behavior and involves other physical processes, such as preferential and film flows. In such circumstances, some parameters can exhibit a negligible effect on the model's response.

As mentioned in the methodology section, the GSA required 30,000 evaluations of the surrogate model. The computational cost of the kriging-based sensitivity analysis was limited to 1-2 seconds on a laptop equipped with a CPU Intel® Core i7-4700 MQ 2.40 GHz processor and 8 GB of RAM. On the other hand, since a single HYDRUS-2D model run required approximately 1 minute, the same type of GSA performed using the original HYDRUS-2D model would have required approximately 21 days of continuous computation. This clearly represents one of the main advantages of surrogate-based modeling: performing the same type of analysis with negligible computation time and a similarly good level of accuracy.

4.3.4 Kriging-Based Optimization

Using the results of the GSA, only shape parameter α and the saturated hydraulic conductivity K_s were optimized. The saturated water content θ_s and the pore-size distribution index n were assumed to be 0.15 and 3.2, respectively, considering that the filter layer consisted of coarse gravel, usually characterized by reduced porosity and narrow pore-size distribution. The soil hydraulic parameters of the filter layer, including the optimized parameters, are summarized in Table 4.5. The filter layer exhibited both a high value of the saturated hydraulic conductivity K_s (90 cm/min) and a very low value of the shape parameter α (0.001 1/cm).

The estimated parameters indicated that the hydraulic behavior of the filter layer was characterized by high flow rates and negligible retention capacity, which are both typical for coarse textured media. The optimized parameter values are similar to those reported in Brunetti et al. (2016b) for the base layer of a permeable pavement. In that study, the base layer consisted

of crushed stones and was modeled using either the classical VGM function or the dual-porosity approach to account for preferential flow. Specifically, for the unimodal VGM function, the authors reported a value of 0.023 1/cm for the shape parameter α and a saturated hydraulic conductivity K_s of 68.7 cm/min. Moreover, the plausible occurrence of film flow in the filter layer, which can support very high flow rates, especially at near-zero matrix potential (Tokunaga, 2009), needs to be contemplated. Under such circumstances, the hydraulic behavior of the material tends to deviate from the typical Richard's type flow, and the optimized parameters attempt to approximate a combination of fingering and film flow that likely occur in this layer.

Table 4.5 VGM parameters for the filter layer. The shape parameter α and the saturated hydraulic conductivity K_s were estimated using the PSO algorithm.

| Soil hydraulic parameters | | | | | | |
|---------------------------|----------------|----------------|-----------------|---------|----------------|---------|
| Layer | θ_r (-) | θ_s (-) | α (1/cm) | n (-) | K_s (cm/min) | L (-) |
| Filter | 0 | 0.15 | 0.001 | 3.2 | 90 | 0.5 |

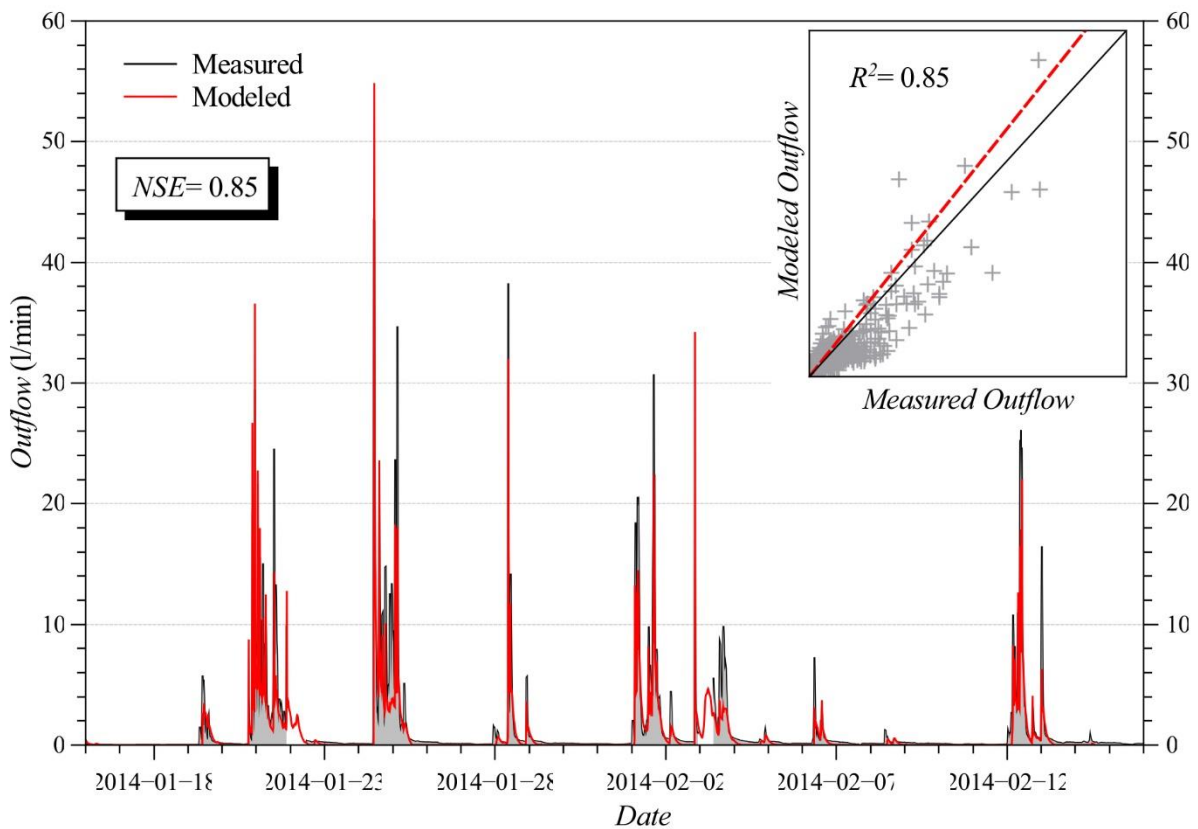


Figure 4.6 A comparison between measured and simulated outflows versus time and against each other (in the insert) for the calibration period. The full and dashed lines in the insert are a bisector and linear regression line, respectively.

Figure 4.6 shows a comparison between the measured and modelled hydrographs for the optimization period. The PSO resulted in the *NSE* value of 0.85, which confirmed the accuracy of the measured and estimated parameters. As reported by Moriasi et al. (2007), values of *NSE* between 0.75 and 1.0 indicate a very good agreement between hydrographs, and an adequate model calibration. The model was able to correctly reproduce the fast hydraulic response of the hydrograph during precipitations and to reasonably estimate peak flows. The insert of Figure 6 shows the simulated against measured SF outflows. The same plot also shows a bisector line, which indicates a perfect agreement between simulated and measured outflows,

and a linear regression line. The good performance of the model is confirmed by the determination coefficient $R^2=0.85$. The comparison between the bisector and regression lines indicates that, in general, the model slightly overestimated the outflow.

A careful inspection of simulated fluxes revealed that the model tends to underestimate low flows (Fig. 4.6). This behavior could be related to the coarse nature of the filter layer, which closely resembles “fractured aquifers”. Typical breakthrough curves for fractured aquifers are characterized by early breakthrough and long tailing (Geiger et al., 2010). This is due to a delayed response in the matrix to pressure head changes that occur in the surrounding fractures. Brattebo and Booth (2003), Brunetti et al. (2016b), and Fassman and Blackburn (2010) observed a similar behavior in permeable pavements, the base and sub-base layers of which are composed of crushed stones. In such circumstances, more complex models are needed to simultaneously describe fast preferential flow and the matrix-fracture interactions in the filter layer (Brunetti et al., 2016a).

Since the computational time associated with a single surrogate model evaluation was negligible, the approximate response surface was investigated. Figure 4.7 shows the α - K_s response surface obtained using a regular grid of 40,000 points. The darkest areas represent regions of the parameter space with high values of NSE . At the first inspection, the response surface was not characterized by multimodality. As shown in Figure 4.7, optimal solutions were concentrated in the left part of the plot for values of α between 0.001 and 0.05. For α values larger than 0.05, the objective function dropped quickly to 0.3-0.4. The NSE values slowly increased for values of $\alpha > 0.2$. This can be expected since the α parameter for gravels usually has relatively high values. However, in our case, high values of α were not able to accurately reproduce the hydraulic behavior of the SF. On the other hand, the response surface exhibited limited variability in the K_s direction, since high values of NSE were guaranteed for a broad range of saturated hydraulic conductivity values.

These results confirmed the findings of the GSA, which clearly indicated that the variance of the objective function was mainly driven by the shape parameter α , with only a limited influence of K_s . This behavior is shown in detail in Figure 4.8.

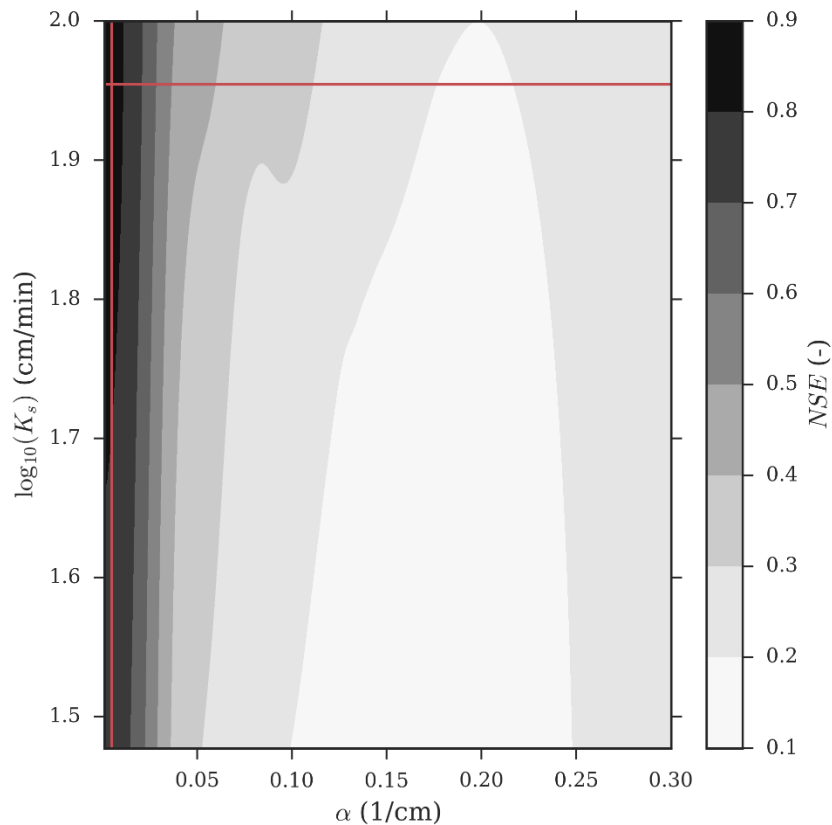


Figure 4.7 The $\alpha - K_s$ response surface obtained using a regular grid of 40,000 points. The red lines indicate the cross sections reported in Figure 4.8.

Figure 4.8 shows horizontal ($K_s = 90$ cm/min) and vertical ($\alpha = 0.001$ 1/cm) cross-sections (red lines in Fig. 4.7) through the response surface. Yellow rectangular areas are expanded in the right part of the plot. With respect to K_s , the optimum was not clearly identifiable at the first inspection. The values of the objective function ranged between 0.8 and

0.85 in the entire range of the saturated hydraulic conductivity, indicating its limited effect on the response surface. The area around the PSO-optimized value of K_s (90 cm/min) is expanded in the bottom-right corner of Figure 4.8. From this plot, it is evident how the PSO algorithm well identified the optimal value K_s , even for a flat profile.

Conversely, Figure 4.8 shows a completely different behavior for the α - NSE profile, for which an optimal region was identified in the left part of the plot for low values of the α parameter. While the gradient of the curve seemed to approach a maximum, it was not possible to clearly identify the optimum, which may have been outside of the range imposed on the α parameter. As previously discussed, this behavior could be related to a deviation from the Darcian flow in the filter layer. The further analyzes of the response surface indicated that values of α over 0.01 1/cm corresponded to a marked decrease of NSE . This is evident from the expanded area in the top-right corner of Figure 4.8. This finding is in agreement with the results of the GSA, which identified α as the most influential parameter.

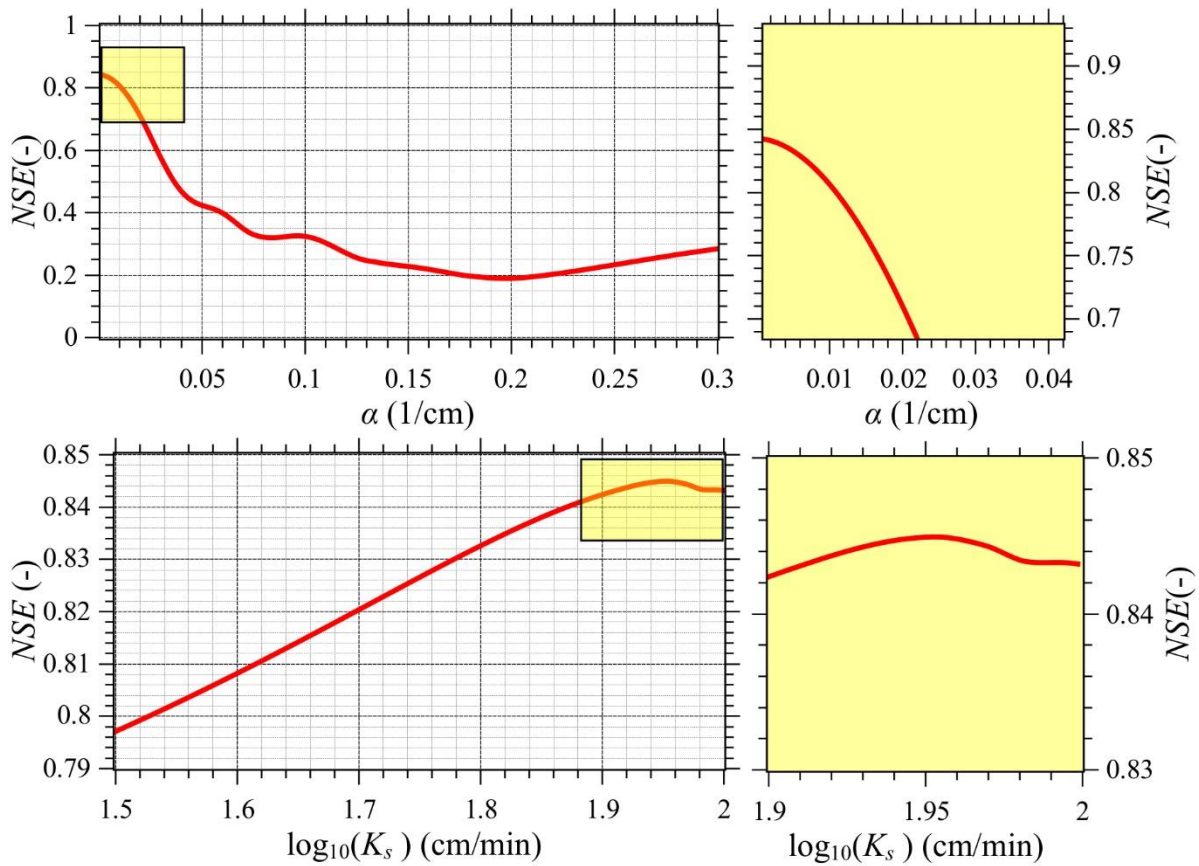


Figure 4.8 Horizontal [$K_s = 90$ cm/min] (top), and vertical [$\alpha = 0.001$ 1/cm] (bottom) response surface cross-sections. The yellow rectangular areas for both plots are expanded on the right.

In order to verify whether additional soil hydraulic parameters, such as the saturated water content θ_s and the pore-size distribution index n , influenced the optimum, a surrogate-based optimization, which considered four soil hydraulic parameters was carried out. The results of the optimization are listed in Table 4.6.

Table 4.6 VGM parameters for the filter layer. The saturated water content θ_s , the shape parameters α and n , and the saturated hydraulic conductivity K_s were estimated using the PSO algorithm.

| Soil hydraulic parameters | | | | | | |
|---------------------------|----------------|----------------|-----------------|---------|----------------|---------|
| Layer | θ_r (-) | θ_s (-) | α (1/cm) | n (-) | K_s (cm/min) | l (-) |
| Filter | 0 | 0.17 | 0.003 | 3.1 | 89 | 0.5 |

As shown in Table 4.6, the newly estimated parameters are very similar to those estimated when θ_s and n were fixed. The saturated water content was 0.17, which is slightly higher than the previously fixed value. Conversely, the pore-size distribution index n was slightly lower, but the difference was again very small. The two most sensitive parameters α and K_s had some small changes, however overall results are in a good agreement with those reported previously. Again, the filter layer exhibited a relatively high permeability and a low value of the α parameter. These numerical differences could be related to the effects of interactions between parameters, which, even if small in magnitude as demonstrated by the GSA, can affect the optimization process.

4.3.5 Model Validation

In order to evaluate the reliability of the estimated parameters, the model was validated using another independent set of experimental data. Figure 4.9 shows a comparison between measured and modeled hydrographs during the validation period.

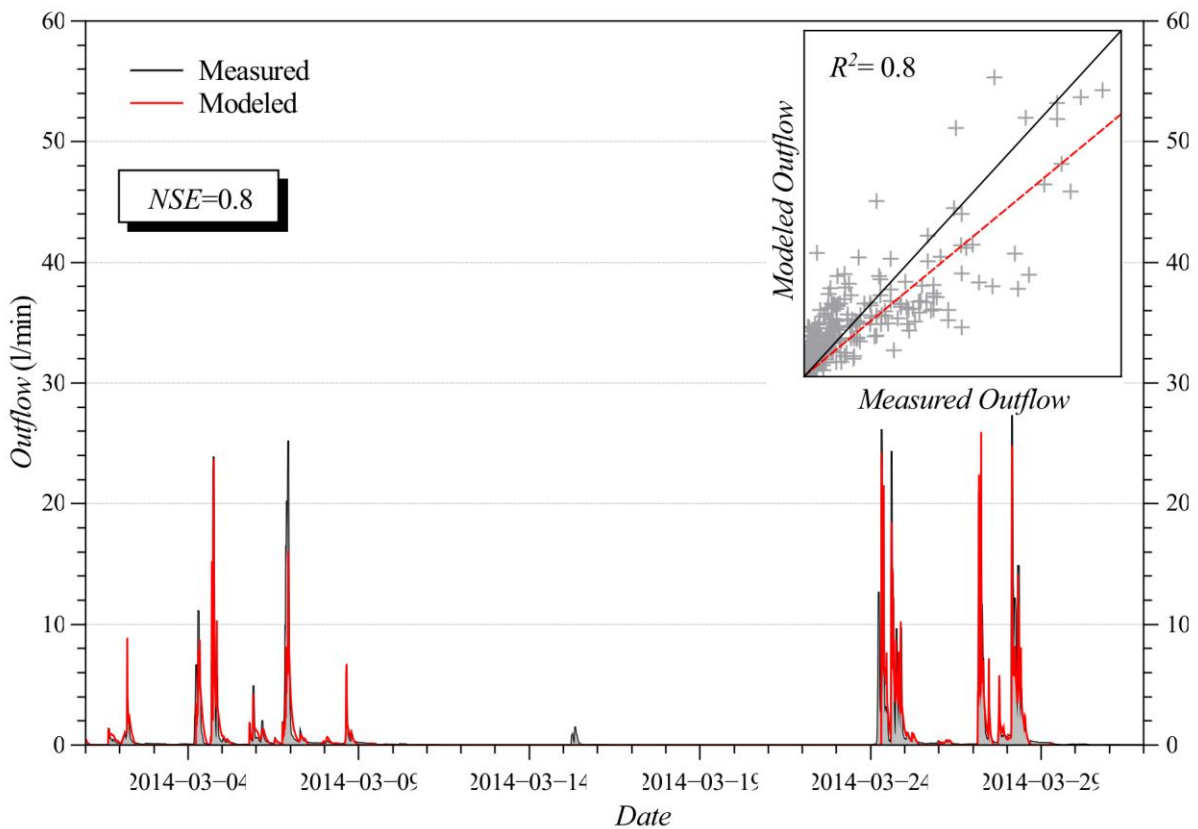


Figure 4.9 A comparison between measured and simulated outflows versus time and against each other (in the insert) during the validation period. The full and dashed lines in the insert are a bisector and linear regression line, respectively.

The value of the objective function was $NSE = 0.8$, which again confirmed the adequacy of the estimated parameters. The description of the hydraulic behavior of the stormwater filter during rainfall events was satisfactory. This capability of the calibrated model to correctly describe the hydraulic behavior of the system is important when dealing with the analysis of combined traditional drainage systems and LID techniques. A correct description of the hydrograph during precipitation events gives information about the lag time and the intensity of peak flow, which are fundamental for both a comprehensive hydraulic analysis of drainage systems, and for the evaluation of benefits of LIDs implementations. The model was not able

to reproduce outflow induced by the precipitation event on March 15. This may be related to an overestimation of actual evapotranspiration calculated using values from the literature for albedo, LAI, and a hypothetical roots distribution, which could result in an overestimation of the storage capacity of the SF at the beginning of the precipitation event, which had a total volume of 6 mm. As a result, the model predicted that the SF retained all the precipitation volume. A better characterization of evapotranspiration could help in increasing the accuracy of the model, which was already high.

4.4 Conclusions and Summary

The aim of this study was to demonstrate the benefit of surrogate-based modeling in the numerical analysis of Low Impact Development techniques. In particular, the unsaturated hydraulic properties of a contained stormwater filter installed at the University of Calabria were evaluated in the study. The kriging technique was used to approximate the deterministic response of the widely used mechanistic model HYDRUS-2D, which was used to simulate the variably-saturated hydraulic behavior of the filter. In order to reduce the dimensionality of the inverse problem, the simplified evaporation method was used to determine the unsaturated soil hydraulic properties of the soil substrate placed on the top of the filter layer. The Nash-Sutcliffe efficiency index was used both to compare the simulated and measured outflows, and as the variable of interest for the construction of the response surface.

The PSO heuristic algorithm was used to estimate the kriging parameters based on an initial set of design sites obtained using Latin Hypercube Sampling. The approximation uncertainty framework improved the accuracy of the surrogate model by using the expected-improvement approach to select additional points to the initial design sites. The kriging model was validated against an unexplored set of points with satisfactory results. The obtained surrogate was then used to perform a global sensitivity analysis of the hydraulic parameters of

the filter layer based on Sobol's method, with a negligible computational cost. The sensitivity analysis revealed that the model is additive, and that only two soil hydraulic parameters, the shape parameter α and the saturated hydraulic conductivity K_s , affect the hydraulic response of the filter layer. These two parameters were estimated using the PSO algorithm with a *NSE* value of 0.85, which indicated a good accuracy of the model. Moreover, the analysis of the response surface confirmed the results of the GSA, identifying α as the most influential parameter. The reliability of the surrogate-based analysis was evaluated by validating the optimized parameters on an independent dataset of measured outflows. A *NSE* value of 0.8 confirmed the reliability of the HYDRUS-2D model calibrated using the kriging technique.

While the accuracy of mechanistic models is not in doubt, one of the most widespread criticism against their use is their computational cost, which limits their adoption. This study has demonstrated how a surrogate-based analysis can provide an effective solution in overcoming this limitation. In this paper, the kriging technique was used for highly expensive computational analyses, such as the GSA and the PSO, with good results.

This novel study represents the first contribution towards the use of surrogates for LIDs analysis, which does not need to be limited only to the investigation of soil hydraulic properties. For example, potential applications can be also targeted to the optimization of the morphological characteristics of the LID itself (depth, slope, plants, etc) for a particular climate, to the optimization of the adsorption properties of filter layers, or for specific design aims. Such studies could help in providing a better understanding of LID techniques while promoting the widespread adoption of such systems.

Chapter 5 Conclusions and future directions

The main aim of this thesis was to investigate the use of mechanistic modelling for the numerical analysis of LIDs. The benefits and the limitations of mechanistic modelling were analysed in a comprehensive perspective to give a new contribution to the scientific community. The work included the application of numerical algorithms and laboratory techniques, which are rather new for urban hydrology. Three field-scale experimental facilities were used as case studies to investigate the use of mechanistic models.

In Chapter 2, a mechanistic model was used to simulate the hydraulic/hydrologic behaviour of an extensive green roof. The numerical analysis included precipitation, drip irrigation, evaporation, transpiration, and infiltration. The combined morphological and hydrological complexity of the green roof required the application of a three-dimensional model. The Finite-Element software HYDRUS-3D has been used. The variably-saturated hydraulic behaviour of the green roof was described by solving numerically the Richards equation. Before simulation started, the soil water retention curve and the unsaturated hydraulic conductivity of the substrate were determined in the laboratory using the simplified evaporative method. Measured soil hydraulic properties highlighted the highly conductive behaviour of the substrate, which also exhibited a slightly bimodality in the pore-size distribution. The widely recognized unimodal and bimodal van Genuchten-Mualem relations were used to parameterize the substrate hydraulic properties, and then used in the numerical model. A two month-long period was simulated and validated against experimental data using the Nash-Sutcliffe efficiency index. Both the unimodal and bimodal model exhibited satisfactory values of the NSE, 0.74 and 0.8 respectively. The bimodal model produced better results, as it was able to accurately reproduce the hydraulic behaviour of the green roof under precipitations and

irrigation. The validated model was used to investigate different aspects of the hydraulic behaviour of the green roof. The hydrological performance of the green roof were analysed during the entire simulation period as well as at event scale, and linked to the dynamics of water contents and actual evapotranspiration. This application demonstrated how a mechanistic model can simultaneously handle the complexity and give extremely useful information about the hydraulic behaviour of a green roof.

In Chapter 3, a mechanistic model was used to simulate the hydraulic behaviour of a permeable pavement. In contrast to green roof, the morphological and hydrological homogeneity allowed the used of one-dimensional model. However, the main difficulty resided in the accurate determination of soil hydraulic parameters for all the four different layers forming the pavement. Two different scenarios of describing the hydraulic behaviour of the permeable pavement system were analysed: the first one uses a single porosity model for all layers of the permeable pavement; the second one uses a dual-porosity model for the base and sub-base layers. The choice to use the dual-porosity model was made in order to investigate the possibility of preferential flows in the lower layers, which were hydraulically compared to fractured aquifers. In such circumstances, the two scenarios included 16 and 20 unknown parameters respectively. A Global Sensitivity Analysis followed by a Monte Carlo filtering highlighted the influence of the wear layer on the hydraulic behaviour of the pavement and identified the ranges of parameters generating behavioural solutions. Reduced ranges were then used in the calibration procedure conducted with the metaheuristic Particle swarm optimization (PSO) algorithm for the estimation of hydraulic parameters. The best fit value for the first scenario was $NSE = 0.43$; for the second scenario, it was $NSE = 0.81$, indicating that the dual-porosity approach is more appropriate for describing the variably-saturated flow in the base and sub-base layers. Estimated parameters were validated using an independent, month-long set of measurements, resulting in NSE values of 0.43 and 0.86 for the first and second scenarios, respectively. The improvement in correspondence between measured and modeled hydrographs confirmed the reliability of the combination of GSA and PSO in dealing with highly dimensional optimization problems. Obtained results have demonstrated that PSO, due

to its easiness of implementation and effectiveness, can represent a new and viable alternative to traditional optimization algorithms for the inverse estimation of unsaturated hydraulic properties. It must be highlighted that both the sensitivity analysis and the PSO required thousands of model runs. While, in this particular case, the model execution was fast, mechanistic models are usually computationally expensive, making it impractical to perform Monte Carlo analysis and global optimizations.

In Chapter 4, the issue related to computational cost of mechanistic model was investigated and addressed. The two-dimensional mechanistic model HYDRUS-2D was used to simulate the hydraulic behaviour of a stormwater filter. This application represented a middle ground between the previous ones. The application was focused on the calibration of a computationally intensive mechanistic model. To address the problem and give a new contribution in this direction, the surrogate-based modelling technique has been used. Surrogate modelling is focused on developing and using a computationally inexpensive surrogate of the original model. While having been previously applied to various water related and environmental modelling problems, no studies have used surrogate models for the analysis of LIDs. The aim of this research thus was to investigate the benefit of surrogate-based modelling in the numerical analysis of LIDs. The kriging technique was used to approximate the deterministic response of the widely used mechanistic model HYDRUS-2D, which was employed to simulate the variably-saturated hydraulic behavior of a contained stormwater filter. The Nash-Sutcliffe efficiency (NSE) index was used to compare the simulated and measured outflows and as the variable of interest for the construction of the response surface. The validated kriging model was first used to carry out a Global Sensitivity Analysis of the unknown soil hydraulic parameters of the filter layer, revealing that only the shape parameter α and the saturated hydraulic conductivity K_s significantly affected the model response. Next, the Particle Swarm Optimization algorithm was used to estimate their values. The NSE value of 0.85 indicated a high accuracy of estimated parameters. Finally, the calibrated model was validated against an independent set of measured outflows with a NSE value of 0.8, which again corroborated the reliability of the surrogate-based optimized parameters. This application

demonstrated how to address the problem of computational cost associated with mechanistic modelling of LIDs.

As highlighted in the Introduction section, the lack of different types of measurements has been a common issue of all modeling scenarios. Only inflows and outflows were available to calibrate and/or validate models. To address this issue, a combination of advanced numerical techniques and laboratory tests has been used. The soil hydraulic properties of the green roof's substrate have been measured in the laboratory using the evaporation method thus avoiding the need to optimize soil hydraulic properties against measured outflow. The same methodology has been used to reduce the dimensionality of the inverse problem addressed in the stormwater filter modeling. In that case, the evaporation method has been used to measure the soil hydraulic properties of the soil substrate thus reducing to four the number of parameters to be optimized against the measured outflow. Conversely, the Global Sensitivity Analysis has been used to gain important information about the hydraulic behaviour of the permeable pavement, identifying most influential parameters. Furthermore, results of the GSA were used to reduce the parameters hyperspace thus improving the convergence of the PSO.

Summarizing, the present thesis demonstrated how mechanistic models represent a valid tool for the numerical analysis of LIDs. The combination of modern laboratory techniques and new numerical algorithms can help in obtaining accurate, reliable and computationally efficient mechanistic models, which offer undoubted benefits against traditional empirical and conceptual models. The widespread adoption of such models among practitioners is the key to boost the diffusion of LIDs in urban areas. A diffusion needed for a *sustainable* development of our cities.

5.1 Future directions

This thesis was not intended as an autoreferential and conclusive act, but on the contrary as an intermediate step towards new and more effective applications of LIDs modeling.

Merging concepts and techniques of other scientific fields is the key to succeed. Surrogate-modeling, a technique of machine learning, is an example. In this study, it has been used to optimize parameters, but it must be not limited to that. For example, potential applications can be also targeted to the optimization of the morphological characteristics of the LID itself (depth, slope, plants, etc) for a particular climate, to the optimization of the adsorption properties of filter layers, or for specific design aims, similarly to what it's done in aeronautical engineering. In this view, Model Order Reduction techniques represent a rather new and effective alternative.

The inclusion of different types of measurements, such as volumetric water content and/or pressure head inside LIDs, could help in reducing the uncertainty in the estimated parameters and facilitate the calibration of mechanistic models for LIDs. In this view, the use of independent measurements of hydraulic properties could increase the reliability of mechanistic models in accurately describing the hydraulic behaviour of LIDs.

Other potential applications of mechanistic models for LIDs can include the simulation of solute transport. Mineralization of organic matter in green roofs, inorganic contaminants transport in permeable pavements, and colloids transport in bioretention cells are just examples. A deep knowledge of these processes, not limited to empirical relations, can help in maximizing the efficiency of LIDs by exploiting the most modern numerical techniques.

References

- Abbaspour, K.C., Johnson, C.A., van Genuchten, M.T., 2004. Estimating Uncertain Flow and Transport Parameters Using a Sequential Uncertainty Fitting Procedure. *Vadose Zo. J.* 3, 1340–1352. doi:10.2113/3.4.1340
- Abbaspour, K.C., Schulin, R., van Genuchten, M.T., 2001. Estimating unsaturated soil hydraulic parameters using ant colony optimization. *Adv. Water Resour.* 24, 827–841. doi:10.1016/S0309-1708(01)00018-5
- Abu-Zreig, M., Rudra, R.P., Whiteley, H.R., 2001. Validation of a vegetated filter strip model (VFSMOD). *Hydrol. Process.* 15, 729–742. doi:10.1002/hyp.101
- Akat, S.B., Gazi, V., 2008. Particle swarm optimization with dynamic neighborhood topology: Three neighborhood strategies and preliminary results, in: 2008 IEEE Swarm Intelligence Symposium. pp. 1–8. doi:10.1109/SIS.2008.4668298
- Allen, R.G., Pereira, L.S., Raes, D., Smith, M., 1998. FAO Irrigation and Drainage Paper No. 56: Crop Evapotranspiration, FAO. Rome.
- Archer, G.E.B., Saltelli, A., Sobol, I.M., 1997. Sensitivity measures, anova-like Techniques and the use of bootstrap. *J. Stat. Comput. Simul.* 58, 99–120. doi:10.1080/00949659708811825
- Arya, L.M., 2002. Wind and hot-air methods, in: Dane, J., G.C., T. (Eds.), *Methods of Soil Analysis. Part 4. Physical Methods.* SSSA, Madison, WI, pp. 916–926.
- Bai, M., Ma, Q., Roegiers, J.-C., 1994. A nonlinear dual-porosity model. *Appl. Math. Model.*

18, 602–610. doi:10.1016/0307-904X(94)90318-2

Barenblatt, G., Zheltov, I., Kochina, I., 1960. Basic concepts in the theory of seepage of homogeneous liquids in fissured rocks [strata]. *J. Appl. Math. Mech.* 24, 1286–1303. doi:10.1016/0021-8928(60)90107-6

Bengtsson, L., Grahn, L., Olsson, J., 2004. Hydrological function of a thin extensive green roof in southern Sweden. *Nord. Hydrol.* 36, 259–268.

Berardi, U., GhaffarianHoseini, A., GhaffarianHoseini, A., 2014. State-of-the-art analysis of the environmental benefits of green roofs. *Appl. Energy* 115, 411–428. doi:10.1016/j.apenergy.2013.10.047

Beven, K., 2006. A manifesto for the equifinality thesis. *J. Hydrol.* 320, 18–36. doi:10.1016/j.jhydrol.2005.07.007

Beven, K., Binley, A., 1992. The future of distributed models: Model calibration and uncertainty prediction. *Hydrol. Process.* 6, 279–298. doi:10.1002/hyp.3360060305

Blanusa, T., Vaz Monteiro, M.M., Fantozzi, F., Vysini, E., Li, Y., Cameron, R.W.F., 2013. Alternatives to Sedum on green roofs: Can broad leaf perennial plants offer better “cooling service”? *Build. Environ.* 59, 99–106. doi:10.1016/j.buildenv.2012.08.011

Borgonovo, E., Castaings, W., Tarantola, S., 2012. Model emulation and moment-independent sensitivity analysis: An application to environmental modelling. *Environ. Model. Softw.* 34, 105–115. doi:10.1016/j.envsoft.2011.06.006

Brattebo, B.O., Booth, D.B., 2003. Long-term stormwater quantity and quality performance of permeable pavement systems. *Water Res.* 37, 4369–76. doi:10.1016/S0043-1354(03)00410-X

Breshears, D.D., Rich, P.M., Barnes, F.J., Campbell, K., 1997. Overstory-imposed heterogeneity in solar radiation and soil moisture in a semiarid woodland. *Ecol. Appl.* 7, 1201–1215. doi:10.1890/1051-0761(1997)007[1201:OIHISR]2.0.CO;2

- Brunetti, G., Simunek, J., Piro, P., 2016a. A comprehensive numerical analysis of the hydraulic behavior of permeable pavement. *J. Hydrol.* 540, 1146–1161. doi:doi: 10.2136/vzj2016.04.0032
- Brunetti, G., Simunek, J., Piro, P., 2016b. A comprehensive analysis of the variably-saturated hydraulic behavior of a green roof in a mediterranean climate. *Vadose Zo. J.* 15, In press. doi:doi: 10.2136/vzj2016.04.0032
- Carbone, M., Brunetti, G., Piro, P., 2014. Hydrological Performance of a Permeable Pavement in Mediterranean Climate, in: 14th SGEM GeoConference on Water Resources. Forest, Marine And Ocean Ecosystems. pp. 381–388. doi:10.5593/SGEM2014/B31/S12.050
- Carbone, M., Brunetti, G., Piro, P., 2015a. Modelling the Hydraulic Behaviour of Growing Media with the Explicit Finite Volume Solution. *Water* 7, 568–591. doi:10.3390/w7020568
- Carbone, M., Turco, M., Brunetti, G., Piro, P., 2015b. A Cumulative Rainfall Function for Subhourly Design Storm in Mediterranean Urban Areas. *Adv. Meteorol.* 2015, 1–10. doi:10.1155/2015/528564
- Cheviron, B., Coquet, Y., 2009. Sensitivity Analysis of Transient-MIM HYDRUS-1D: Case Study Related to Pesticide Fate in Soils. *Vadose Zo. J.* 8, 1064. doi:10.2136/vzj2009.0023
- Coffman, L.S., 2002. Low-impact development: an alternative stormwater management technology., in: France, R.L. (Ed.), *Handbook of Water Sensitive Planning and Design*. Lewis Publishers Inc., pp. 97–123.
- Collins, K.A., Hunt, W.F., Hathaway, J.M., 2008. Hydrologic Comparison of Four Types of Permeable Pavement and Standard Asphalt in Eastern North Carolina. *J. Hydrol. Eng.* 13, 1146–1157. doi:10.1061/(ASCE)1084-0699(2008)13:12(1146)
- Dane, J.H., Hopmans, J.W., 2002. Pressure plate extractor, in: Dane, J.H., Topp, G.C. (Eds.),

- Methods of Soil Analysis. Part 4. Physical Methods. SSSA, Madison, WI, pp. 688–690.
- Davis, A.P., 2008. Field Performance of Bioretention: Hydrology Impacts. *J. Hydrol. Eng.* 13, 90–95. doi:10.1061/(ASCE)1084-0699(2008)13:2(90)
- DeWalle, D.R., Swistock, B.R., Johnson, T.E., McGuire, K.J., 2000. Potential effects of climate change and urbanization on mean annual streamflow in the United States. *Water Resour. Res.* 36, 2655–2664. doi:10.1029/2000WR900134
- Dosskey, M.G., Helmers, M.J., Eisenhauer, D.E., Franti, T.G., Hoagland, K.D., 2002. Assessment of concentrated flow through riparian buffers. *J. Soil Water Conserv.* 57, 336–343. doi:VL - 57
- Draper, N., Smith, H., 1981. *Applied regression analysis* 2nd ed., Technometrics. doi:10.1198/tech.2005.s303
- Duan, Q., Sorooshian, S., Gupta, V., 1992. Effective and efficient global optimization for conceptual rainfall-runoff models. *Water Resour. Res.* 28, 1015–1031. doi:10.1029/91WR02985
- Durhman, A.K., Bradley Rowe, D., Rugh, C.L., 2006. Effect of watering regimen on chlorophyll fluorescence and growth of selected green roof plant taxa. *HortScience* 41, 1623–1628.
- Durner, W., 1994. Hydraulic conductivity estimation for soils with heterogeneous pore structure. *Water Resour. Res.* 30, 211–223. doi:10.1029/93WR02676
- Efron, B., Tibshirani, R., 1986. *Bootstrap Methods for Standard Errors, Confidence Intervals, and Other Measures of Statistical Accuracy.* *Stat. Sci.* 1, 54–75.
- Elliot, A., Trowsdale, S., 2007. A review of models for low impact urban stormwater drainage. *Environ. Model. Softw.* 22, 394–405. doi:10.1016/j.envsoft.2005.12.005
- Fassman, E. a., Blackbourn, S., 2010. Urban Runoff Mitigation by a Permeable Pavement System over Impermeable Soils. *J. Hydrol. Eng.* 15, 475–485.

doi:10.1061/(ASCE)HE.1943-5584.0000238

Feddes, R.A., Kowalik, P.J., Zaradny, H., 1978. Simulation of field water use and crop yield. PUDOC, Wageningen.

Forrester, A.I.J., Sóbester, A., Keane, A.J., 2008. Engineering Design via Surrogate Modelling: A practical Guide. J. Wiley. doi:10.1002/9780470770801

Geiger, S., Cortis, A., Birkholzer, J.T., 2010. Upscaling solute transport in naturally fractured porous media with the continuous time random walk method. *Water Resour. Res.* 46, n/a–n/a. doi:10.1029/2010WR009133

Getter, K.L., Rowe, D.B., Andresen, J.A., 2007. Quantifying the effect of slope on extensive green roof stormwater retention. *Ecol. Eng.* 31, 225–231. doi:10.1016/j.ecoleng.2007.06.004

Gill, M.K., Kaheil, Y.H., Khalil, A., McKee, M., Bastidas, L., 2006. Multiobjective particle swarm optimization for parameter estimation in hydrology. *Water Resour. Res.* 42, n/a–n/a. doi:10.1029/2005WR004528

Gironás, J., Roesner, L. a, Rossman, L. a, Davis, J., 2010. A new applications manual for the Storm Water Management Model (SWMM). *Environ. Model. Softw.* 25, 813–814. doi:10.1016/j.envsoft.2009.11.009

Gutmann, H.M., 2001. A Radial Basis Function Method for Global Optimization. *J. Glob. Optim.* 19, 201–227. doi:10.1023/A:1011255519438

Hanscom, Z., Ting, I.P., 1978. Responses of succulents to plant water stress. *Plant Physiol.* 61, 327–30.

Hilten, R.N., Lawrence, T.M., Tollner, E.W., 2008. Modeling stormwater runoff from green roofs with HYDRUS-1D. *J. Hydrol.* 358, 288–293. doi:10.1016/j.jhydrol.2008.06.010

Hodnet, M.G., Bell, J.P., 1990. Processes of water movement through a chalk coombe deposit in Southeast England. *Hydrol. Process.* 4, 361–372. doi:10.1002/hyp.3360040406

- Hopmans, J.W., Šimůnek, J., Romano, N., Durner, W., 2002. Inverse Modeling of Transient Water Flow, in: Dane, J.H., Topp, G.C. (Eds.), *Methods of Soil Analysis, Part 4, Physical Methods*. SSSA, Madison, WI, pp. 963–1008.
- Hornberger, G.M., Spear, R.C., 1981. An approach to the preliminary analysis of environmental systems. *J. Environ. Manage.* 12, 7–12. doi:10.1016/S0272-4944(89)80026-X
- Houska, T., Multsch, S., Kraft, P., Frede, H.-G., Breuer, L., 2013. Monte Carlo based calibration and uncertainty analysis of a coupled plant growth and hydrological model. *Biogeosciences Discuss.* 10, 19509–19540. doi:10.5194/bgd-10-19509-2013
- Hu, S., 1987. Akaike information criterion statistics. *Math. Comput. Simul.* 29, 452. doi:10.1016/0378-4754(87)90094-2
- Illgen, M., Harting, K., Schmitt, T.G., Welker, A., 2007. Runoff and infiltration characteristics of pavement structures--review of an extensive monitoring program. *Water Sci. Technol.* 56, 133–40. doi:10.2166/wst.2007.750
- Ines, A.V.M., Droogers, P., 2002. Inverse modelling in estimating soil hydraulic functions: a Genetic Algorithm approach. *Hydrol. Earth Syst. Sci. Discuss.* 6, 49–66.
- Jiang, Y., Liu, C., Huang, C., Wu, X., 2010. Improved particle swarm algorithm for hydrological parameter optimization. *Appl. Math. Comput.* 217, 3207–3215. doi:10.1016/j.amc.2010.08.053
- Jones, D.R., 2001. A Taxonomy of Global Optimization Methods Based on Response Surfaces. *J. Glob. Optim.* 21, 345–383. doi:10.1023/A:1012771025575
- Jones, D.R., Schonlau, M., William, J., 1998. Efficient Global Optimization of Expensive Black-Box Functions. *J. Glob. Optim.* 13, 455–492. doi:10.1023/a:1008306431147
- Kasmin, H., Stovin, V.R., Hathway, E.A., 2010. Towards a generic rainfall-runoff model for green roofs. *Water Sci. Technol.* 62, 898–905. doi:10.2166/wst.2010.352

- Keating, E.H., Doherty, J., Vrugt, J.A., Kang, Q., 2010. Optimization and uncertainty assessment of strongly nonlinear groundwater models with high parameter dimensionality. *Water Resour. Res.* 46, n/a–n/a. doi:10.1029/2009WR008584
- Kennedy, J., Eberhart, R., 1995. Particle Swarm Optimization. *Eng. Technol.* 1942–1948.
- Kennedy, J., Spears, W.M., 1998. Matching algorithms to problems: an experimental test of the particle swarm and some genetic algorithms on the multimodal problem generator, in: 1998 IEEE International Conference on Evolutionary Computation Proceedings. IEEE World Congress on Computational Intelligence (Cat. No.98TH8360). IEEE, pp. 78–83. doi:10.1109/ICEC.1998.699326
- Khu, S.-T., Werner, M.G.F., 2003. Reduction of Monte-Carlo simulation runs for uncertainty estimation in hydrological modelling. *Hydrol. Earth Syst. Sci.* 7, 680–692. doi:10.5194/hess-7-680-2003
- Klute, A., Dirksen, C., 1986. Hydraulic conductivity and diffusivity. Laboratory methods. *Methods soil Anal. - part 1. Phys. Mineral. methods* 9, 687–734. doi:10.2136/sssabookser5.1.2ed.c28
- Kundzewicz, Z., Radziejewski, M., Pínskwar, I., 2006. Precipitation extremes in the changing climate of Europe. *Clim. Res.* 31, 51–58. doi:10.3354/cr031051
- Laloy, E., Rogiers, B., Vrugt, J.A., Mallants, D., Jacques, D., 2013. Efficient posterior exploration of a high-dimensional groundwater model from two-stage Markov chain Monte Carlo simulation and polynomial chaos expansion. *Water Resour. Res.* 49, 2664–2682. doi:10.1002/wrcr.20226
- Lazzarin, R.M., Castellotti, F., Busato, F., 2005. Experimental measurements and numerical modelling of a green roof. *Energy Build.* 37, 1260–1267. doi:10.1016/j.enbuild.2005.02.001
- Lenderink, G., van Meijgaard, E., 2008. Increase in hourly precipitation extremes beyond expectations from temperature changes. *Nat. Geosci.* 1, 511–514. doi:10.1038/ngeo262

- Leopold, L.B., 1968. Hydrology for Urban Land Planning - A Guidebook on the Hydrologic Effects of Urban Land Use. U.S. Government Printing Office, Washington D.C.
- Levinson, R., Akbari, H., 2002. Effects of composition and exposure on the solar reflectance of portland cement concrete. *Cem. Concr. Res.* 32, 1679–1698. doi:10.1016/S0008-8846(02)00835-9
- Li, Y., Babcock, R.W., 2014. Green roof hydrologic performance and modeling: A review. *Water Sci. Technol.* 69, 727–738. doi:10.2166/wst.2013.770
- Li, Y., Babcock, R.W., 2015. Modeling Hydrologic Performance of a Green Roof System with HYDRUS-2D. *J. Environ. Eng.* 141, 04015036. doi:10.1061/(ASCE)EE.1943-7870.0000976
- Liang, J.J., Qin, A.K., Suganthan, P.N., Baskar, S., 2006. Comprehensive learning particle swarm optimizer for global optimization of multimodal functions. *IEEE Trans. Evol. Comput.* 10, 281–295. doi:10.1109/TEVC.2005.857610
- Liu, H.H., Doughty, C., Bodvarsson, G.S., 1998. An active fracture model for unsaturated flow and transport in fractured rocks. *Water Resour. Res.* 34, 2633–2646. doi:10.1029/98WR02040
- Liu, H.-H., Haukwa, C.B., Ahlers, C.F., Bodvarsson, G.S., Flint, A.L., Guertal, W.B., 2003. Modeling flow and transport in unsaturated fractured rock: an evaluation of the continuum approach. *J. Contam. Hydrol.* 62-63, 173–188. doi:10.1016/S0169-7722(02)00170-5
- Locatelli, L., Mark, O., Mikkelsen, P.S., Arnbjerg-Nielsen, K., Bergen Jensen, M., Binning, P.J., 2014. Modelling of green roof hydrological performance for urban drainage applications. *J. Hydrol.* 519, 3237–3248. doi:10.1016/j.jhydrol.2014.10.030
- Mackay, D.J.C., 1998. Introduction to Gaussian processes. *Neural Networks Mach. Learn.* 168, 133–165. doi:10.1007/s10067-003-0742-1

- Marquardt, D.W., 1963. An Algorithm for Least-Squares Estimation of Nonlinear Parameters. *J. Soc. Ind. Appl. Math.* 11, 431–441. doi:10.1137/0111030
- McKay, M.D., Beckman, R.J., Conover, W.J., 1979. Comparison of Three Methods for Selecting Values of Input Variables in the Analysis of Output from a Computer Code. *Technometrics* 21, 239–245. doi:10.1080/00401706.1979.10489755
- Metselaar, K., 2012. Water retention and evapotranspiration of green roofs and possible natural vegetation types. *Resour. Conserv. Recycl.* 64, 49–55. doi:10.1016/j.resconrec.2011.12.009
- Min, S.-K., Zhang, X., Zwiers, F.W., Hegerl, G.C., 2011. Human contribution to more-intense precipitation extremes. *Nature* 470, 378–81. doi:10.1038/nature09763
- Moriiasi, D.N., Arnold, J.G., Van Liew, M.W., Binger, R.L., Harmel, R.D., Veith, T.L., 2007. Model evaluation guidelines for systematic quantification of accuracy in watershed simulations. *Trans. ASABE* 50, 885–900. doi:10.13031/2013.23153
- Munoz-Carpena, R., Parsons, J.E., 2004. A design procedure for vegetative filter strips using VFSMOD-W. *Trans. Asae* 47, 1933–1941.
- Nash, J.E., Sutcliffe, J. V., 1970. River flow forecasting through conceptual models part I - A discussion of principles. *J. Hydrol.* 10, 282–290. doi:10.1016/0022-1694(70)90255-6
- Nash, J.E., Sutcliffe, J. V, 1970. River Flow Forecasting through Conceptual Models: Part I - A Discussion of Principles. *J. Hydrol.* 10, 282–290. doi:10.1016/0022-1694(70)90255-6
- Newcomer, M.E., Gurdak, J.J., Sklar, L.S., Nanus, L., 2014. Urban recharge beneath low impact development and effects of climate variability and change. *Water Resour. Res.* 50, 1716–1734. doi:10.1002/2013WR014282
- Nossent, J., Elsen, P., Bauwens, W., 2011. Sobol' sensitivity analysis of a complex environmental model. *Environ. Model. Softw.* 26, 1515–1525. doi:10.1016/j.envsoft.2011.08.010

- O'Hagan, A., 2006. Bayesian analysis of computer code outputs: A tutorial. *Reliab. Eng. Syst. Saf.* 91, 1290–1300. doi:10.1016/j.res.2005.11.025
- Oakley, J.E., O'Hagan, A., 2004. Probabilistic sensitivity analysis of complex models: A Bayesian approach. *J. R. Stat. Soc. Ser. B Stat. Methodol.* 66, 751–769. doi:10.1111/j.1467-9868.2004.05304.x
- OECD, 2013. *Water and Climate Change Adaptation: Policies to Navigate Uncharted Waters*, OECD Studies on Water. OECD Publishing, Paris. doi:10.1787/9789264200449-en
- Palla, A., Gnecco, I., Lanza, L.G., 2009. Unsaturated 2D modelling of subsurface water flow in the coarse-grained porous matrix of a green roof. *J. Hydrol.* doi:10.1016/j.jhydrol.2009.10.008
- Pan, L., Wu, L., 1998. A hybrid global optimization method for inverse estimation of hydraulic parameters: Annealing-simplex method. *Water Resour. Res.* 34, 2261–2269. doi:10.1029/98WR01672
- Pedersen, M.E.H., 2010. Good parameters for particle swarm optimization, Technical Report HL1001, Hvass Laboratories.
- Pertassek, T., Peters, A., Durner, W., 2015. *HYPROP-FIT Software User's Manual*, V.3.0.
- Peters, a., Durner, W., 2006. Improved estimation of soil water retention characteristics from hydrostatic column experiments. *Water Resour. Res.* 42, n/a–n/a. doi:10.1029/2006WR004952
- Peters, A., Durner, W., 2008. Simplified evaporation method for determining soil hydraulic properties. *J. Hydrol.* 356, 147–162. doi:10.1016/j.jhydrol.2008.04.016
- Poli, R., Kennedy, J., Blackwell, T., 2007. Particle swarm optimization. *Swarm Intell.* 1, 33–57. doi:10.1007/s11721-007-0002-0
- Rasmussen, C.E., Williams, C.K.I., 2006. *Gaussian processes for machine learning*. MIT Press, Cambridge, MA.

- Ratto, M., Tarantola, S., Saltelli, A., 2001. Sensitivity analysis in model calibration: GSA-GLUE approach. *Comput. Phys. Commun.* 136, 212–224. doi:10.1016/S0010-4655(01)00159-X
- Razavi, S., Tolson, B.A., Burn, D.H., 2012. Review of surrogate modeling in water resources. *Water Resour. Res.* 48, n/a–n/a. doi:10.1029/2011WR011527
- Regis, R.G., Shoemaker, C.A., 2004. Local function approximation in evolutionary algorithms for the optimization of costly functions. *IEEE Trans. Evol. Comput.* 8, 490–505. doi:10.1109/TEVC.2004.835247
- Rezaei, M., Seuntjens, P., Joris, I., Boëne, W., Van Hoey, S., Campling, P., Cornelis, W.M., 2015. Sensitivity of water stress in a two-layered sandy grassland soil to variations in groundwater depth and soil hydraulic parameters. *Hydrol. Earth Syst. Sci. Discuss.* 12, 6881–6920. doi:10.5194/hessd-12-6881-2015
- Ritchie, J.T., 1972. Model for predicting evaporation from a row crop with incomplete cover. *Water Resour. Res.* 8, 1204–1213. doi:10.1029/WR008i005p01204
- Rose, S., Peters, N.E., 2001. Effects of urbanization on streamflow in the Atlanta area (Georgia, USA): a comparative hydrological approach. *Hydrol. Process.* 15, 1441–1457. doi:10.1002/hyp.218
- Rosenberg, N.J., Blaine, L.B., Shashi, B.V., 1983. *Microclimate: the biological environment*. Wiley, New York.
- Sacks, J., Welch, W.J., Mitchell, T.J., Wynn, H.P., 1989. Design and analysis of computer experiments. *Stat. Sci.* 4, 409–435. doi:doi:10.1214/ss/1177012413
- Saltelli, A., 2002. Making best use of model evaluations to compute sensitivity indices. *Comput. Phys. Commun.* 145, 280–297. doi:10.1016/S0010-4655(02)00280-1
- Saltelli, A., Annoni, P., 2010. How to avoid a perfunctory sensitivity analysis. *Environ. Model. Softw.* 25, 1508–1517. doi:10.1016/j.envsoft.2010.04.012

- Saltelli, A., Annoni, P., Azzini, I., Campolongo, F., Ratto, M., Tarantola, S., 2010. Variance based sensitivity analysis of model output. Design and estimator for the total sensitivity index. *Comput. Phys. Commun.* 181, 259–270. doi:10.1016/j.cpc.2009.09.018
- Saltelli, A., Tarantola, S., 2004. *Sensitivity Analysis in Practice: A Guide to Assessing Scientific Models* 232.
- Saltelli, A., Tarantola, S., Saisana, M., Nardo, M., 2005. What is sensitivity analysis?, in: II Convegno Della Rete Dei Nuclei Di Valutazione E Verifica, Napoli 26, 27 Gennaio 2005, Centro Congressi Università Federico II, Via Partenope 36.
- Sayed, O.H., 2001. Crassulacean Acid Metabolism 1975-2000, a check list. *Photosynthetica* 39, 339–352. doi:10.1023/A:1015179704819
- Schaap, M.G., Leij, F.J., 1999. Improved Prediction of Unsaturated Hydraulic Conductivity with the Mualem-van Genuchten Model. *Soil Sci. Soc.* 64, 843–851. doi:10.2136/sssaj2000.643843x
- Schaap, M.G., Leij, F.J., van Genuchten, M.T., 2001. rosetta: a computer program for estimating soil hydraulic parameters with hierarchical pedotransfer functions. *J. Hydrol.* 251, 163–176. doi:10.1016/S0022-1694(01)00466-8
- Schindler, U., 1980. Ein Schnellverfahren zur Messung der Wasserleitfähigkeit im teilgesättigten Boden an Stechzylinderproben. *Arch. für Acker- und Pflanzenbau und Bodenkd.* 24, 1–7.
- Schindler, U., Durner, W., von Unold, G., Mueller, L., Wieland, R., 2010a. The evaporation method: Extending the measurement range of soil hydraulic properties using the air-entry pressure of the ceramic cup. *J. Plant Nutr. Soil Sci.* 173, 563–572. doi:10.1002/jpln.200900201
- Schindler, U., Durner, W., von Unold, G., Muller, L., 2010b. Evaporation Method for Measuring Unsaturated Hydraulic Properties of Soils: Extending the Measurement Range. *Soil Sci Soc Am J* 74, 1071–1083. doi:10.2136/sssaj2008.0358

- Schonlau, M., 1997. Computer experiments and global optimization. PhD Thesis. University of Waterloo, Waterloo, Canada.
- Scott, D.W., 1992. Frontmatter, Wiley Series in Probability and Mathematical Statistics Applied Probability and Statistics Section. doi:10.1002/9780470316849.fmatter
- Sevat, E., Dezetter, A., Servat, E., 1991. Selection of calibration objective functions in the context of rainfall-runoff modelling in a sudanese savannah area. *Hydrol. Sci. - J. - des Sci. Hydrol.* 36, 307–330. doi:10.1080/02626669109492517
- She, N., Pang, J., 2010. Physically Based Green Roof Model. *J. Hydrol. Eng.* 15, 458–464. doi:10.1061/(ASCE)HE.1943-5584.0000138
- Shi, Y., Eberhart, R., 1998. A modified particle swarm optimizer. 1998 IEEE Int. Conf. Evol. Comput. Proceedings. IEEE World Congr. Comput. Intell. (Cat. No.98TH8360) 69–73. doi:10.1109/ICEC.1998.699146
- Shi, Y., Eberhart, R.C., 1999. Empirical study of particle swarm optimization. Proc. 1999 Congr. Evol. Comput. 1945–1950. doi:10.1109/CEC.1999.785511
- Silverman, B., 1981. Using kernel density estimates to investigate multimodality. *J. R. Stat. Soc.* 43, 97–99.
- Simmons, D.L., Reynolds, R.J., 1982. EFFECTS OF URBANIZATION ON BASE FLOW OF SELECTED SOUTH-SHORE STREAMS, LONG ISLAND, NEW YORK. *J. Am. Water Resour. Assoc.* 18, 797–805. doi:10.1111/j.1752-1688.1982.tb00075.x
- Simunek, J., Jarvis, N.J., van Genuchten, M.T., Gardenas, A., 2003. Review and comparison of models for describing non-equilibrium and preferential flow and transport in the vadose zone. *J. Hydrol.* 272, 14–35. doi:10.1016/S0022-1694(02)00252-4
- Šimůnek, J., van Genuchten, M.T., 2008. Modeling Nonequilibrium Flow and Transport Processes Using HYDRUS. *Vadose Zo. J.* 7, 782. doi:10.2136/vzj2007.0074
- Šimůnek, J., van Genuchten, M.T., Šejna, M., 2008. Development and Applications of the

- HYDRUS and STANMOD Software Packages and Related Codes. *Vadose Zo. J.* 7, 587. doi:10.2136/vzj2007.0077
- Šimůnek, J., van Genuchten, M.T., Šejna, M., 2016. Recent Developments and Applications of the HYDRUS Computer Software Packages. *Vadose Zo. J.* 15, 25. doi:10.2136/vzj2016.04.0033
- Šimůnek, J., van Genuchten, M.T., Wendroth, O., 1998. Parameter Estimation Analysis of the Evaporation Method for Determining Soil Hydraulic Properties. *Soil Sci. Soc. Am. J.* 62, 894. doi:10.2136/sssaj1998.03615995006200040007x
- Sobol', I., 2001. Global sensitivity indices for nonlinear mathematical models and their Monte Carlo estimates. *Math. Comput. Simul.* 55, 271–280. doi:10.1016/S0378-4754(00)00270-6
- Song, X., Zhang, J., Zhan, C., Xuan, Y., Ye, M., Xu, C., 2015. Global sensitivity analysis in hydrological modeling: Review of concepts, methods, theoretical framework, and applications. *J. Hydrol.* 523, 739–757. doi:10.1016/j.jhydrol.2015.02.013
- Starry, O., Lea-Cox, J.D., Kim, J., van Iersel, M.W., 2014. Photosynthesis and water use by two *Sedum* species in green roof substrate. *Environ. Exp. Bot.* 107, 105–112. doi:10.1016/j.envexpbot.2014.05.014
- Stovin, V., Poë, S., Berretta, C., 2013. A modelling study of long term green roof retention performance. *J. Environ. Manage.* 131, 206–215. doi:10.1016/j.jenvman.2013.09.026
- Sutanto, S.J., Wenninger, J., Coenders-Gerrits, A.M.J., Uhlenbrook, S., 2012. Partitioning of evaporation into transpiration, soil evaporation and interception: A comparison between isotope measurements and a HYDRUS-1D model. *Hydrol. Earth Syst. Sci.* 16, 2605–2616. doi:10.5194/hess-16-2605-2012
- Taylor, S.A., Ashcroft, G.L., 1972. *Physical Edaphology: The Physics of Irrigated and Nonirrigated Soils.* W.H. Freeman, San Francisco.

- Tokunaga, T.K., 2009. Hydraulic properties of adsorbed water films in unsaturated porous media. *Water Resour. Res.* 45, 1287–1295. doi:10.1029/2009WR007734
- Tokunaga, T.K., Wan, J., 1997. Water film flow along fracture surfaces of porous rock. *Water Resour. Res.* 33, 1287–1295. doi:10.1029/97WR00473
- Torres, E.A., Calera, A., 2010. Bare soil evaporation under high evaporation demand: a proposed modification to the FAO-56 model. *Hydrol. Sci. J.* 55, 303–315. doi:10.1080/02626661003683249
- Trimble, S.W., 1997. Contribution of Stream Channel Erosion to Sediment Yield from an Urbanizing Watershed. *Science* (80-.). 278, 1442–1444. doi:10.1126/science.278.5342.1442
- UMS GmbH, 2015. UMS (2015): Manual HYPROP, Version 2015-01.
- Usher, W., xantares, Hadka, D., bernardoct, Fernando, Herman, J., Mutel, C., 2015. SALib: New documentation, doc strings and installation requirements. doi:10.5281/zenodo.31316
- van Dam, J.C., Groenendijk, P., Hendriks, R.F. a., Kroes, J.G., 2008. Advances of Modeling Water Flow in Variably Saturated Soils with SWAP. *Vadose Zo. J.* 7, 640. doi:10.2136/vzj2007.0060
- van Genuchten, M.T., 1980. A Closed-form Equation for Predicting the Hydraulic Conductivity of Unsaturated Soils1. *Soil Sci. Soc. Am. J.* 44, 892–898. doi:10.2136/sssaj1980.03615995004400050002x
- Van Genuchten, M.T., Wierenga, P.J., 1976. Mass Transfer Studies in Sorbing Porous Media I. Analytical Solutions. *Soil Sci. Soc. Am. J.* 40, 473–480.
- Vesuviano, G., Sonnenwald, F., Stovin, V., 2014. A two-stage storage routing model for green roof runoff detention. *Water Sci. Technol.* 69, 1191–7. doi:10.2166/wst.2013.808
- Vrugt, J.A., Gupta, H. V., Bouten, W., Sorooshian, S., 2003. A Shuffled Complex Evolution

- Metropolis algorithm for optimization and uncertainty assessment of hydrologic model parameters. *Water Resour. Res.* 39, n/a–n/a. doi:10.1029/2002WR001642
- Vrugt, J.A., Schoups, G., Hopmans, J.W., Young, C., Wallender, W.W., Harter, T., Bouten, W., 2004. Inverse modeling of large-scale spatially distributed vadose zone properties using global optimization. *Water Resour. Res.* 40, n/a–n/a. doi:10.1029/2003WR002706
- Vrugt, J.A., Stauffer, P.H., Wöhling, T., Robinson, B.A., Vesselinov, V. V., 2008. Inverse Modeling of Subsurface Flow and Transport Properties: A Review with New Developments. *Vadose Zo. J.* 7, 843. doi:10.2136/vzj2007.0078
- Wang, G.G., Shan, S., 2007. Review of Metamodeling Techniques in Support of Engineering Design Optimization. *J. Mech. Des.* 129, 370. doi:10.1115/1.2429697
- Warren, J.E., Root, P.J., 1963. The Behavior of Naturally Fractured Reservoirs. *Soc. Pet. Eng. J.* 3, 245–255. doi:10.2118/426-PA
- Wasko, C., Sharma, A., 2015. Steeper temporal distribution of rain intensity at higher temperatures within Australian storms. *Nat. Geosci.* 8, 527–529. doi:10.1038/ngeo2456
- Wendroth, O., Ehlers, W., Kage, H., Hopmans, J.W., Halbertsma, J., Wösten, J.H.M., 1993. Reevaluation of the Evaporation Method for Determining Hydraulic Functions in Unsaturated Soils. *Soil Sci. Soc. Am. J.* 57, 1436–1443. doi:10.2136/sssaj1993.03615995005700060007x
- Wesseling, J., Elbers, J., Kabat, P., Broek, B. Van den, 1991. SWATRE: instructions for input. Intern. Note, Winand Star. Cent.
- Westra, S., Fowler, H.J., Evans, J.P., Alexander, L. V., Berg, P., Johnson, F., Kendon, E.J., Lenderink, G., Roberts, N.M., 2014. Future changes to the intensity and frequency of short-duration extreme rainfall. *Rev. Geophys.* 52, 522–555. doi:10.1002/2014RG000464
- Whipple, W., DiLouie, J.M., Pytlar, T., 1981. EROSIONAL POTENTIAL OF STREAMS

- IN URBANIZING AREAS. *J. Am. Water Resour. Assoc.* 17, 36–45.
doi:10.1111/j.1752-1688.1981.tb02586.x
- Wong, T.H.F., Fletcher, T.D., Duncan, H.P., Jenkins, G.A., 2006. Modelling urban stormwater treatment-A unified approach. *Ecol. Eng.* 27, 58–70.
doi:10.1016/j.ecoleng.2005.10.014
- Ye, K.Q., Li, W., Sudjianto, A., 2000. Algorithmic construction of optimal symmetric Latin hypercube designs. *J. Stat. Plan. Inference* 90, 145–159. doi:10.1016/S0378-3758(00)00105-1
- Younes, A., Mara, T.A., Fajraoui, N., Lehmann, F., Belfort, B., Beydoun, H., 2013. Use of global sensitivity analysis to help assess unsaturated soil hydraulic parameters. *Vadose Zo. J.* 12. doi:10.2136/vzj2011.0150
- Zambrano-Bigiarini, M., Rojas, R., 2013. A model-independent Particle Swarm Optimisation software for model calibration. *Environ. Model. Softw.* 43, 5–25.
doi:10.1016/j.envsoft.2013.01.004
- Zhang, S., Guo, Y., 2015. SWMM Simulation of the Storm Water Volume Control Performance of Permeable Pavement Systems. *J. Hydrol. Eng.* 20, 06014010.
doi:10.1061/(ASCE)HE.1943-5584.0001092
- Zhang, S.H., Guo, Y.P., 2013. Analytical Probabilistic Model for Evaluating the Hydrologic Performance of Green Roofs. *J. Hydrol. Eng.* 18, 19–28. doi:10.1061/(ASCE)HE.1943-5584.0000593
- Zhang, X., Srinivasan, R., Van Liew, M., 2009. Approximating SWAT Model Using Artificial Neural Network and Support Vector Machine. *JAWRA J. Am. Water Resour. Assoc.* 45, 460–474. doi:10.1111/j.1752-1688.2009.00302.x